HYDROMECHANICAL BEHAVIOUR OF A SURGE-TYPE GLACIER: TRAPRIDGE GLACIER, YUKON TERRITORY, CANADA

By

Jeffrey L. Kavanaugh

B. Sc. (Physics) Sonoma State University, 1994

A THESIS SUBMITTED IN PARTIAL FULFILLMENT OF

THE REQUIREMENTS FOR THE DEGREE OF

DOCTOR OF PHILOSOPHY

in

THE FACULTY OF GRADUATE STUDIES

EARTH AND OCEAN SCIENCES

We accept this thesis as conforming

to the required standard

THE UNIVERSITY OF BRITISH COLUMBIA

December 2000

In presenting this thesis in partial fulfilment of the requirements for an advanced degree at the University of British Columbia, I agree that the Library shall make it freely available for reference and study. I further agree that permission for extensive copying of this thesis for scholarly purposes may be granted by the head of my department or by his or her representatives. It is understood that copying or publication of this thesis for financial gain shall not be allowed without my written permission.

Earth and Ocean Sciences

The University of British Columbia

129-2219 Main Mall

Vancouver, Canada

V6T 1Z4

Date:

20 December, 2000

Abstract

Subglacial hydrological and mechanical processes play a critical role in determining the flow characteristics and stability of glaciers and ice sheets, but our understanding of these processes remains incomplete. Instrument and modelling studies of conditions beneath Trapridge Glacier, a small surge-type glacier in the St. Elias mountains, Yukon Territory, Canada, yield additional insight into subglacial hydromechanical behaviour.

High-pressure pulses in the subglacial drainage system are indicated by sudden offsets in measured pressure and result from damage to the pressure sensor measurement diaphragm. Laboratory and modelling studies confirm that pressures significantly above the transducer rating produce offsets comparable to those observed in field records. Instrument records suggest that high-pressure pulses are generated by abrupt glacier motion that compresses or dilates the subglacial hydraulic system.

Analysis of instrument records taken during summer 1995 reveals that a series of hydromechanical events occurred following the establishment of a subglacial drainage system. Pressure fluctuations in this drainage system weakened a basal region that was acting as a pinning point, resulting in three episodes of strong basal motion.

I develop a simple hydromechanical model of basal processes acting beneath a soft-bedded alpine glacier. In this model, I classify the glacier bed into three regions: soft-bedded and hydraulically-connected to the subglacial drainage system, soft-bedded and unconnected and hard-bedded. Each basal region is modelled as a one-dimensional column. The time evolution of pore-water pressure, till dilatancy, sediment deformation and glacier sliding is calculated in soft-bedded regions; hard-bedded regions are considered

rigid and impermeable. The regions are coupled by a simple ice-dynamics model. Sediment deformation is calculated for four till flow laws: linear-viscous, nonlinear-viscous, nonlinear- Bingham and Coulomb-plastic. I develop relations describing instrument responses to modelled subglacial basal conditions.

I apply the hydromechanical model to simulate typical summer conditions beneath Trapridge Glacier. Modelled pore-water pressure profiles, deformation profiles, basal shear stress and instrument responses are presented for the four flow laws. Comparison of synthetic and field instrument responses suggests that till behaviour is best represented as Coulomb-plastic.

Table of Contents

List of Tables

List of Figures

List of Symbols

Chapter 2:

a_0	Sensor response equation constant (mV)
Δa_0	Change in sensor response equation constant (mV)
a_1	Sensor response equation constant ($\mathrm{mV\,m^{-1}}$)
b_0	Sensor calibration equation constant (m)
b_1	Sensor calibration equation constant ($\mathrm{m\,mV^{-1}}$)
h	Pressure head (m)
g	Gravitational acceleration ($\mathrm{m\,s^{-2}}$)
Δh	Elevation change (m)
P	Water pressure (kPa)
P_i	Pressure head measured by transducer i (m)
P^*	Damage pressure (kPa, m)
ΔP	Pressure head difference (m)
t	time (d)
V	Voltage (mV)
ΔV	Voltage difference (mV)
ρ_w	Density of water ($\mathrm{kg\,m^{-3}}$)

Chapters 3–5:

a, b	Till flow law exponents
a_{PL}	Semi-minor axis of ploughmeter (m)
c_{PL}	Semi-major axis of ploughmeter (m)
A_0	Glen flow law parameter ($\mathrm{(kPa)^{-3}s^{-1}}$)
B	General till flow law parameter ($\mathrm{(kPa)^{0.47}a^{-1}}$)
B_1	Nonlinear-viscous till flow law parameter ($\mathrm{(kPa)^{0.47}a^{-1}}$)
B_2	Nonlinear-Bingham till flow law parameter ($\mathrm{(kPa)^{0.625}a^{-1}}$)
B_c	Compression index
B_s	Swelling index
c_0	Residual cohesion
C_{SL}	Sliding coefficient
d_{PL}	Ploughmeter diameter (m)
D_0	Scaling factor

e	Void ratio
e_0, e_1, $e_0^\dagger$	Reference void ratio
e_{CS}	Critical state void ratio
$\dot{e}_D$	Rate-of-change of void ratio due to dilatant reorganization (s^{-1})
$\tilde{f}(z,t)$	Eulerian expression of function f
$f(F,t)$	Lagrangian expression of function f
F	Modelled ploughmeter force response $(\mathrm{kg\,m\,s}^{-2})$
F'	Force per unit length $(\mathrm{kg\,s}^{-2})$
G_I	Ice rigidity (Pa)
h	Till layer thickness (m)
h_g	Location of ploughmeter strain gauge centre (m)
h_{SL}	Lubricating layer thickness (m)
H	Ice thickness (m)
J	Jacobian
l_g	Ploughmeter tip-to-offset distance (m)
l_{BT}	Length of tilt cell (m)
L	Lengthscale of variation (m)
L_H	Lengthscale separating hard-bedded, soft-bedded regions (m)
L_S	Lengthscale separating soft-bedded regions (m)
m_s	Mass of solids
m_w	Mass of water
M	Bending moment $(\mathrm{kg\,m^2\,s}^{-2})$
n	Porosity
N	Glen flow law exponent
p	Water pressure (kPa)
p_{PZ}	Modelled pore-water transducer response value (kPa)
p_h	Pressure head (m)
p_0, p_1	Reference water pressure (kPa)
p_{SL}	Reference water pressure for sliding (kPa)
Δp_{SL}	Water pressure range for sliding (kPa)
$\dot{p}$	Rate-of-change of water pressure (kPa)
p_I	Ice overburden pressure (kPa)

p_{Ti}	Mean water pressure at $Z = H$ in column i (kPa)
$p_{\Delta Ti}$	Amplitude of diurnal pressure variation at $Z = H$ in column i (kPa)
p_{Bi}	Mean water pressure at $Z = 0$ in column i (kPa)
p'	Effective pressure (kPa)
p'_0, p'_1	Reference effective pressure (kPa)
$\dot{p}'$	Rate-of-change of effective pressure (kPa)
P'	Preconsolidation effective pressure (kPa)
s	Till displacement (m)
s_{SL}	Sliding displacement (m)
S	Total ice displacement (m)
S_0	Surface-to-volume ratio of solids (m^{-1})
q_w	Water flux ($kg\,s^{-1}$)
t	time (s)
v_s	Velocity of solids ($m\,s^{-1}$)
v_x	Till deformation rate ($m\,s^{-1}$)
v_{SL}	Sliding rate ($m\,s^{-1}$)
V	Total ice velocity ($m\,s^{-1}$)
ΔV	Velocity contrast between columns ($m\,s^{-1}$)
x	Longitudinal (down-glacier) coordinate (m)
x_b	Location of bottom of tilt cell (m)
x_t	Location of top of tilt cell (m)
x_{SL}	Modelled slidometer response value (m)
y	Longitudinal (across-glacier) coordinate (m)
z	Vertical Eulerian coordinate (m)
Z	Vertical Lagrangian coordinate (m)
Z_0	Instrument installation depth (m)
α	Compressibility of soil (Pa^{-1})
α_i	Areal fraction for region i
β	Compressibility of water (Pa^{-1})
$\dot{\varepsilon}$	Strain rate (s^{-1})
$\dot{\varepsilon}_0$	Reference strain rate (s^{-1})
$\dot{\varepsilon}_{b \to a}$	Strain rate of ice between columns a and b (s^{-1})

η_0	Effective till viscosity (Pa s)
η_{min}	Minimum effective till viscosity (Pa s)
θ	Ice surface slope (°)
θ_{BT}	Tilt angle measured by tilt cell (°)
κ	Hydraulic permeability (m^2)
μ_{SL}	Viscosity of lubricating layer (Pa s)
μ_w	Viscosity of water (Pa s)
ρ_s	Density of solids (kg m^{-3})
ρ_w	Density of water (kg m^{-3})
σ_Y	Yield stress (kPa)
σ_{min}	Stress at which $\eta = \eta_{min}$ (kPa)
τ	Basal shear stress (kPa)
τ_i	Basal shear stress for region i (kPa)
τ_0	Nominal basal shear stress (kPa)
$\tau_{b \to a}$	Shear stress transferred from column b to column a (kPa)
$\tau_{i \to j}$	Shear stress transferred from columns i to column j (kPa)
$\dot{\tau}_{b \to a}$	Rate-of-change of shear stress transferred from column b to column a (kPa)
$\dot{\tau}_{i \to j}$	Rate-of-change of shear stress transferred from column i to column j (kPa)
$\Delta\tau$	Coulomb-plastic failure range (kPa)
ϕ	Residual friction angle

Preface

Most of the material presented in Chapter 2 was previously published in the *Journal of Glaciology* (Kavanaugh and Clarke, 2000). A manuscript containing the data and interpretations presented in Chapter 3 has been submitted for publication to the same journal and is currently in review. Papers describing the development of the subglacial hydromechanical model and its application to the discrimination of till flow laws are being prepared for submission to the *Journal of Geophysical Research*. Because these chapters have been prepared as individual papers, some redundancy in introductory material is inevitable. I apologise for this repetition.

Acknowledgement

This thesis is dedicated to Brett Barrett and Bette Ruellen.

There are many people who have made my stay at UBC an enjoyable and rewarding experience. Foremost on this list is my research supervisor Garry K. C. Clarke. I have had the immense pleasure of spending six field seasons with Garry on Trapridge Glacier, which surely ranks as one of the finest places on this planet. I thank Garry for both his steady guidance and the remarkable amount of freedom I have been given in determining the direction of my research. I have benefitted greatly from my time working with Garry. I also appreciate the valuable contributions made by the other members of my supervisory committee, included Bruce Buffett, Rosemary Knight and Dave McClung.

I give heartfelt thanks to the members of the UBC Glaciology group, including Gwenn Flowers, Dave Hildes, Shawn Marshall, Urs Fischer, Kuan-Neng Foo, Tim Creyts and Nicolas Lhomme. In particular, the field seasons spent with Gwenn, Dave and Kuan-Neng provided me with many cherished memories and a wealth of data to draw this thesis from. It is hard to imagine a more supportive and cohesive environment than that found in the geophysics building at UBC. I will miss the frequent coffee-room sessions with Len Pasion, Kris Innanen, Andrew Gorman, Phil Hammer, Stéphane Rondenay, Eldad Haber, Ken Mattson, Colin Farquharson, Kim Welford, Charly Bank, Kristy Skaret, Evgenya Shkolnik, and Jaymie Matthews and the rather more infrequent impromptu jam sessions with Dave McMillan, Chris Wijns, and Dave Baird. I have enjoyed the time I have spent with such stellar non-geophysical Canadians as Jacquie Bastick, Joe Jazvak, Teri Leslie,

Chapter 1

Introduction

Sediment deformation and basal sliding can contribute significantly to the motion of glaciers and ice sheets that are underlain by water-saturated sediments. Basal sliding was recognized as a flow mechanism as early as the late-eighteenth century (de Saussure, 1779–96), and theories for glacier sliding over a rigid bed have been steadily refined over the past 125 years (e.g. Hopkins, 1862; Deeley and Parr, 1914; Weertman, 1957; Lliboutry, 1968, 1987; Nye, 1969; Kamb, 1970; Fowler, 1986). In contrast, the role sediment deformation plays in ice dynamics has only been recently recognized. Measurements by Boulton and Jones (1979) indicated that basal deformation accounted for ~90% of the total ice motion at Breidamerkurjökull, Iceland. Drawing from this observation, they concluded that extensive sediment deformation beneath Pleistocene ice sheet margins lowered the ice-margin surface profiles while allowing ice flow at remarkably low driving stresses, thus accounting for (1) the extent of reconstructed Pleistocene ice sheet margins over North America and Europe, (2) anomalously small isostatic rebound in these areas and (3) rapid retreat rates of the margins. This interpretation was bolstered by an 1986 seismic study of ice stream B, West Antarctica, which revealed a layer of water-saturated basal sediments several metres thick (Blankenship and others, 1986). Alley and others (1986) concluded that the high porosity and pore-water pressure values inferred from the seismic records indicate active deformation of the sediment layer and suggested that the ice stream moves primarily by such deformation.

Ice streams, which are regions of fast-moving ice bounded by slower-moving sheet

ice, play a principal role in the mass balance of the West Antarctic Ice Sheet. This ice sheet is grounded below sea level, which raises the concern that continued climatic warming could result in collapse of the ice sheet and a $\sim$5 m rise in global sea level (Mercer, 1978). Ice streams also provide modern analogues to fast-flowing regions of the Laurentide and Cordilleran Ice Sheets inferred from geologic evidence (e.g., Morner and Dreimanis, 1973; Clayton and Moran, 1982; Brown and others, 1987). Efforts to accurately model the response of both modern and past ice sheets to climate change have been hampered by unrealistic treatment of the basal boundary condition. As a result, much effort has been directed at determining both the "till flow law", which relates basal shear stress and pore-water pressure conditions to the strain rate within the till, and the "sliding law", relating basal shear stress and water pressure to slip at the ice–bed interface. It has been well-established that both sediment deformation and basal sliding are strongly influenced by subglacial hydraulic conditions, as high basal pressures act to weaken ice–bed coupling (e.g., Kamb and others, 1985; Iken and Bindschadler, 1986; Hooke and others, 1989; Fischer and Clarke, 1997b) and soften the underlying sediments (e.g., Boulton and others, 1974; Boulton and Hindmarsh, 1987; Iverson and others, 1995). Our understanding of these processes remains incomplete, however, and must be improved if we are to accurately assess the stability of glaciers and ice sheets and predict how they will respond to changes in global climate.

Fast flow is also exhibited by alpine glaciers that undergo quasi-periodic flow instabilities known as surges. During a surge, the glacier flow rate typically increases by more than an order of magnitude and a large volume of ice is transported from an up-glacier reservoir area to lower elevations. The active surge phase generally lasts between <1 and 6 years, after which the glacier returns to a quiescent state that typically lasts 20–30 years but can range between 15 and <100 years (Meier and Post, 1969). Glaciers that surge do so repeatedly and exhibit remarkably uniform periods. It is now believed that most

surge-type glaciers are underlain by deformable sediments, making it likely that similar mechanisms control both ice streaming and glacier surging. The study of surge-type glaciers provides the opportunity to gain valuable insight into these mechanisms despite the substantial differences in geometry and flow characteristics between alpine glaciers and ice streams. Alpine glaciers afford generally easier access and more temperate environments than do ice streams, and are typically significantly thinner than ice streams. Reduced drilling times increase the number of instruments that can be installed during a field season, allowing greater basal coverage and increasing the likelihood of recording interesting subglacial phenomena. While lubricating water beneath ice streams is thought to be basally generated, the thinner ice of alpine glaciers allows surface meltwater to reach the glacier bed, strongly influencing basal deformation and glacier sliding. The resulting seasonal and, during warmer months, diurnal variations in subglacial hydrological conditions are in marked contrast with the relatively stable conditions observed beneath ice streams. Although these variations raise the concern that the flow mechanisms operating beneath alpine glaciers and ice streams differ fundamentally, they also provide a means to better explore the interactions between subglacial hydrological and mechanical conditions. In this thesis I present an investigation of the hydromechanical behaviour of a surge-type glacier.

1.1 Previous work

Studies of basal processes are complicated by the difficulty of directly observing the glacier bed. In early studies, access to the bed was obtained through tunnels excavated to the glacier sole (e.g. Haefeli, 1951; McCall, 1952; Kamb and LaChapelle, 1964; Vivian and Bocquet, 1973; Boulton and Jones, 1979; Boulton and Hindmarsh, 1987). Many of these tunnels were constructed to divert subglacial water to hydroelectric stations (Clarke,

1987a). Improvements in ice drilling techniques, culminating with the hot-water drill, have permitted rapid access to the glacier bed and stimulated the development of new instruments to measure subglacial processes. Advances in instrument design, coupled with the development of reliable and inexpensive data loggers, have allowed year-round monitoring of subglacial conditions and phenomena. Numerous borehole studies have yielded direct measurements of sediment deformation (Blake and others, 1992; Iverson and others, 1995; Hooke and others, 1997; Truffer, 1999), sediment strength (Humphrey, 1993; Iverson and others, 1994; Fischer and Clarke, 1994; Iverson and others, 1995; Hooke and others, 1997; Porter and others, 1997) and glacier sliding (Harrison and Kamb, 1970, 1973; Engelhardt and others, 1978; Kamb and others, 1979; Fischer and Clarke, 1997a, 1997b). Boreholes have also allowed retrieval of till samples from beneath both alpine glaciers (Clarke and Blake, 1991; Truffer, 1999) and ice stream B, West Antarctica (Engelhardt and others, 1990; Tulaczyk and others, 2000a).

1.2 Trapridge Glacier

Field studies presented in this thesis were performed on Trapridge Glacier, a surge-type glacier in the St. Elias Mountains, Yukon Territory, Canada (Fig. 1.1). The glacier is situated on the eastern flank of Mount Wood (el. 4842 m) and ranges in elevation between approximately 2200 m and 2900 m. Trapridge Glacier covers an area of $\sim$1 by $\sim$4 km, and both surface and basal slopes average 7° in the direction of glacier flow. In the study area, which is located in the ablation zone of the glacier, ice motion averages $\sim$30 m a^{-1} in a flow direction approximately 10° north of east. The temperature profile of the glacier classifies it as sub-polar, with near-surface ice at sub-freezing temperatures and basal ice at the pressure melting point (Clarke and others, 1984; Clarke and Blake, 1991). Ice thickness averages $\sim$70 m, allowing rapid drilling to the glacier bed. The
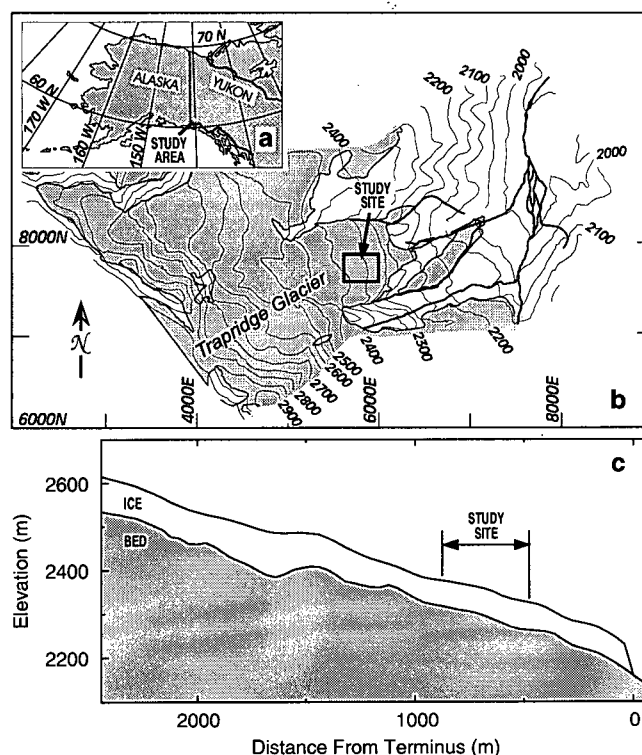
Figure 1.1: Study area. (a) Location map, southwestern Yukon Territory, Canada. (b) Trapridge Glacier, showing location of instrument study site. (c) Longitudinal profile through the centre of the study site. Note the 2× vertical exaggeration. Ice thickness along this profile ranges between ∼45 and ∼100 m and averages ∼70 m. This profile was constructed from a DEM generated by Flowers (2000) based on optical and radar surveys.

glacier is underlain by a layer of water-saturated sediments that is thought to be up to ∼10 m thick in some locations (Stone, 1993). Blake (1992) estimated that the top ∼0.30 m of the till layer is actively deforming.

Trapridge Glacier last surged at some time between 1941 and 1949 (Clarke and others, 1984). Investigations on Trapridge Glacier began in 1969, focussing on measurements of flow (Collins, 1972), temperature (Jarvis and Clarke, 1975; Clarke and others, 1984) and ice thickness (Narod and Clarke, 1980). Year-round measurements of subglacial mechanical and hydrological conditions began in 1988 in an effort to gain insight into the

mechanisms that control glacier surging.

1.2.1 Instruments

Several different instruments are used to measure hydrological and mechanical conditions beneath Trapridge Glacier. Installation of these instruments is facilitated by hot-water drilling, allowing rapid access to the glacier bed. Boreholes drilled to the glacier bed are classified as either connected or unconnected depending on whether communication with the subglacial water system is established, indicated by water level fluctuations in the borehole immediately following completion of drilling. Hydraulically-connected regions typically show strong diurnal variations in basal water pressure and mechanical responses. After installation, instruments are connected to Campbell CR10 data loggers, which are programmed to take measurements at intervals of 2 min during the summer field season and 20 min during the winter.

Subglacial water pressures are recorded by pressure transducers, which are typically suspended 0.2–2.0 m above the glacier bed. While the SI unit for pressure is the Pascal (Pa), which has units of N/m^2, subglacial water pressures are often expressed in terms of hydraulic head $p_h = p/\rho_W g$, where p is the water pressure, ρ_W the density of water and g the gravitational acceleration. Hydraulic head, which has units of metres, gives the pressure in terms of equivalent water column height. Pressures are alternately expressed in terms of the effective pressure $p' = p_I - p$, where p_I is the ice overburden pressure. The water pressure at which $p = p_I$ ($p' = 0$) is called the *flotation pressure*.

Conductivity sensors measure the electrical conductivity of the water. Because water that has been in contact with subglacial sediments will have a higher dissolved ion content than does surficial meltwater, the electrical conductivity gives a proxy for the subglacial residence time of a given body of water. Turbidity sensors measure the degree of turbidity, or cloudiness, of subglacial water. Because fast-flowing water can carry a greater sediment

load, the turbidity gives an indication of the flow rate of subglacial water (see Stone and others, 1993 for more information on conductivity and turbidity sensors). Before installation in Trapridge Glacier, pressure transducers, conductivity sensors and turbidity sensors are typically built into easily-installed "hydrology units". Hydrology units are installed approximately 0.15 m above the glacier bed.

While hydrological sensors are installed above the ice–bed interface, mechanical sensors are typically inserted ~0.1–0.3 m into the subglacial sediments. Tilt cells (Blake and others, 1992) are installed vertically in the subglacial till, and subsequent rotation gives indication of sediment deformation. Slidometers (Blake and others, 1994) measure glacier sliding in the following manner: a spool of nylon string is suspended in the borehole above the ice–bed interface, with the end secured by an anchor hammered into the subglacial till. Glacier sliding pulls the string off of the spool and turns a potentiometer. The potentiometer resistance measured at the top of the borehole is then related to the glacier sliding distance.

Sediment strength is measured by ploughmeters (Fischer and Clarke, 1996), which consist of a 1.54 m steel bar that is instrumented with strain gauges. Upon insertion into the till, relative motion between the ploughmeter and sediment results in a bending moment that is measured by the strain gauges. The bending moment is related to the sediment strength and, if till exhibits viscous behaviour, to the rate at which the ploughmeter is dragged through the till. Load bolts (Iverson and others, 1994) operate in a similar manner but measure the force acting on a body as it is dragged through the subglacial sediments.

Geophones and vertical strain sensors are installed ~15 m below the ice surface, which allows them to rapidly freeze into the glacier ice. Geophones are used to count the number of "ice quakes", or acoustic emissions, that occur per minute but give no indication of the magnitude or timing of individual events. Vertical strain sensors (Harrison and others,

1993) measure vertical compression or extension of the glacier ice. These devices measure the change in resistance of a $x.x$ m length of nickel-chromium wire. The measured change in resistance is then related to the strain $\Delta l/l$ of the wire and therefore of the encasing ice. Assuming incompressible, two-dimensional glacier flow in the study area, vertical compression (decreasing vertical strain values) indicates longitudinal extension of the ice, while vertical extension (increasing vertical strain) indicates longitudinal compression.

Although uncertainties in pressure transducer installation height lead to absolute errors of approximately 0.15 m of pressure head (1.5 kPa), the relative error for pressure transducers is limited by the data logger sampling resolution to $\sim$0.2 kPa (0.02 m). While an accurate measure of subglacial water pressure is of interest because both glacier sliding and bed deformation are strongly dependent on effective pressure, the accuracy of other instrument records is less pressing. Conductivity and turbidity sensors are used only as general indicators of subglacial water quality and thus do not require accurate calibration. Instrumental uncertainties for tilt cells, slidometers and ploughmeters are overshadowed by incertainties related to installation geometry and local basal conditions. Hot-water drilling disturbs sediments at the bottom of the borehole, leading to an uncertainty of $\sim$0.15 m in the installation depths of these instruments. Because both sediment deformation and sediment strength vary with depth in a manner that is poorly understood, it is hard to gauge how the uncertainty in installation depth influences responses of these instrument. In addition, sensor responses vary with installation location because of variations in mechanical and hydraulic conditions. Interpretation of instrument records is made with these limitations in mind, and emphasis is placed on response timing and the phase relationships between instrument signals rather than on the response magnitude.

1.3 Thesis overview
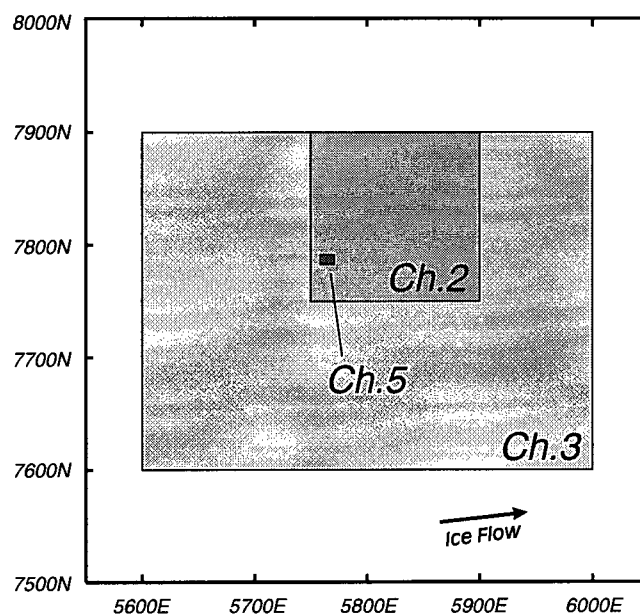
Figure 1.2: Relative locations of instrument study sites. The instruments presented in Chapter 3 were located within the 400 × 300 m area represented by the lightly-shaded region (see also Fig. 3.1c). Instruments used in Chapter 2 were located within the 150 × 150 m area represented by the middle-grey area (see also Fig. 2.2). Instruments presented in Chapter 5 were located in the small 12 × 8 m area shaded dark grey (see also Fig. 5.2c).

In the following chapters I present the results of investigations into the hydromechanical behaviour of a surge-type glacier. Central to these investigations are *in situ* instrument measurements, which allow direct examination of the subglacial environment. In each of the studies presented here, interpretations are based on simultaneous measurements made by a number of different instruments. Incorporating information from a variety of instruments allows us to draw a more complete picture of subglacial conditions and provides constraints by which we can narrow the range of the possible interpretations. Because the information contained in an individual instrument record is limited to one

aspect of subglacial conditions at one specific location, only within the context of other records can an individual instrument record provide useful information about subglacial phenomena. In the studies presented in this thesis, I have attempted to incorporate information from all available instrument records. The relative study area locations for the studies presented in Chapters 2, 3 and 5 are shown in Figure 1.2. All three instrument studies are contained within an area covering approximately 300 m by 400 m.

In Chapter 2 I present evidence for transient high-pressure pulses in the subglacial drainage system. These previously-undetected pulses are indicated in the records for several pressure transducers on 20 July, 1996 by sudden offsets in the measured pressure. The offsets are attributed to permanent deformation of the transducer measurement diaphragm. I present laboratory studies that show that subjecting a pressure transducer to pressures well above their design limit effectively resets the calibration parameters and produces measurement offsets similar to those observed in field records. Model simulations of these calibration offsets yield responses that are qualitatively similar to pressure transducer records from Trapridge Glacier. Analysis of records from other hydrological and mechanical instrument records suggests that transient high-pressure pulses could be generated by abrupt glacier motion that compresses or dilates the subglacial hydraulic system.

Chapter 3 contains an analysis of records from a large number of mechanical and hydrological instruments taken during early summer 1995. These records reveal that a series of subglacial hydromechanical events occurred following the establishment of a subglacial drainage system at the beginning of the summer melt season. Pressure fluctuations in the drainage system weakened a region of the bed that was acting as a local pinning point, resulting in three episodes of strong basal motion. Abrupt offsets in several pressure transducer records suggest that basal motion during the events generated extreme pressure pulses similar to those discussed in Chapter 2. Although previous "spring events"

have been noted at Trapridge Glacier (Stone, 1993; Stone and Clarke, 1996) and else-
where (Iken, 1983; Röthlisberger and Lang, 1987; Harbor and others, 1997; Gordon and
others, 1998), this event is of particular interest because it was captured by more than
forty instruments representing several different types, allowing clear characterization of
both the hydrological and mechanical responses. The event occurred prior to our return
to the glacier in July 1995 and the demonstrates the success of year-round monitoring of
subglacial conditions at Trapridge Glacier.

The instrument records presented in Chapters 2 and 3 capture what might be called
"experimental moments", moments when conditions beneath the glacier conspire to gen-
erate simultaneous responses in a large number of instrument records. Inspection of the
Trapridge Glacier data archive reveals that such moments are relatively rare and are
typically associated with brief hydromechanical adjustments or events. Thus while these
experimental moments provide valuable insight into the nature of interactions between
mechanical and hydrological conditions under unusual circumstances, they reveal little
about normal subglacial conditions. In order to investigate typical diurnal variations in
mechanical and hydrological conditions, I develop a simple hydromechanical model of the
processes governing basal motion of a soft-bedded alpine glacier. For the model, which I
develop in Chapter 4, the glacier bed is classified into three general regions: soft-bedded
and hydraulically-connected to the subglacial drainage system, soft-bedded but poorly
connected, and hard-bedded. Each basal region is modelled as a single one-dimensional
column. The time-evolution of pore-water pressure, till dilatancy, sediment deformation
and glacier sliding is calculated in the soft-bedded regions; the hard-bedded region is
considered rigid and impermeable. The regions are coupled by a simple ice-dynamics
model, allowing investigation of the effects of shear stress bridging between regions. I
also develop models describing instrument responses to the modelled subglacial hydro-
logical and mechanical conditions. Individual instrument responses have been modelled

by Fischer (1996) and Fischer and Clarke (1994, 1997a, 1997b); this model is the first to incorporate synthetic instrument responses into a comprehensive model of hydromechanical behaviours and the first to calculate simultaneous responses for several instrument types.

In Chapter 5, I apply the coupled three-column hydromechanical model developed in Chapter 4 to the discrimination of proposed till flow laws. Initial and boundary conditions are chosen to mimic typical summer-mode conditions at Trapridge Glacier, Yukon Territory, Canada. I present modelled pore-water pressure and deformation profiles for four constitutive relations that have been proposed in the literature to describe the flow behaviour of till: linear-viscous, nonlinear-viscous, nonlinear-Bingham and Coulomb-plastic. I compare the magnitude and phase relationships of synthetic instrument responses for each flow law with *in situ* measurements of basal water pressure, pore-water pressure, sediment strain rate, basal sliding and sediment strength recorded at Trapridge Glacier recorded during July 1996. These records comprise the first successful simultaneous measurement of basal pressure, deformation, sliding and sediment strength conditions under any glacier. Comparison of synthetic responses with field records allows determination of the flow law that provides the best qualitative match to observed variations in hydrological and mechanical conditions beneath Trapridge Glacier.

Chapter 2

Evidence for extreme pressure pulses in the subglacial water system

2.1 Introduction

I present a suite of subglacial instrument records taken during the summer 1996 field season at Trapridge Glacier. Interpreted literally, these records provide evidence for a hydraulic transformation that seems impossible to reconcile with current understanding of subglacial processes. Although strong responses were recorded by the majority of pressure transducers, other sensors were unaffected by the event or recorded only minor signals. The paradoxical instrument records can be explained by transient pressure pulses in the subglacial water system. Exposure to such a pressure pulse can permanently deform the measurement diaphragm of a transducer, causing an apparent shift in calibration. In field records, this calibration shift would appear as a pressure jump that might be difficult to distinguish from hydraulically-plausible behaviour. In order to investigate this failure mechanism, laboratory studies were performed to determine the effect of overpressurization on pressure transducers. These studies confirm that exposing a transducer to pressures above the specified measurement range can cause resetting of calibration parameters and allow estimation of the pulse magnitudes required to produce the observed offsets. Modelling the transducer response to calibration parameter changes similar to those observed during laboratory testing yields responses that are qualitatively similar to field records from Trapridge Glacier. Analysis of records from other hydrological and mechanical instruments suggests that the transient water pressure pulses could

13

be generated by abrupt glacier motion that compresses or dilates the subglacial hydraulic system. In the instrumented region, mechanical signals lag the pressure changes by several minutes, implying that the inferred pressure pulses may induce basal motion.

2.2 Observations
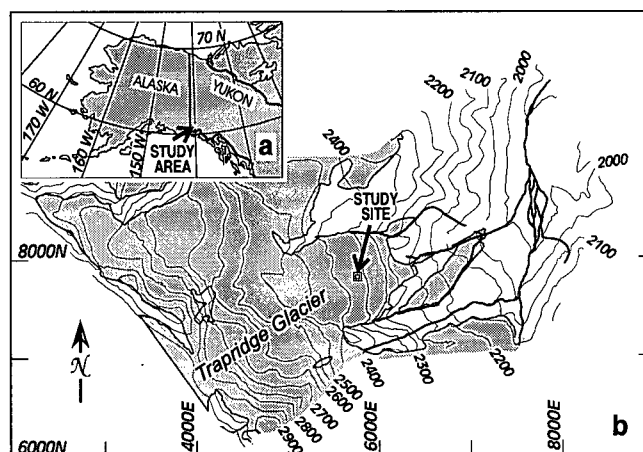
Figure 2.1: Study area. (a) Location map, southwestern Yukon Territory, Canada. (b) Trapridge Glacier, showing location of instrument study site.

Since 1988, year-round measurements of water pressure have been recorded beneath Trapridge Glacier, Yukon Territory, Canada (Fig. 2.1a, b) in an effort to broaden understanding of subglacial hydraulic phenomena (see Clarke and Blake (1991) for background information and references). Fourteen pressure transducers were in operation on 20 July 1996. Map locations for the six pressure sensors detailed in this study are presented in Figure 2.2. Five of the six pressure sensors were installed during July 1996; the sixth was installed in July 1995 and its position has been corrected for glacier motion. Four pressure sensors that were placed in hydraulically-connected regions of the bed, as indicated by water level fluctuations in the borehole immediately after drilling was completed, are identified as C1–C4; the two sensors that were placed in hydraulically-unconnected
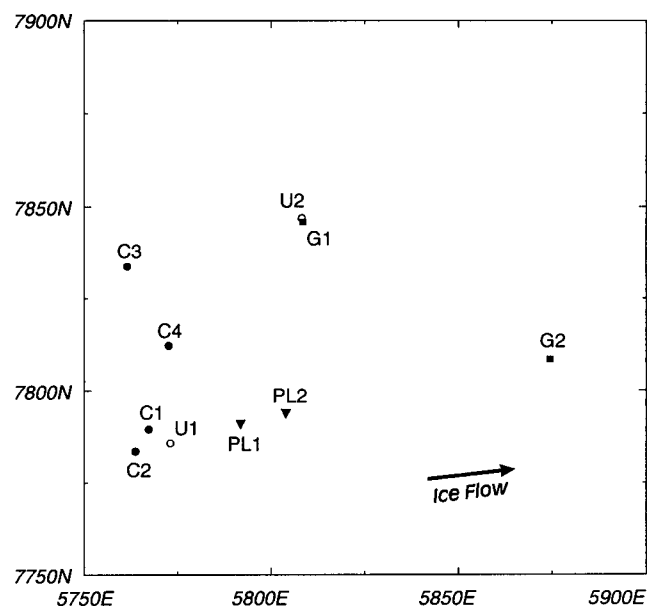
Figure 2.2: Study site. Coordinates are given in metres Easting and North-
ing, with positions of instruments installed in 1995 corrected for glacier flow.
Pressure transducers installed in connected regions are labelled C1–C4; un-
connected transducers are labelled U1 and U2 (see text for explanation of
connection status). Ploughmeters are labelled PL1 and PL2, and geophones
are labelled G1 and G2.

holes are denoted U1 and U2. These designations do not necessarily correspond to the

connection status at later times. Also included in Figure 2.2 are corrected locations

for two ploughmeters, installed in July 1995 and labelled PL1 and PL2, and two 1996

geophones, designated G1 and G2. As discussed in Chapter 1, pressure transducers

are typically built into hydrology units combining pressure, conductivity and turbidity

sensors prior to installation in Trapridge Glacier. In these units, the pressure sensor is

situated slightly up-hole from the other sensors and all sensors share a common signal

wire. Hydrology units are installed approximately 0.15 m above the bed. Transducers

installed in-hole with ploughmeters (Fischer and Clarke, 1994) are placed ~2 m above the

bed. Boreholes typically freeze closed near the surface within a day or so, thus confining

the instruments in a closed, water-filled space.
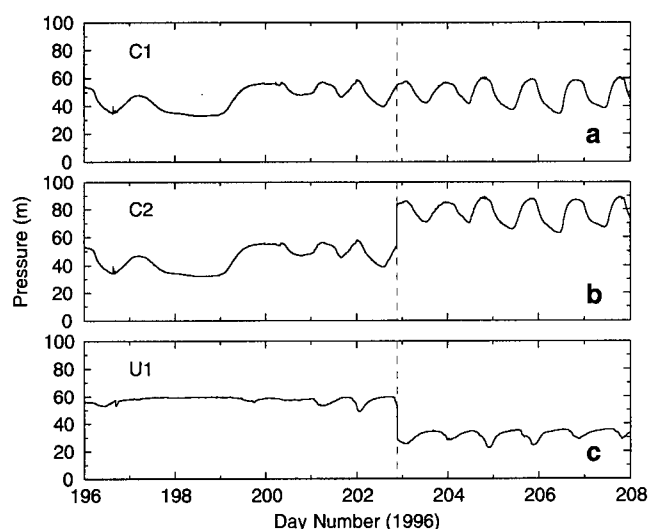
Figure 2.3: Pressure records. Day 196 corresponds to 14 July 1996. Pressure values are expressed in terms of equivalent water column height. Vertical dashed lines represent 2120 h on day number 202. (a) Connected transducer C1. (b) Connected transducer C2. (c) Unconnected transducer U1.

Figure 2.3 shows 12-day records for three pressure transducers installed less than 10 m apart (Fig. 2.2). Pressures are expressed in terms of hydraulic head $h = P/\rho_W g$, where P is the water pressure, ρ_W the density of water and g the gravitational acceleration. Pronounced changes in pressure are recorded by sensors C2 and U1 near the end of day 202. The pressure records of C1 and C2 (Fig. 2.3a and 2.3b, respectively) show close agreement for the first seven days of observation. Pressure values indicated by C1 are consistently 0.72 m higher than those for C2, even for high-frequency pressure fluctuations that are barely discernible on the two records. Peak pressures are close to the local ice flotation value of ~60 m. At 2120 h on day 202 the pressure record for C2 shows a sharp increase of 29.7 m, while that for C1 gives no indication of this jump. Subsequently, the pressure records continue to show close agreement in both diurnal variation and

fine detail, but with a pressure offset of $+28.5$ m for C2, indicating peak pressures well above flotation. The pressure record for U1 (Fig. 2.3c) shows a diurnal signal having lower amplitude and opposite phase to those for C1 and C2. Such contrasts between the behaviour of connected and unconnected regions are not unusual and result from the transfer of mechanical support of ice overburden between the two regions as the water system pressure varies (Murray and Clarke, 1995; Gordon and others, 1998). At 2120 h on day 202, coincident with the abrupt change in the pressure record for C2, sensor U1 indicates a pressure drop of 23.9 m. The diurnal character of the record is unaffected by this pressure step.

Twelve of the fourteen pressure transducers in operation 20 July 1996 recorded abrupt changes at the time of the event that affected sensors C2 and U1. Responses ranged from a pressure increase of 0.5 m recorded by one sensor to the apparent failure of three transducers, and were recorded throughout the 200 m $\times$ 250 m instrumented study area. Figures 2.4a–c details records for the six pressure transducers shown in Figure 2.2 over a 3-day period spanning the hydraulic event. These records demonstrate the wide range of responses seen in pressure records at the time of the event. Pressure records for C2 and C3 are shown in Figure 2.4a with that for C1, the unaffected sensor, included as a reference. Sensor C3 was installed $\sim$45 m cross-glacier from C1 (Fig. 2.2). All three boreholes were connected to the subglacial hydrological system at the time of drilling. Despite the distance between sensors, C2 and C3 show comparable behaviours: (i) initially, both pressure signals have similar form but are slightly offset from that of C1 (-0.72 m for C2; $+3.0$ m for C3); (ii) C2 and C3 exhibit large jumps in recorded pressure at 2120 h on day 202; (iii) subsequent pressure fluctuations are very similar to that of C1 but with large offsets ($+28.4$ m for C2, $+55.2$ m for C3).

Pressure records for U1 and U2 are shown in Figure 2.4b. Both instruments were installed in boreholes that were hydraulically-unconnected to the drainage system at the
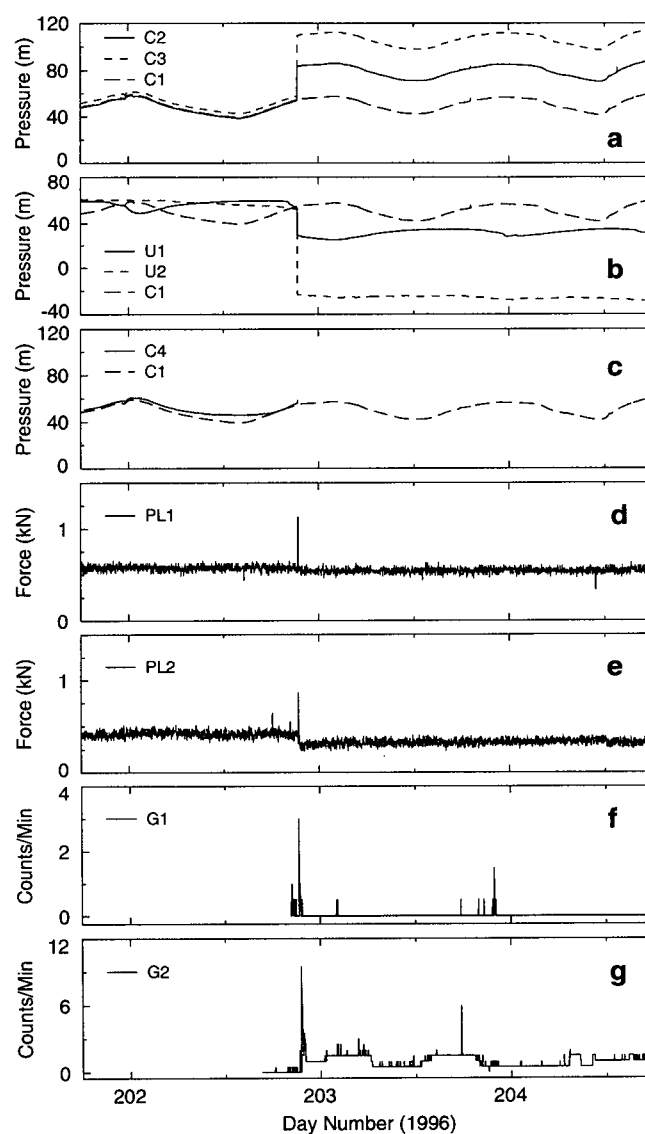
Figure 2.4: Detailed instrument records. (a) Time series plots for connected transducers C2 (solid), C3 (short dashed) and C1 (long dashed). (b) Unconnected transducers U1 (solid) and U2 (short dashed), compared to C1 (long dashed). (c) Comparison of C4 (solid) to C1 (dashed). Failure of C4 occurs at 2120 h on day 202. (d) Force record for ploughmeter PL1. Transient peak occurs at 2124 h, day 202. (e) Force record for PL2. Transient peak occurs at 2124 h, day 202. (f) Geophone G1. Small peak occurs at 2122 h, day 202. (g) Geophone G2. Small peak noted at time of event; larger peak of $9.5\,\text{min}^{-1}$ occurs at 2134 h, day 202.

time of drilling. Sensor U2 was installed ~70 m down-glacier from C1 (Fig. 2.2). The unconnected records exhibit higher ambient pressures and lower variability than those for the connected holes. Coincident with the pressure increases of C2 and C3, both sensors show marked decreases in pressure, with U2 recording negative pressure values after the drop. All pressure decreases associated with the event were recorded by transducers installed in unconnected regions of the bed, whereas the majority of connected sensors exhibited positive pressure jumps at the time of the event.

Figure 2.4c compares the response of C1 to C4, a transducer installed in 1995. The advected position of C4 is calculated from surface flow measurements. The two records show similar diurnal character, indicating C4 is sampling a connected region of the bed, though the damped diurnal signal of C4 suggests an imperfect hydraulic connection with C1. Failure of C4 occurs at the time of the sudden pressure change observed by the other sensors. Two of the three event-related transducer failures were of sensors installed in connected regions of the bed.

In contrast to the strong responses recorded by pressure transducers, other instruments showed only minor responses to the event. No conductivity or turbidity records exhibit changes at the time of the event; similarly, none of the tilt cells or slidometers (Blake and others, 1994) recorded any event response. Of the fourteen ploughmeters installed, two displayed small transient responses shortly after the event. Ploughmeters PL1 (Fig. 2.4d) and PL2 (Fig. 2.4e) were installed in 1995. Their positions, corrected for glacier flow, are shown in Figure 2.2. Records for ploughmeters are characterized by low, steady force values, averaging 0.56 kN for PL1 and 0.41 kN for PL2. Both ploughmeters recorded small transient peaks 4 min after the event, measuring 1.13 kN for PL1; 0.87 kN for PL2. Both ploughmeters return to steady forcings after the transient peak, with PL2 measuring a slight reduction in force at 0.28 kN. Five of the eight geophones produced increased count rates near the time of the event. Although three geophones

registered counts during the event interval, peak count rates occurred 2–20 min after the event. Icequake count rates for geophones G1 and G2 are shown in Figures 2.4f, g. Both geophones were installed on day 201 and were allowed to freeze into the glacier ice before being connected to data loggers on day 202; their locations are shown in Figure 2.2. While no counts are measured by G1 during the 2 min interval preceding the event, a small peak of $3 \, \text{min}^{-1}$ is recorded immediately afterward (Fig. 2.4f). Counts are recorded for a 24 min period following the event. Sensor G2 (Fig. 2.4g) registers a small peak of $2 \, \text{min}^{-1}$ during the interval immediately prior to the event, followed by a count rate of $9.5 \, \text{min}^{-1}$ 14 min later. Elevated count rates continue until approximately 46 min after the event.

2.3 Interpretation

The instrument records presented in Figures 2.3 and 2.4 suggest an event having both hydrological and mechanical components. Timing of the various sensor responses suggests that, at least in the instrumented region of the bed, the hydrological signal preceded the mechanical response by several minutes. I therefore focus on the pressure transducer records, and explore the implications of two alternative interpretation hypotheses: (i) that the curious behaviour can be explained in terms of a rapid and sustained change in the subglacial drainage morphology, and (ii) that rapid and extreme water pressure variations, undetected because of the 2 min sampling interval of our data loggers, have reset the calibrations of four of the five sensors subjected to the extreme event.

2.3.1 Drainage morphology implications

Individually, the three pressure records presented in Figure 2.3 imply plausible changes in the local subglacial water pressure. Taken together, they suggest the occurrence of an

intriguing hydrological switching event that led to highly-localized reorganization of the subglacial water pressure field. In Figure 2.4a, the small initial pressure offsets can be attributed to differences in bed elevation or errors in measurement of transducer install-ation depth. Similarities in the pressure signals, including both diurnal and small-scale character, indicate the presence of an efficient hydraulic connection between boreholes both before and after the event. Weakening of this connection during the event would result in differences in amplitude or phase of the diurnal signal between sensor records or reduced coherence of small-scale features. Instead, following the switching event, the three pressure records of Figure 2.4a show nearly identical waveforms but with large constant pressure offsets.

Figure 2.5 illustrates a hydraulic reorganization that could account for the observed features in the records of C1, C2 and C3. For clarity, the system is represented by water pipes and shows three branches of a subglacial drainage system, each branch representing a region measured by an individual pressure transducer. The similar elevation and strong hydraulic connection evident in the pipe circuit of Figure 2.5a would ensure uniform re-sponses to variations in pressure head and could therefore reproduce the essential features of the pre-event records for C1, C2 and C3. Switching to the pipe geometry shown in Figure 2.5b would produce offsets resembling those of the observed post-event records. Lowering two of the branches by distances Δh_2 and Δh_3 yields pressures $P_2 = P_1 + \Delta h_2$ and $P_3 = P_1 + \Delta h_3$. Pressure P_1 is unaffected by the event. The low-resistance pipe allows the strong hydraulic connection to be maintained, and thus each transducer meas-ures similar pressure fluctuations while exhibiting large offsets. Although this simple scenario reproduces the main features of the connected sensor records, it cannot occur subglacially. The pipes shown in Figure 2.5 represent drainage pathways at the bed of the glacier, and thus the sudden drops in elevation of 29.2 m and 52.2 m indicated in the

records of C2 and C3 would place both the drainage channels and the pressure trans-
ducers deep within the glacier bed. While up-thrusting of the sensors is a conceivable
process, but down-thrusting *through the bed* is certainly not.
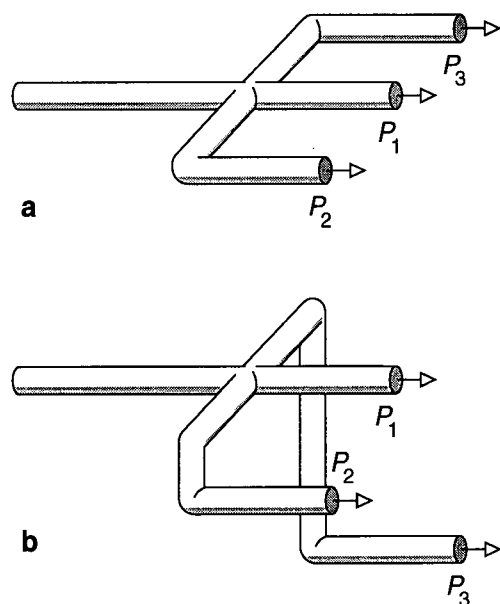
Figure 2.5: Schematic diagram showing hydraulic connections which could
explain the pressure records of transducers C1, C2 and C3. (a) Before event.
(b) After event.

Subglacial pressure signals have been attributed to both hydrological forcings, includ-
ing changes in meltwater input and drainage morphology (e.g. Fountain, 1994; Walder
and Fowler, 1994; Clarke, 1996), and mechanical forcings, such as the transfer of over-
burden pressure between regions of the bed (Murray and Clarke, 1995). The failure of
current hydrological models to explain the transducer records compels us to ask whether
the observed offsets are maintained by forcings that have thus far eluded understanding,
or if the signals can be more simply attributed to other causes, such as instrument fail-
ure. The record for transducer U2 argues in favour of the latter explanation. Sensors

U1 and U2 (Fig. 2.4b) were installed in hydraulically-unconnected regions of the bed, and both records exhibit low-amplitude pressure variations that are out-of-phase with those of C1–C4. At the time of the switching event, both sensors record large pressure decreases, measuring -23.9 and -75.4 m, respectively. The character of the diurnal variations in each case is unchanged by the event. While U1 records reasonable pressure values following the event, the negative post-event values recorded by U2 suggest instrument failure and raise several questions: (i) Are the other observed pressure jumps due to device failure? (ii) If so, what is the failure mechanism? (iii) Is this mechanism also responsible for the failure of C4?

2.3.2 Implications of covert sensor failure

In order to discuss the failure of pressure sensors, it is first necessary to describe their operating principles. A schematic diagram of the transducer (Gems Sensors Series 2000, 16 bar absolute) is shown in Figure 2.6. Variations in water pressure deflect the measurement diaphragm, which in turn bends the sensor beam (Fig. 2.6a). Pressures are measured relative to a sealed reference chamber (Fig. 2.6b). Transducer response is highly linear with changes in water pressure over the 1.62 MPa measurement range, and thus the relation $V = a_0 + a_1 h$, which I refer to as the sensor response equation, provides an excellent fit to the calibration data. Here V is the output of the transducer measured in millivolts and h the hydraulic head, expressed in metres above the bed. To determine the pressure head for a given transducer output, the sensor response equation is inverted to give the sensor calibration equation $h = b_0 + b_1 V$ where, self-evidently, $b_0 = -a_0/a_1$ and $b_1 = 1/a_1$. An operating voltage of 2.5 V was used for all field measurements and laboratory studies, and data were recorded using a sampling interval of 2 min on Campbell CR10 data loggers.

The event affected a large number of transducers, covering a large area and connected
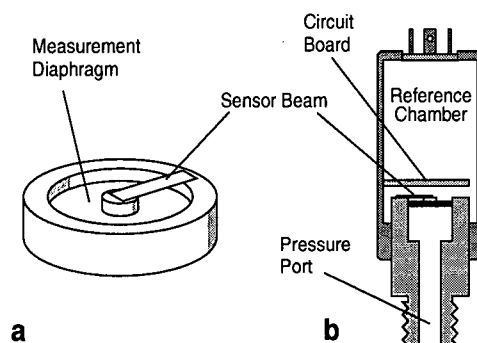
Figure 2.6: Schematic diagram of pressure transducer. (a) Detail of measurement diaphragm and sensor beam. Shown at approximately 2x scale. (b) Cross section. Shown at approximately 1/2 scale.

to several different data loggers; thus the failures cannot be attributed to simple electrical problems. Lightning strikes, which could potentially affect several loggers simultaneously, would be expected to induce some signature in turbidity and conductivity records as well. Such signals are not observed. Three of the six pressure transducers involved in this study were incorporated into hydrology units. While the turbidity and conductivity sensors installed with C4 were disconnected prior to the event and thus give no indication of the failure mode, those sensors installed with C3 and U2 were operating at the time, and no reflection of the event is evident in these records. Thus crushing of the instruments or wire breakage could not explain the observed pressure records.

I propose a mode of transducer failure that reconciles the seemingly incompatible instrument records. Transient high-pressure pulses, having peak pressures well above the specified transducer measurement range, can impose a permanent strain on the measurement diaphragm. This damage results in an effective shift in the response coefficients a_0 and a_1. Recalibration of a transducer after exposure to a high pressure pulse would yield new values of calibration coefficients b_0 and b_1. However, because the original values continue to be used, the calculated pressure fluctuations have incorrect amplitude and

offset.

I conducted a series of laboratory experiments to test the validity of the failure hypothesis. Two pressure transducers, identified as PT1 and PT2 and of identical manufacture to those installed in Trapridge Glacier, were calibrated over the range 0–700 kPa (0–71.4 m) at 100 kPa (10.2 m) intervals (all pressures measured relative to atmospheric). Two measurements were taken at each calibration point, first as the pressure was increased from atmospheric to the maximum value and then again as it was released. The lack of hysteresis in these data indicates that the calibration was unaffected by fluctuations in ambient temperature or by adiabatic heating of the air pressure chamber during testing. After calibration, the transducers were subjected to static pressure values of 1200 kPa to 17 000 kPa (122 m to 1730 m) at intervals of 500–1000 kPa (51–102 m) using a hydraulic hand pump (Enerpac Model P-39). These values represent pressures well above both the rated transducer pressure limit of 1600 kPa and typical ambient subglacial pressures of 300–800 kPa measured beneath Trapridge Glacier. The pressures were sustained only long enough to record the transducer output (typically 0.5–1.5 min). I shall refer to the extreme pressure head P^* to which a transducer has been subjected as the inherited extreme pressure or "damage pressure". This quantity will be expressed interchangably in units of pressure (kPa) or pressure head (m). Accepting the sensor failure hypothesis, the sensor response equation is rewritten as $V = a_0(P^*) + a_1(P^*)h$, where the damaged sensor response parameters are assumed to depend on the device history, encapsulated in P^*.

The transducers were recalibrated each time that the damage pressure was increased, and changes in response parameters a_0 and a_1 were noted. Output voltages are plotted against calibration pressure for PT1 and PT2 in Figures 2.7a and 2.7b, respectively. Each line represents a sensor calibration performed at successively higher values of damage pressure. After being subjected to high damage pressures, both transducers yielded an

increased voltage response for a given calibration pressure. This results in an upward shift of the calibration line and effectively changes a_0 to a greater value. Visual inspection of the measurement diaphragm between calibrations did not reveal obvious damage to the measurement diaphragm, likely because (i) the magnitude of the permanent strains was small and (ii) inspection was hampered by the fact that the diaphragm is located deep within the transducer body (Fig. 2.6). Ultimate failure of both test instruments was due to measurement diaphragm rupture.
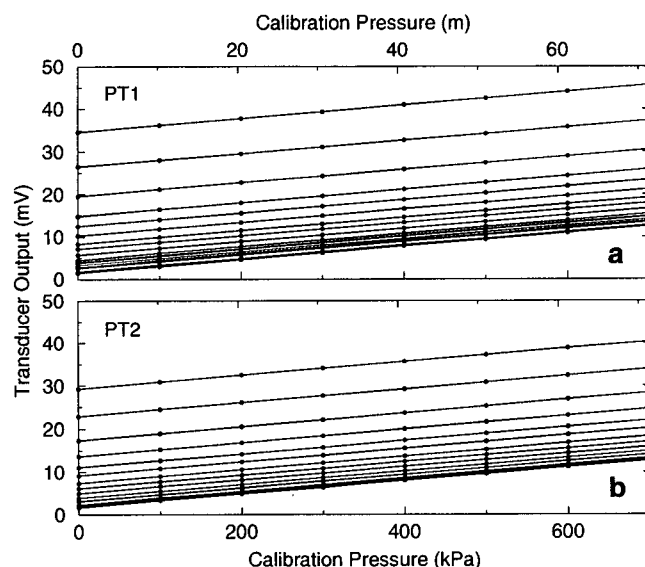
Figure 2.7: Repeated calibration data. Transducers were exposed to an increased damage pressure between calibrations. (a) PT1. (b) PT2.

If the calibration line is shifted sufficiently, the transducer can produce output voltages that are greater than the maximum value measurable by the data logger. As programmed for our experiments, the Campbell data logger cannot measure voltages exceeding $\sim27\,\mathrm{mV}$. Figure 2.7 shows that damage pressures greater than approximately $15\,000\,\mathrm{kPa}$ ($1530\,\mathrm{m}$) can cause calibration shifts sufficient to yield out-of-range output voltages for typical values of subglacial water pressure for Trapridge Glacier. The failure

of C4 (Fig. 2.4c) could thus also be explained by a large pressure pulse.

If the ambient hydraulic head is $h = 0$ m, the damaged sensor response equation yields a voltage of $V = a_0(P^*)$. Applying this voltage to the sensor response equation gives an indicated hydraulic head $P^* = b_0 + b_1 a_0(P^*)$, which for damaged sensors differs from $P = 0$ m and constitutes a calibration offset. Figure 2.8a plots this calibration offset h^* against damage pressure. Shifts are first observed at damage pressure as low as 2000 kPa (205 m). Below $\sim$4000 kPa (410 m), increases in damage pressure produce small calibration shifts (see inset, Fig. 2.8a). Above this threshold, increases in damage pressure result in large calibration offsets; for both sensors the form of the relationship approximates an exponential increase in $a_0(P^*)$ with increasing damage pressure. If transducers installed in Trapridge Glacier fail in a comparable manner, we can estimate the magnitude of the pressure pulses responsible for the offsets in the records of C2 and C3 from these experimental results. The 29.2 m shift in the time series of C2 corresponds to a pulse on the order of 9000–11 000 kPa (900–1100 m), with the 52.2 m shift of C3 requiring a pulse of approximately 11 000–13 000 kPa (1100–1300 m). If we attribute the failure of C4 to pressure-induced calibration shift to an off-scale value, Figure 2.8a suggests that the pulse pressure was greater than $\sim$15 000 kPa (1500 m). While the transducers in this experiment were subjected to multiple damage pressures of increasing value, calibration shifts observed in field records likely result from a single pressure pulse. Thus the calibration offset behaviour of a transducer installed in the field might differ from those observed in this laboratory study.

The parallel nature of the calibration lines in Figure 2.7 suggests that the slope of the calibration line (calibration coefficient a_1) does not change significantly with increasing damage pressure. Figure 2.8b plots the calibration line slope against damage pressure. The pre-damage ($P^* \sim 0$) values of the calibration slope for the two transducers are very similar at $a_1(0) = 0.1551$ mV m^{-1} for both PT1 and PT2. With increasing damage

pressure, PT1 shows a small overall decrease in value while PT2 varies slightly around the initial pre-damage value. The maximum deviation of a_1 during damage pressure testing for PT1 occurs at $P* = 5700\,\mathrm{kPa}$, with $a_1(P^*) = 0.1534\,\mathrm{mV\,m^{-1}}$; the maximum deviation of PT2 gives $a_1(P^*) = 0.1546\,\mathrm{mV\,m^{-1}}$ at $P^* = 16\,000\,\mathrm{kPa}$. These values represent changes in slope of -1.07% and -0.35%, respectively, and may indicate strain hardening due to diaphragm damage (personal communication, P. Jansson, 1999). The calibration constants b_0 and b_1 of the sensor response equation are calculated from the initial pre-damage calibration values $a_0(0)$ and $a_1(0)$, and thus any change in $a_1(P^*)$ results in the scaling of the apparent magnitude of a given pressure signal by the factor $a_1(P^*)/a_1(0)$. For example, a pulse of magnitude $P^* = 5700\,\mathrm{kPa}$, would reduce the response of sensor PT1 to a $20\,\mathrm{m}$ pressure fluctuation by $0.215\,\mathrm{m}$ (-1.07%).
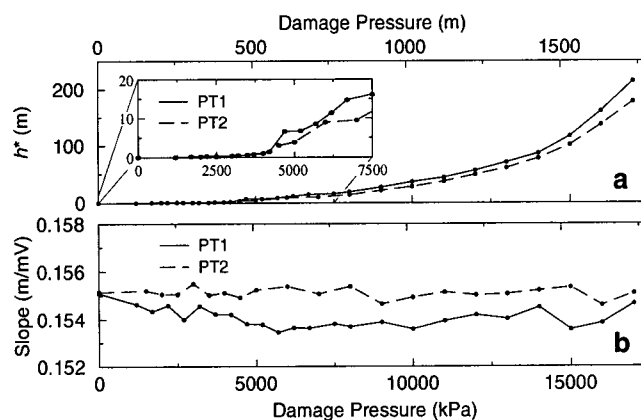
Figure 2.8: (a) Plot of calibration offset h^* against damage pressure for PT1 (solid) and PT2 (dashed). (Inset) Detail of calibration shift at low damage pressures. (b) Plot of calibration slope value against damage pressure.

As a consequence of the effective changes in a_0 and a_1, the record of an instrument subjected to a high-pressure pulse would appear to abruptly jump to a higher ambient pressure while the magnitude of diurnal and small-scale fluctuations would change only

slightly. Although sudden pressure jumps are easy to recognize in instrument records, small changes in the amplitude of pressure fluctuations are difficult to discern unless the record for an undamaged transducer is available for comparison. Sensors C2 and C1 provide such a complementary pair of field records. Figure 2.9 plots the pressure difference between the two sensors, $\Delta P = P_{C2} - P_{C1}$. The pressure record of C1 (dashed line) is shown for comparison. Prior to the event of 2120 h on day 202 (Fig. 2.9a), C2 registers pressures approximately 0.72 m lower than those measured by C1. Slight deviations from this value (e.g. accompanying the large pressure increase on day 199 and at peak pressure on days 201 and 202) show no systematic relationship between P_{C1} and ΔP. After the event (Fig. 2.9b), ΔP varies sinusoidally around 28.4 m with a peak-to-peak amplitude of 0.154 m. This variation is out-of-phase with P_{C1} and suggests a slight decrease in post-event sensitivity to the 24.9 m diurnal pressure variation measured by C2. The measured difference of -0.151 m suggests a pressure pulse-induced deviation in a_1 of -0.606%, comparable in value to changes exhibited by the transducers during laboratory testing.
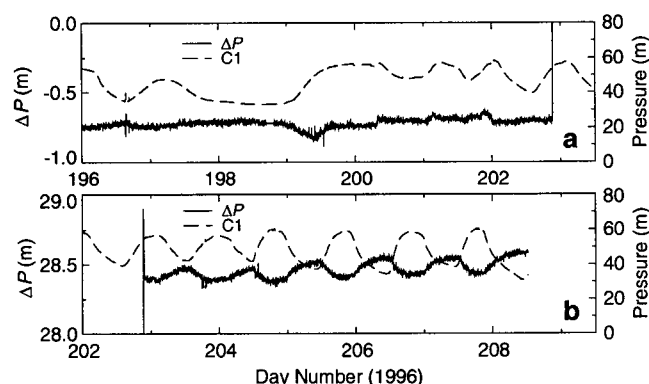
Figure 2.9: Pressure difference between C2 and C1. Time series for C1 (dashed) is shown for comparison. (a) Detail before event. (b) Detail after event.

To further investigate this behaviour, I model the response of PT1 to a diurnal sinusoidal pressure fluctuation that varies between $40\,\text{m}$ and $60\,\text{m}$ (Fig. 2.10a). The voltage response is calculated by applying the pre-damage values $a_0(0) = 1.4316\,\text{mV}$ and $a_1(0) = 0.1551\,\text{mV}\,\text{m}^{-1}$ to the damaged sensor response equation. Substituting the resulting voltage into the sensor response equation, with $b_0 = -a_0(0)/a_1(0)$ and $b_1 = 1/a_1(0)$, yields the calibrated instrument output. To simulate the occurrence of a $P^* = 9000\,\text{kPa}$ ($918\,\text{m}$) pressure pulse at $0000\,\text{h}$ on day 5, I calculate the voltage response of the transducer by switching to the appropriate values of $a_0(P^*) = 5.675\,\text{mV}3$ and $a_1(P^*) = 0.1539\,\text{mV}\,\text{m}^{-1}$ in the damaged sensor response equation. This results in a post-event jump of $+27.0\,\text{m}$ in the calibrated output. Figure 2.10b details ΔP before the modelled pulse. Because the values $a_0(0)$ and $a_1(0)$ are used both in determining the transducer voltage response and calculating the corresponding pressure, the transducer accurately records the forcing pressure and thus $\Delta P = 0$. Similarly, the pre-event field records of C1 and C2 (Fig. 2.9a) show a nearly constant value of ΔP. Figure 2.10c details ΔP after the occurrence of the modelled damage pulse at the onset of day 5. The post-pulse change in a_1 of -0.796% results in a response that is $0.159\,\text{m}$ smaller than the $20\,\text{m}$ forcing. This results in a pressure difference ΔP that varies sinusoidally around $+27.0\,\text{m}$ and is out-of-phase with the forcing pressure (dashed line). Comparison with the post-event field records of C1 and C2 (Fig. 2.8b) reveals very similar behaviour.

Although the post-event amplitude reduction recorded by C2 could be explained by a change in the subglacial hydraulic system, the extreme linearity of the effect over the full range of the diurnal pressure variation suggests an instrumental cause. The remarkable similarities between the field records of C2 and C1 and the modelled pressure response of PT1, coupled with the unlikely nature of the hydraulic switching necessary to create the aggregate pressure records, strongly support attribution to transducer failure.

Further evidence for this mode of transducer failure is provided by transducer PR1
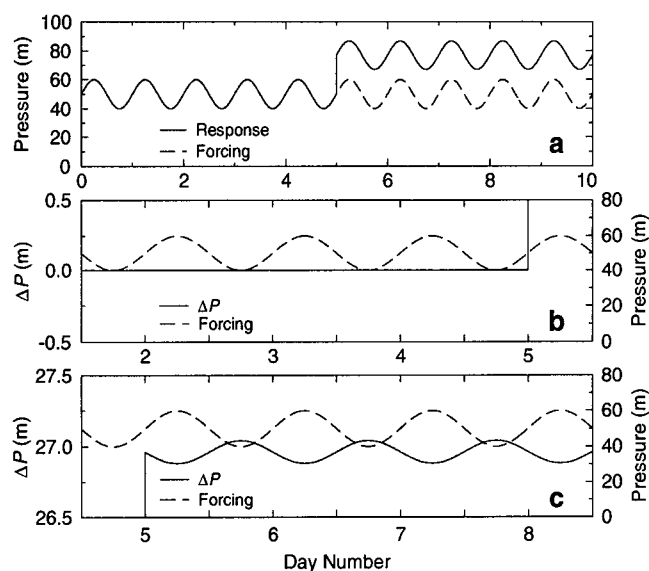
Figure 2.10: (a) Modelled response of PT1 to a sinusoidally-varying pressure function with a 9000 kPa (918 m) pressure pulse at 0 h on day number 5. The modelled input pressure is plotted as a dashed line. (b, c) Pressure difference between modelled instrument response and input pressure. Input pressure (dashed) shown for comparison. (b) Detail before pulse. (c) Detail after pulse.

(Fig. 2.11). This transducer was installed during the 1997 field season and retrieved during July 1999. The pressure record for this transducer during the winter of 1998 is shown in Figure 2.11a. A brief pressure spike is observed at 0500 h of day 241 (29 August) 1998, followed by an abrupt drop of 188.0 m. Indicated pressures following this drop measure between −136 and −143 m. At 2020 h on day 68 (9 March) of 1999, an abrupt increase of 60.7 m is indicated in the record. This transducer was recovered during the 1999 field season and subsequently recalibrated. Comparison of pre-installation calibration line (Fig. 2.11b, solid line) with that obtained following retrieval (Fig. 2.11b, dashed line) reveals changes similar in character to those observed during the laboratory studies presented
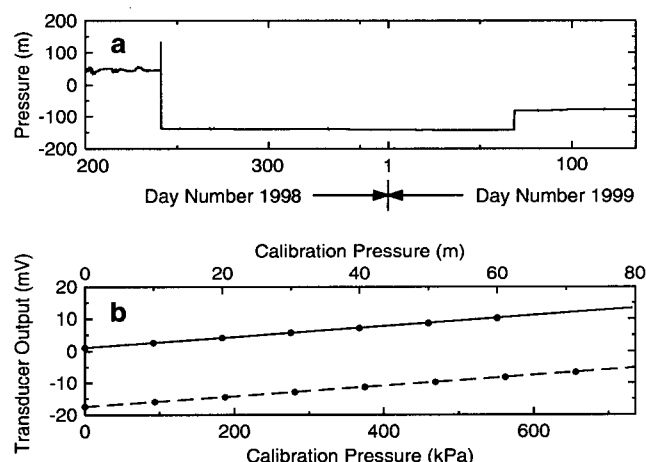
Figure 2.11: (a) Field record during winter 1998 for recovered pressure transducer PR1. Day 200 corresponds to 19 July 1998. Following a brief pressure spike, an abrupt pressure change of -188.0 m is indicated at 0520 h on day 241 (29 August) 1998. A pressure jump of $+60.7$ m is noted at 2020 h of day 68 (9 March) of 1999. (b) Repeated calibration data for pressure transducer PR1. The solid line represents the original calibration performed prior to installation in Trapridge Glacier. The dashed line represents a laboratory calibration performed after the transducer was recovered from Trapridge Glacier during the summer of 1999.

above. Both calibrations yield similar slope values, with $a_1 = 0.1510\,\mathrm{mV\,m^{-1}}$ for the pre-installation calibration and $a_1 = 0.1521\,\mathrm{mV\,m^{-1}}$ following retrieval. The post-retrieval calibration line is offset from the pre-installation line by $\Delta V = \Delta a_0 = -18.62\,\mathrm{mV}$. For an average slope value of $a_1 = 0.1515\,\mathrm{mV\,m^{-1}}$ for PR1, this offset would result in an indicated pressure change of -122.9 m. This change is similar to the net offset of -127.3 m obtained by simply summing the two large pressure jumps indicated in the record for PR1 (Fig. 2.11a). The record for PR1 suggests that an individual transducer can be damaged numerous times by successive pressure pulses, and that the damage is cumulative.

2.3.3 Pressure pulse generation

While the weak responses recorded by other instruments fail to reveal the origin of the pressure pulses, they do provide constraints on possible sources. Because no pressure pulse was captured in the records, the duration of the pulse must be shorter than the 2 min sampling interval of the data loggers. The lack of response from conductivity and turbidity sensors precludes any significant change in the flow regime of subglacial water, and it is thus unlikely that the release of stored water gave rise to the pressure pulses. Additionally, the large pulse magnitudes would likely require a significant volume of water to be released, suggesting that elevated pressures would be recorded for several sampling intervals. Mechanical sensors give little indication of basal motion in the instrumented region at the time of the event. Although three geophones recorded counts during the event interval, it is unclear if these counts signify local basal motion or if the geophones are simply responding to the pressure pulse. No change in sliding or deformation rates is evident in slidometer or tilt cell records. Ploughmeters records, including those for instruments installed in-hole with pressure transducers C1, C2 and U1, do not exhibit any change in measured forcing at the time of the event. The small transient responses measured by PL1 and PL2 (Fig. 2.4d, e) lag the event time by 4 min and thus cannot be associated with the generation of the pressure pulses.

Hydraulic transients have been cited as a source of low-frequency seismic waves recorded by earthquake seismographs (St. Lawrence and Qamar, 1979). These transients are caused by abrupt changes in water velocity in subglacial conduits and are analogous to the "water-hammer effect" commonly associated with piping systems. Although this mechanism can generate pressure pulses having sufficiently large magnitude and short duration to reproduce the observed instrument responses, it requires the high water velocities typically associated with conduit drainage. No evidence for conduit drainage has

been found at Trapridge Glacier; water transport is instead thought to be dominated by flow along a permeable horizon of sediments at the ice-bed interface (Stone, 1993). Inferred flow rates of approximately 0.01–$0.1\,\mathrm{m\,s^{-1}}$ (Stone and Clarke, 1996) are too low to produce pressure transients capable of damaging the transducers.

I propose that extreme pressure pulses can be generated by abrupt basal motion that either compresses the subglacial drainage system, producing positive pulses and corresponding positive offsets in transducer records, or dilates it, creating negative pulses and offsets. Because no response was recorded by mechanical instruments at the time of the event, it is likely that that the pulses were either (i) produced locally by some mechanism that did not affect the instruments, such as failure of basal sediments at some depth greater than the instrument installation depths, or (ii) generated remotely and transmitted through the subglacial drainage system. Such transmission seems plausible given the large-scale hydraulic communication evident in the records for connected transducers (Fig. 2.4a), but the effective range of transmission would be limited by diffusion of the pressure pulse. The transmission of pressure pulses does not require significant movement of basal water, and thus little response would be expected in conductivity and turbidity records. It is unclear to what degree the hydraulic system must be compressed in order to generate pressure pulses of magnitudes suggested by the laboratory studies, but the low compressibility of water ($\beta = 5.1 \times 10^{-10}\,\mathrm{Pa^{-1}}$) indicates that even a small volume change would result in a large pressure increase. It would be interesting to develop a quantitative model (perhaps of the form of the model developed in Chapter 4) to investigate possible pulse-generating mechanisms.

If the pulses are produced by some undetected local mechanism, the wide range of offsets recorded during the event (ranging between -75.4 and $+55.2\,\mathrm{m}$ of pressure head) suggest that a large number of individual pressure pulses, each acting over a small basal region, could have been generated by localized compression (producing positive pulses)

or dilation (producing negative pulses) of the basal sediments. A single large, remotely-generated pulse could also produce a wide range of offset values if spatial variations in the hydraulic system acted to modulate the pulse magnitude. In this case, the negative offsets observed in the records for U1 and U2 suggest that an extreme pressure pulse in the drainage system could result in rapid "jacking" of the glacier, creating a strong negative pressure transient in the unconnected regions.

Although pressure pulses with large positive magnitudes are easily imagined, it is less clear how large negative pressures can be supported by a body of water. Cavitation, or the formation of cavities in a fluid when the pressure is reduced and maintained for a sufficient duration below a certain critical value, is a well-known phenomenon that affects both the efficiency and longevity of boat propellers and water pumps. Cavitation is often thought to occur when the local pressure drops below the vapor pressure, but the process is more complex. The vapor pressure at a given temperature is defined as the equilibrium pressure of the liquid's vapor which is in contact with an existing free surface (Knapp and others, 1970). If a cavity is to be formed in a homogeneous liquid, however, the liquid itself must be ruptured. For rupture to occur, the applied stress has to exceed the tensile strength of the liquid, which is determined by intermolecular cohesive forces (Knapp and others, 1970). Laboratory estimates of the tensile strength of pure water range between 34 atm (Meyer, 1911) and ~270 atm (Briggs, 1953). While the tensile strength of a liquid is greatly reduced by the presence of undissolved gas bubbles (Reynolds (1882) and Temperley and Chambers (1946) measured tensile strengths of just ~5 atm for ordinary tap water), dissolved gases do not appreciably reduce the tensile strength (Kuper and Trevena, 1952). It is possible that the subglacial conditions of high hydrostatic pressures and low temperatures encourage rapid dissolution of air bubbles into the water, resulting in basal waters that have sufficiently-high tensile strengths to allow damaging negative pressure pulses.

The records of G1 and G2 (Fig. 2.4e, f) show peak count rates at 2–14 min after the event time, and elevated count rates are measured for as long as 46 min following the event. Two ploughmeters demonstrate increased forcing 4 min after the abrupt changes in the transducer records. If the observed transient increases can be attributed to basal motion, the records suggest that the pressure transients are able to locally decouple the glacier from its bed and thereby induce basal motion.

2.4 Conclusions

I have identified a mode of pressure transducer failure that clarifies the interpretation of records that otherwise challenge understanding. Laboratory studies suggest that pulse magnitudes ranging from ∼900 m to greater than 1500 m could produce the pressure offsets noted in transducer records from Trapridge Glacier. If pulses are generated remotely and transmitted through the subglacial drainage system, subsequent basal motion suggested by ploughmeter and geophone records raises the intriguing possibility that the drainage system can provide a mechanical teleconnection between regions of the bed that are weakly coupled by longitudinal stresses.

Our laboratory study was performed using two transducers of identical manufacture and would be of limited value if other sensors did not fail in a similar manner. Discussions with product engineers at several transducer manufacturers (including Barksdale, Inc., Gems Sensors, Geokon, Inc. and Omega Engineering, Inc.) indicate that pressure transducers that utilize a measurement diaphragm are generally susceptible to similar damage from overpressurization, regardless of the method of diaphragm displacement measurement (e.g., via strain gauges, vibrating wire, or solid state detection). In general, transducer damage can be expected at pressures greater than approximately double

the maximum rated pressure, and results in an linear shift in measured pressure. Several manufacturers commented that the use of a pulse dampener (not used at Trapridge Glacier) may prevent damage to transducers if subglacial pressure pulses are of sufficiently short duration ($\sim$ms). While the use of a dampener could protect the transducers against damage, it would also obscure the occurrence of the events.

Although our laboratory study has reproduced all salient features related to positive jumps in the field records, the testing apparatus used to generate negative damage pressures relies on a vacuum pump and is incapable of producing relative pressures less than $-101\,$kPa (i.e. $\sim$0 atm absolute pressure). This magnitude of negative pressure is insufficient to cause calibration shift. Studies of the tensile strength of water indicate that high-magnitude negative pressure pulses provide a plausible explanation of the negative offsets observed in transducer records. The large negative offset obtained in the post-retrieval recalibration of sensor PR1 lend further support for the occurrence of large negative subglacial pressure pulses. As a final note, it is chastening to consider the fact that, examined separately, the pressure records for sensors C2, C3 and U1 would not have been identified as compromised by sensor failure.

Chapter 3

Abrupt glacier motion and reorganization of basal shear stress following the establishment of a connected drainage system

3.1 Introduction

Glacier motion is controlled to a great extent by the contact between ice and the underlying bed. If the bed is composed of saturated sediments, both sliding and sediment deformation can contribute to the total glacier motion. These two process are strongly influenced by subglacial hydraulic conditions, as high subglacial pressures act both to decouple ice from the bed and to weaken the basal sediments.

At the beginning of the melt season, the subglacial drainage system is likely to be poorly developed and of low capacity. Rapid melting of the winter snowpack can introduce a substantial volume of meltwater into the drainage system and if meltwater input exceeds the drainage system capacity, hydraulic and mechanical instability can result. Instabilities caused by early-summer melting, often called "spring events" (Röthlisberger and Lang, 1987) have been widely observed and result in reorganization of the subglacial drainage system (e.g. Gordon and others, 1998; Stone and Clarke, 1996) or enhanced glacier motion (e.g. Iken, 1983; Harbor and others, 1997).

I present an analysis of instrument records taken during early summer 1995 at Trapridge Glacier. These records reveal that a series of subglacial hydromechanical events occurred following the establishment of a subglacial drainage system in the area. Pressure fluctuations in the drainage system weakened a region of the bed that was acting as a local

pinning point and resulted in three episodes of strong basal motion on 11 June (day 162).

3.2 Observations
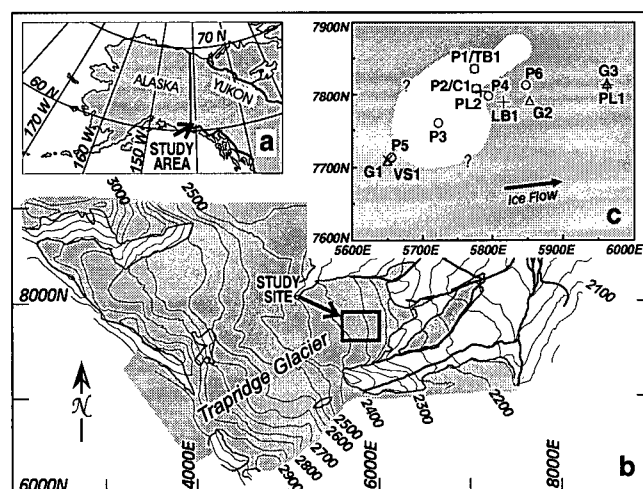
Figure 3.1: Study area. (a) Location map, southwestern Yukon Territory, Canada. (b) Trapridge Glacier, showing location of instrument study. (c) Study site. Unshaded area indicates region of high connectivity; question marks denote poorly constrained boundaries.

Year-round measurements of subglacial conditions have been recorded at Trapridge Glacier, Yukon Territory, Canada (Fig. 3.1a,b) since 1988. One focus of these studies is to clarify the role that the subglacial water system plays in facilitating basal sliding and bed deformation (e.g. Blake, 1992; Blake and others, 1992; Blake and others, 1994; Fischer and Clarke, 1997b, Fischer and Clarke, in review). Fifty-six hydrological and mechanical instruments were in operation on 11 June (day 162) 1995, including pressure transducers, conductivity and turbidity sensors, ploughmeters, load bolt sensors, geophones and vertical strain sensors. Responses are seen in the records of 42 of these sensors at the time of the events. In order to clarify discussion I present the records for 16 instruments, that were installed between July 1992 and July 1994. These records represent the range

of mechanical and hydrological responses observed during day 162. Corrected sensor positions, as calculated from surface flow measurements, are shown in Figure 3.1c.
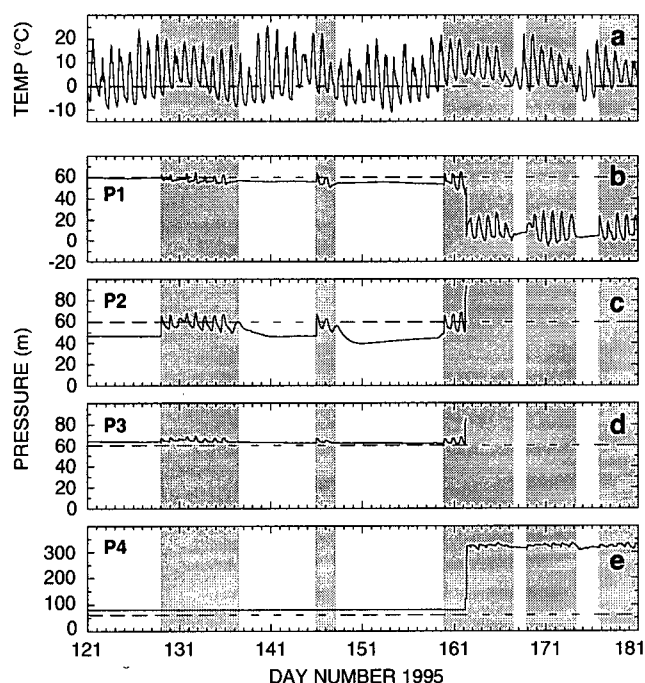
Figure 3.2: Air temperature and subglacial water pressure records. Day 121 corresponds to 1 May 1995. Shaded regions indicate periods exhibiting diurnal pressure fluctuations. (a) Air temperature record. (b) Water pressure record for P1. Dashed horizontal line represents local flotation pressure. (c) Water pressure record for P2. (d) Water pressure record for P3. (e) Water pressure record for P4 (note change of scale).

An air temperature record for Trapridge Glacier during the period 1 May–30 June (day numbers 121–182) 1995 is presented in Figure 3.2a. The record shows strong diurnal variations, with measured temperatures ranging from $-11\,C°$ to $+26\,C°$. True daytime temperatures are likely lower than indicated, however, as direct solar heating of the logger enclosures can yield artificially high temperatures. In addition to diurnal variations, temperature fluctuations with timescales of approximately 10–20 days are also apparent

in the record. Minimum night-time temperatures remain above 0°C during days 131–133, 145, 160–167, 170–173 and 179.

Pressure transducer P1 (Fig. 3.2b) was installed during July 1994 in a borehole that connected at the time of drilling. The pressure record during days 121–159 alternates between two distinct modes: periods of high, steady pressures, with values close to the ∼60 m local flotation pressure head; and periods of high diurnal variability, which exhibit peak pressures greater than flotation and minimum night-time pressures with values lower than those recorded during high, stable periods. Inspection of Figure 3.2 reveals a strong relationship between pressure modes and night-time temperatures, with periods of diurnal pressure variability occurring in conjunction with above-freezing night-time temperatures: diurnal pressure fluctuations are recorded during days 129–137, 146–148, 160–167, 169–174 and 177–182 (shaded regions, Fig. 3.2); above-freezing night-time temperatures are noted for days 131–133, 145, 160–167, 170–173 and 179–182. The third period of diurnal pressure variability begins with an abrupt 9.1 m jump in hydraulic head at 2300 h on day 159. A 41.6 m pressure drop is recorded at 0820 h on day 162. Diurnal pressure variations continue uninterrupted following the pressure drop, and negative pressure minima are indicated during days 164, 167, 170–172 and 178–179.

Transducers P2 and P3 (Fig. 3.2c, d) were installed in connected boreholes during July 1994. Both records alternate between winter- and summer-mode behaviours similar to those in the record for P1. Winter-mode pressures for P2 measure approximately 80% of the flotation value, while those for P3 register slightly greater than flotation. The timing of diurnal variations in both records closely matches those for P1 (shaded regions, Fig. 3.2), and similar peak pressure values are indicated in all three transducer records during diurnal fluctuations. Both P2 and P3 fail at 0820 h on day 162, coincident with the 41.6 m pressure drop in the record for P1.

Transducer P4 (Fig. 3.2e) was installed in July 1993 in a borehole that connected at

the time of drilling. Steady pressures are indicated for the first 39 record days, with values

of approximately 135% of the local flotation value. Diurnal pressure fluctuations, out-

of-phase with those with in the records for P1–P3 and with amplitudes of ∼0.8 m, begin

on day 160. Pressure jumps of 41.1 m and 201.8 m are recorded at 0500 h and 0820 h,

respectively, on day 162. Indicated pressures following these jumps measure greater than

5 times the local flotation pressure.
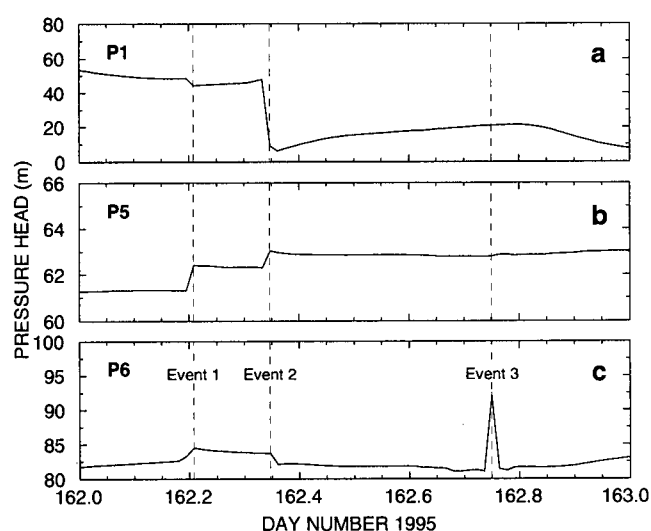
Figure 3.3: Detailed pressure records. Day 162 corresponds to 11 June 1995.
(a) Transducer P1. (b) Transducer P5. (c) Transducer P6.

Figure 3.3 details the pressure record for three sensors on day 162. Sensor P1 (Fig.

3.3a) registers a decrease of 4.3 m at 0500 h, immediately following the beginning of the

diurnal pressure rise. This decrease is followed by a 41.6 m drop at 0820 h seen in Figure

3.2b. The character of the diurnal cycle is unchanged by these pressure changes. Figure

3.3b shows the pressure record for transducer P5, which was installed in an unconnected

borehole in July 1993. Small pressure jumps of 1.1 m and 0.7 m coincide with the drops

recorded by P1 at 0500 and 0820 h. The record for transducer P6 (Fig. 3.3c), installed

in July 1992 in an unconnected borehole, also shows pressure changes at these times: an increase of 1.9 m at 0500 h is followed by a decrease of 1.6 m at 0820 h. In addition, a transient pressure increase of 10.9 m is recorded at 1820 h. Many instrument records exhibit responses within one 20 min sampling interval of these times, suggesting the occurrence of a series of subglacial events during day 162. Hereafter, I designate the events at 0500 h, 0820 h and 1820 h respectively, as events 1, 2 and 3.

Clock drift during the winter months can result in discrepancies as large as 6 min between loggers, and instrument responses to events that occur within this measurement window will be distributed over two sampling intervals. Several instrument records demonstrate responses to events 2 and 3 that lag the event timing by one sampling interval. Although it is possible that these lags reflect a series of strong mechanical adjustments around the time of the events, they are equally attributable to clock drift. The lags do not appear to be correlated to instrument location, suggesting that the large mechanical forcings recorded during the events affected the entire study area simultaneously.
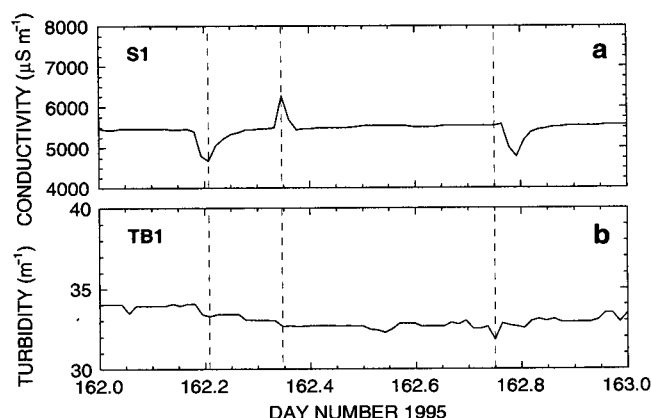
Figure 3.4: Hydrology sensor records. Dashed vertical lines at 0500 h, 0820 h and 1820 h represent events 1–3. (a) Conductivity sensor S1. (b) Turbidity sensor TB1.

Figure 3.4 illustrates typical event responses for conductivity and turbidity sensors (Stone and others, 1993) during day 162. Dashed vertical lines represent the timing of events 1, 2 and 3. Sensor S1 (Fig. 3.4a) was installed in the same borehole as transducer P2 (Fig. 3.2c). Negative transient responses were recorded both at event 1 and immediately following the timing of event 3, with a positive transient noted at event 2. Responses to the three events are of comparable magnitude ($\sim$800 μS/m), and a background conductivity value of 5400 μS/m is re-established within 180 min of each event. Figure 3.4b shows the record for turbidity sensor TB1, which was installed in the same borehole as sensor P1 (Fig. 3.2b, 3.3a). Very small responses are recorded during the events, with a 0.8% drop at event 1 and a transient change of -0.9% at event 3 superimposed onto the slight ($\sim$2%) diurnal signal.
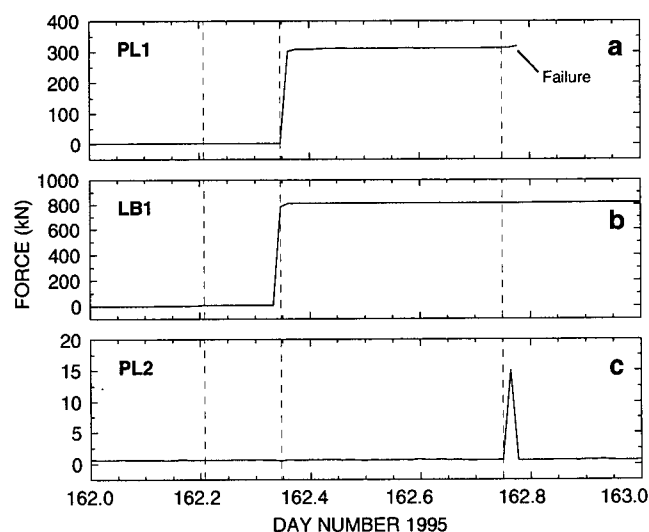
Figure 3.5: Mechanical sensor records. Dashed vertical lines at 0500 h, 0820 h and 1820 h represent events 1–3. (a) Ploughmeter PL1. (b) Load bolt sensor LB1. (c) Ploughmeter PL2.

Records during day 162 for three instruments that measure mechanical forcings in the glacier bed are shown in Figure 3.5. Ploughmeter (Fischer and Clarke, 1994) PL1 (Fig.

3.5a) was installed in July 1992. While no response is evident at event 1, a large jump was recorded at event 2, during which forcing increases from 1.9 kN to 310 kN. High, steady values are measured until sensor failure occurs immediately following event 3. Load bolt (Iverson and others, 1994) LB1 (Fig. 3.5b) was installed in July 1993. The force acting on the instrument increases from 2.3 kN to 9.0 kN at event 1, and then jumps to 813 kN at event 2. This high value is measured for the remainder of the record, and no further response is seen at event 3. The record for ploughmeter PL2 (Fig. 3.5c), installed July 1994, shows a steady force value of ~0.6 kN through most of day 162. No response is evident at events 1 or 2, but a transient increase of 15.1 kN is seen immediately following event 3.
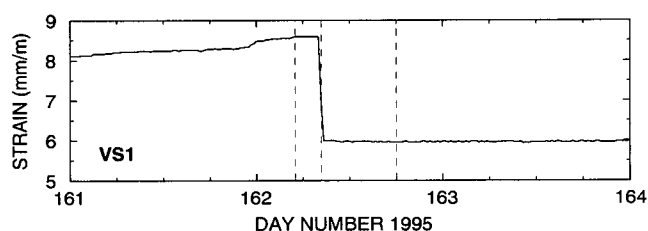
Figure 3.6: Vertical strain record during days 161–164 (10–12) June 1995. Dashed vertical lines at 0500 h, 0820 h and 1820 h during day 162 represent events 1–3.

Figure 3.6 shows the record during days 161–164 for vertical strain sensor (Harrison and others, 1993) VS1, which was installed during July 1992. Vertical strain values increase steadily through the first portion of the record, with maximum vertical extension of the ice occurring immediately prior to event 1. The strain value remains constant between events 1 and 2. A drop of ~2.64 mm/m in vertical strain occurs at event 2, with no further response seen at event 3. Vertical strain values remain constant for 8.5 days before values begin increasing again.

Records for three geophones during day 162 are shown in Figure 3.7. Plotted are the
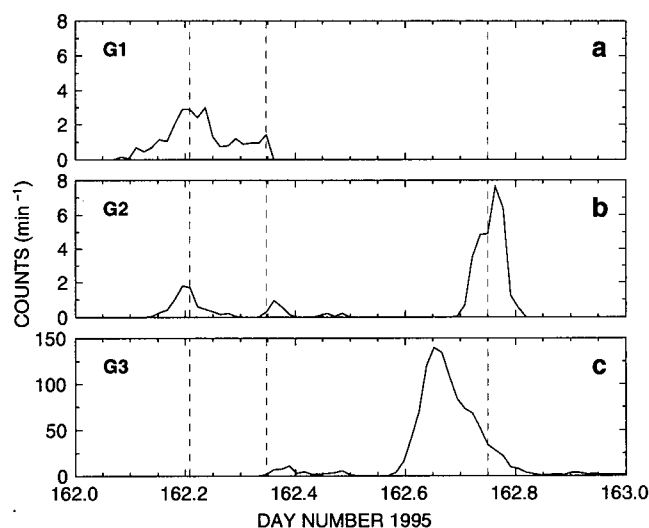
Figure 3.7: .
Geophone records during 11 June 1995. Dashed vertical lines at 0500 h,
0820 h and 1820 h represent events 1–3.

number of "ice quake" counts per minute; the timing and magnitude of individual events
are not recorded. All three geophones were installed in July 1992. A generally down-
glacier progression of high count rates is apparent in the records, with counts spanning
a several-hour period at each event. The geophone records exhibit elevated count rates
during a several-hour period spanning each event. Geophone G1 (Fig. 3.7a), located
approximately 0.9 m from VS1, is furthest up-glacier of the three geophones. Its record
shows counts as early as 3.3 h before event 1. A broad peak of 2.9 min^{-1} occurs at the
time of the event. Count rates between events 1 and 2 average 0.9 min^{-1}, increasing to
1.4 min^{-1} during event 2. Following event 2, no further counts are noted for the remainder
of the day. The record for geophone G2 (Fig. 3.7b), located in the middle of the study
area, shows peak rates of 1.8 min^{-1} immediately prior to event 1 and 1.0 min^{-1} during
event 2. Elevated count rates are measured during a 2.67 hr period spanning event 3,
with a peak of 7.7 min^{-1} immediately following the time of the event. Geophone G3 (Fig.

3.7c) is located at the lower end of the study area. No counts are evident until event 2; a peak count rate of $10.8\,\mathrm{min^{-1}}$ observed 1 h later. Extremely high count rates are recorded during a 7 h period spanning event 3: a peak rate of $140\,\mathrm{min^{-1}}$ is indicated at 1540 h. The count rate declines to $30\,\mathrm{min^{-1}}$ at event 3.

3.3 Interpretations and discussion

The high, steady pressures seen in the first portion of the record for transducers P1–P3 (Fig. 3.2b–d) are typical of winter pressure records and indicate a low-volume, poorly-connected subglacial hydraulic system (e.g. Stone, 1993). In contrast, the diurnal pressure fluctuations recorded during days 129–137, 146–148, 160–167, 169–174 and 177–182 (shaded regions) are characteristic of well-connected summer-mode drainage systems. Pressure excursions during these periods are driven by variations in the flux of meltwater reaching the glacier bed as daily meltwater production peaks and ebbs. The records for P1–P3 indicate repeated establishment and shut-down of a connected drainage system. This winter–summer mode switching is found in the records for 8 pressure transducers, indicating connections over the up-glacier portion of the instrumented region during these periods. A $\sim20\,000\,\mathrm{m^2}$ region of high hydraulic connectivity indicated by these records is shown in Figure 3.1c (unshaded area). The extent of this region is poorly known due to limited instrument distribution; questionable boundaries are indicated by question marks.

Periods of hydraulic connection in the records for P1–P3 (Fig. 3.2a–c) coincide with warm night-time temperatures, suggesting rapid, sustained melting of the winter snow-pack during these times. Such vigorous early-season melting can place a substantial volume of water into the subglacial drainage system, which is likely to be poorly developed at the beginning of summer. If the input of meltwater exceeds the capacity of the

drainage system to remove it, hydraulic and mechanical instability can result (e.g. Stone, 1993; Jansson, 1995; Stone and Clarke, 1996).

The instrument records presented in Figures 3.2–3.7 show evidence for both hydraulic and mechanical responses during three subglacial events on day 162. These events occur soon after hydraulic connection is re-established in the region, suggesting that changes in drainage system morphology altered mechanical properties of the bed. In the following sections I present an interpretation of the hydrological and mechanical responses recorded during the events.

3.3.1 Hydrological response

The record for transducer P1 (Fig. 3.2b) shows pressure drops of 4.3 m and 41.6 m at events 1 and 2. Although abrupt pressure adjustments are plausible responses to changes in the subglacial drainage system, features in the record indicate that these drops are due to transducer damage rather than morphological switching. Studies by Kavanaugh and Clarke (2000) presented in the previous chapter show that extreme pressure pulses can damage the measurement mechanism of pressure transducers. This damage, attributed to compression or dilation of the subglacial drainage system by abrupt ice motion, produces a calibration shift that appears in field records as a sudden pressure jump that is difficult to distinguish from a true pressure change. Sufficiently large pressure pulses result in transducer failure. Evidence for abrupt glacier motion is seen in ploughmeter and load bolt records and will be discussed in the following section.

A transient pressure pulse at the time of event 3 is noted in the record for P6 (Fig. 3.3c). Although the indicated pulse magnitude is too small to cause sensor damage, it is not certain whether this measurement occurred at the time of peak pulse pressure. If the maximum measured pressure record does represent the true local value of the peak, spatial variations in the hydraulic system seem to locally modulate the pulse magnitude,

and thus higher pressures could have occurred in other areas. Similar pressure transients are seen in the records for several other transducers at the time of the events.

Records for 14 transducers exhibit step pressure changes at the time of events 1 and 2. These changes range between a drop of 41.6 m in the record for transducer P1 (Fig. 3.2b) and an increase of 201.6 m in the record for transducer P4 (Fig. 3.2e). Following this largest increase, recorded pressures consistently measure greater than 5 times overburden, a value too high to be maintained subglacially. Likewise, negative pressures in the record for P1 during days 164, 167, 170–172 and 178–179 cannot be attributed to errors in calibration or installation and are thus indicative of transducer malfunction. In addition to the abrupt pressure changes observed in many transducer records, seven pressure transducers failed during events 1 and 2, including sensors P2 and P3 (Fig. 3.2c, 2d). These records further indicate the occurrence of damaging pressure pulses during the events.

While extremely large pulses can cause total pressure transducer failure, other instruments are insensitive to pressure pulses. Extreme events can thus destroy pressure transducers without adversely affecting other instruments, including those installed in the same borehole. Pressure transducer P2 (Fig. 3.2c), which fails at event 2, was installed in the same borehole with S1 (Fig. 3.4a); the conductivity sensor is undamaged by the event. In total, seven pressure transducers failed during the events, but none of the instruments installed in common holes failed at these times. This selective device failure argues against several common failure mechanisms, including wire breakage and crushing of the transducer (Kavanaugh and Clarke, in press), and gives further evidence for large pressure pulses at the time of the events.

Although many of the large jumps can be clearly attributed to sensor damage, the interpretation of smaller jumps can be more difficult. The record for P5 (Fig. 3.3b) shows increases of 1.1 m and 0.7 m at events 1 and 2; the record for P6 (Fig. 3.3c)

exhibits a 1.9 m jump at event 1, followed by a drop of 1.6 m at event 2. Both of these instruments are located outside the region of high connectivity shown in Figure 3.1 and exhibit unconnected behaviour during this period. Although these jumps are most likely caused by sensor damage, it is also possible that they reflect actual, if minor, adjustments in water pressure at the location of the instrument. These small, isolated pressure adjustments could result from basal motion and do not reflect significant changes in drainage system morphology.
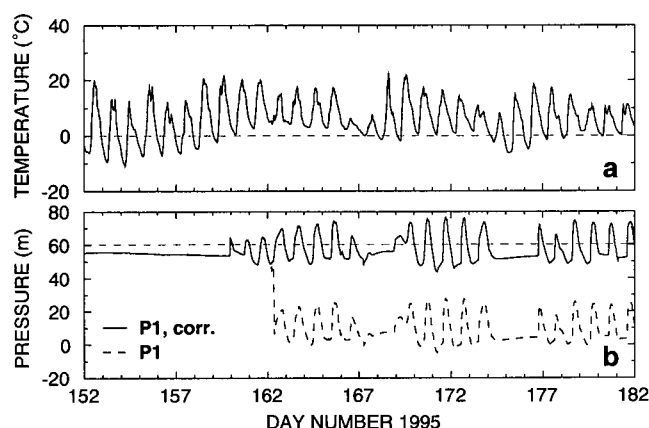
Figure 3.8: Air temperature and corrected subglacial water pressure records. Day 152 corresponds to 1 June 1995. (a) Air temperature record. (b) Corrected pressure record for P1. Uncorrected record (dashed) is shown for comparison. Horizontal dashed line represents the local flotation pressure.

Figure 3.8b shows the record for P1 during days 152–182 with the pressure drops at 0500 h and 0820 h on day 162 removed (solid line; the original record is represented by the dashed line). The temperature record during the same period is shown in Figure 3.8a. It is likely that changes in the subglacial drainage system sufficient to precipitate a 41.6 m drop would also lead to changes in the response of the system to pressure variations. The corrected record instead exhibits consistent behaviour both before and after the indicated drops, and it is difficult to determine event timing without consulting the uncorrected

record. These features strongly suggest attribution of the pressure drops to damaging pressure pulses of the kind proposed in the previous chapter. The corrected record shows diurnal variations with pressures greater than the local flotation value and night-time minima of 44–50 m. Days 168 and 174–176, during which diurnal variations are absent, exhibit pressures similar to the steady winter-mode pressures measured prior to day 159. After correction, pre- and post-event pressure signal characteristics are consistent during both winter and summer modes.

Minimum night-time pressures measured during times of diurnal variability exhibit values that are lower than the pressures recorded during stable winter-mode periods (Fig. 3.8b). This behaviour demonstrates the higher transport capacity of connected drainage systems, which allow greater evacuation of basal water and thus lower night-time pressures. It is also apparent from the records that the connected system actively adjusts to variations in meltwater input, as high daytime temperatures generally correspond to low night-time pressures. This relation is most clearly evident during days 170–177 (Fig. 8a–b). The decreasing daytime temperatures seen in days 170–174 are accompanied by increasing minimum night-time pressures. Diurnal variations cease as night-time temperatures dip below freezing on day 174. Decreasing meltwater input during this period leads to closure of the connected system, resulting in decreased drainage capacity and higher night-time pressure minima. The system switches to an isolated winter-mode state when the meltwater flux drops below some threshold. Hydraulic connection is re-established on day 176 with the return of higher temperatures and increased meltwater input.

Inspection of Figures 3.8a and 3.8b shows that minimum night-time pressure values are more closely related to peak daytime temperatures than to peak pressures. This is not surprising, because increased drainage capacity during periods of high meltwater flux would result in the depression of both daytime and night-time pressures. It is

not clear how the drainage system capacity changes in response to meltwater input. While adjustments occur rapidly enough to accommodate changes in daily meltwater input, variations in minimum night-time pressures show that the adjustments are not immediately reversible. One plausible mechanism is the incorporation of additional basal area into the drainage system during periods of high meltwater input. This process could be facilitated by hydraulic jacking (ice–bed separation promoted by high water pressures), which would allow rapid flooding of the drainage system margins. Evidence for hydraulic jacking is seen in the records for several pressure transducers located on the periphery of the well-connected region (Fig. 3.1c). These records exhibit low-amplitude diurnal fluctuations that are out-of-phase with those of P1, indicating the transfer of mechanical support of ice overburden from the unconnected region as water pressure varies in the connected system (Murray and Clarke, 1995; Gordon and others, 1998). Flooding of the margins would increase the hydraulic transmissivity there and permit greater meltwater transport. Subsequent reductions in meltwater flux would allow the margins to lose hydraulic connection with the drainage system, resulting in decreased transport capacity and higher night-time pressure minima.

In contrast with the large pressure signals recorded during the events, records for turbidity and conductivity sensors (Fig. 3.4) show only minor responses. The record for S1 exhibits transient responses at all three events, returning to a stable background value following each event. Oldenborger and others (in review) have proposed that such conductivity fluctuations can result from ice- or bed-deformation events that drive water exchange between the borehole and subglacial bed, which disturbs a stratified conductivity structure within the borehole. Assuming that conductivity decreases with increasing distance from the bed, fluctuations could result from water being forced into the underlying sediments (resulting in the lower conductivity values associated with events 1 and 3) or expelled from the sediments (resulting in the increases conductivity seen at event 2)

during motion associated with the events. Following these disturbances, the equilibrium conductivity structure is rapidly re-established. The interpretation of Oldenborger and others (submitted) is based on observations of hydraulically-unconnected boreholes, in which mixing of the water is likely negligible. The borehole containing sensors S1 and P2 is inferred to be in a hydraulically-connected region of the bed, and therefore the water contained within the borehole is likely to experience some flow-driven mixing. If this mixing is incomplete, a response similar to that postulated for unconnected boreholes is plausible given a large enough disturbance. The responses in the record for TB1 (Fig. 3.4b) at events 1 and 3 are too small to suggest lasting changes in drainage patterns and give little evidence for movement of substantial volumes of basal water during any of the events.

Aside from small transient responses, records for conductivity and turbidity sensors show no significant response to the events of day 162. Similarly, after removal of the large damage-induced jumps in the records of P1 and other pressure transducers, little indication of lasting change is present in the pressure records. Hydraulic responses during the events thus appear to have been largely transient, with little evidence for morphological changes in the subglacial drainage system.

3.3.2 Mechanical response

Despite the strong responses apparent in the records of PL1, LB1 and PL2 (Fig. 3.5a–c), it is unclear how these sensors should be expected to respond to episodes of strong, sudden basal motion. Ploughmeters have been used as sliding indicators in clast-rich tills (Fischer and Clarke, 1997a), and a transient response to glacier motion would be expected if till exhibits viscous or elastic properties. Recent studies by Iverson and others (1998) and Tulaczyk and others (2000a) suggest that till behaviour is best approximated as Coulomb-plastic. The strength of such a material is independent of the strain rate

and is linearly related to the effective pressure p' (the difference between ice overburden pressure and pore-water pressure) by $\sigma_Y = c_0 + p' \tan\phi$, where c_0 is the cohesion and ϕ the angle of internal friction. The force acting on a ploughmeter or load bolt being dragged through such a material would reflect only variations in the yield strength of the material and would not be affected by changes in basal velocity. Ploughmeter force records are commonly found to be inversely correlated to local subglacial water pressure (e.g. Fischer and Clarke, 1994; Hooke and others, 1997) and typically show no correlation with changes in sliding velocity indicated by nearby slidometers. These behaviours suggest that subglacial till behaves as a Coulomb-plastic material. Conversely, ploughmeter records occasionally show transient force increases that coincide with elevated geophone count rates, suggesting that the ploughmeters are responding to episodic basal motion.

Tills are known to exhibit dilatancy, or expansion under shear, if they are in an overconsolidated state (e.g. Boulton and others, 1974; Clarke, 1987b). Diurnal pressure variations are likely to produce overconsolidation in tills that have not been significantly sheared for a time (Iverson and others, 1998). Disturbance of till by ploughmeter or load bolt motion can produce dilatant expansion, resulting in a drop in pore-water pressure. This pressure drop in turn strengthens the till. Such strengthening is called "dilatancy hardening" and has been noted in laboratory studies (e.g. Iverson and others, 1998). In general, basal motion occurs slowly enough that the pore-water pressure in the disturbed sediments has time to equilibrate with the surrounding pressures. Rapid instrument motion, however, can create dilatancy rates that are large relative to pore-water flow and hence produce appreciable dilatancy strengthening of the till immediately surrounding the instrument. The transient response recorded by PL2 at event 3 is of short duration, indicating rapid equalization of pore-water pressures with the surrounding values. Calculations show that hydraulic diffusivities greater than 10^{-6}–$10^{-4}\,\mathrm{m^2 s^{-1}}$ are required to explain the rapid decay of dilatancy strengthening seen in the instrument records.

These values are in reasonable agreement with values obtained in laboratory studies (e.g. Iverson and others, 1997) and field studies at Trapridge Glacier (e.g. Stone and Clarke, 1993; Fischer and others, 1998).

In contrast with the transient response of PL2, the force records for PL1 and LB1 exhibit step increases at the time of the events (Fig. 3.5a–c). The indicated forcings of 310 kN and 813 kN are more than an order of magnitude greater than typical peak forcings recorded at Trapridge Glacier. The high, sustained forcings in these records suggest that permanent damage was sustained by PL1 and LB1 during the events. Strong basal motion, coupled with sufficient dilatancy hardening, could have permanently bent the steel rod in ploughmeter PL1 during event 2. This bend would produce an apparent offset in measured force analogous to the jumps seen in pressure transducer records. Further damage sustained during event 3 results in device failure. The record for LB1 can be explained by similar damage to the device. In the spirit of the investigations presented in Chapter 2, it would be interesting to conduct laboratory studies to investigate this mode of ploughmeter and load bolt failure. Such studies could provide estimates on the degree of dilatancy hardening required to explain the records for PL1 and LB1 and would therefore allow us to judge whether this mechanism is qualitatively reasonable. At the time of this writing, these studies have not been performed.

Increasing strain values prior to event 1 in the record for VS1 (Fig. 3.6) indicate longitudinal compression in the vicinity of the sensor. The constant strain value recorded between events 1 and 2 suggest that no further compression occurred during this period. The large drop at event 2 indicates a decrease in vertical strain equal to the net extension of the previous 288 days, suggesting substantial longitudinal extension at the time of event 2. The record for VS1 is thus consistent with the evidence for strong basal motion seen in ploughmeter and load bolt records.

Geophones respond to a variety of sources such as ice fracture and basal slippage.

Geophone records can therefore yield information about stress transients in the glacier, as these sources typically involve some failure mechanism and are thus focussed where rapid changes in the stress field occur. The down-glacier progression of high count rates in the geophone records indicates the migration of a region of high stress over the course of the events. The high-stress region likely represents a local "sticky spot", or area in which the basal shear stress is concentrated (Alley, 1993). Migration of this sticky spot will be discussed in the following section.

3.3.3 Glacier response

Because sediment strength is strongly dependent on pore water pressure, diurnal pressure fluctuations within the subglacial drainage system result in variations in sediment strength over large portions of the bed. Furthermore, high drainage system pressures can weaken coupling at the ice–bed interface, allowing basal sliding. Through these processes, diurnal pressure fluctuations can drive a cyclic transfer of shear stress between connected and unconnected regions of the bed. The establishment of a subglacial drainage system can thus significantly change both the mechanical properties of the bed and the distribution of shear stresses acting upon it.

Pressure records show that hydraulic connection was re-established over a large region of the bed (Fig. 3.1c, unshaded area) 3 days prior to the events of day 162. Following this connection, large diurnal pressure variations are recorded in the region, with peaks above local flotation (Fig. 3.8b). These strong variations contrast markedly with the steady pressures recorded during the winter months. Development of a connected drainage system could have resulted in significant changes in the distribution of basal shear stress in the region.

Geophone records suggest that these changes led to the failure of a local sticky spot during the events of day 162. Failure of this sticky spot, which played an important

role in balancing driving stresses, destabilized the glacier in the instrumented region and resulted in vigorous basal motion at the time of the events. The down-glacier progression of high geophone count rates further suggests that failure of the sticky spot resulted in the transfer of basal stress to the unconnected region of the bed.

While geophone records suggest significant changes in basal shear stress during the events, they yield no information about the state of stress prior to hydraulic connection. Variations in the distribution of stresses indicated by geophone records thus represent changes relative to some background state. This background stress state is represented by uniform shading in Figure 3.9a; locations for geophones G1–G3 are also shown.

Geophone G1 (Fig. 3.7a) is located slightly up-glacier from the large connected region shown in Figure 3.1c. Following hydraulic connection, basal shear stresses in this location could thus be strongly affected by variations in drainage system pressure. Counts begin 3.3 h prior to event 1 and are measured continuously during a 7 h period spanning events 1 and 2, indicating that mechanical adjustments occurred throughout this period. The record for geophone G2 (Fig. 3.7b), which is located down-glacier from the connected region, also shows elevated count rates during events 1 and 2. In contrast, the record for G3 (Fig. 3.7c), located furthest down-glacier, does not exhibit counts prior to event 2.

These records indicate significant changes in the state of stress in the connected region (Fig. 3.1c) between geophones G1 and G2 during the time spanning the first two events. This period coincides with the minimum night-time pressure in the subglacial drainage system, at which time pressures in the drainage system are well below those measured in unconnected regions of the bed. Because the yield strength of tills is strongly dependent on pore pressure, sediments in connected portions of the bed are subject to stiffening during low drainage system pressures. Such stiffening could create areas where basal shear stresses concentrate, effectively creating a sticky spot. This configuration is inherently unstable, however, as subsequent increases in system pressure would weaken

the sediments and favour failure of the sticky spot. It is not clear from instrument records whether the sticky spot was established in this location prior to hydraulic connection; if so, low night-time system pressures likely focussed additional shear stress onto the sticky spot. Diurnal pressure variations during days 159–161 could have weakened the sticky spot, resulting in failure on day 162.
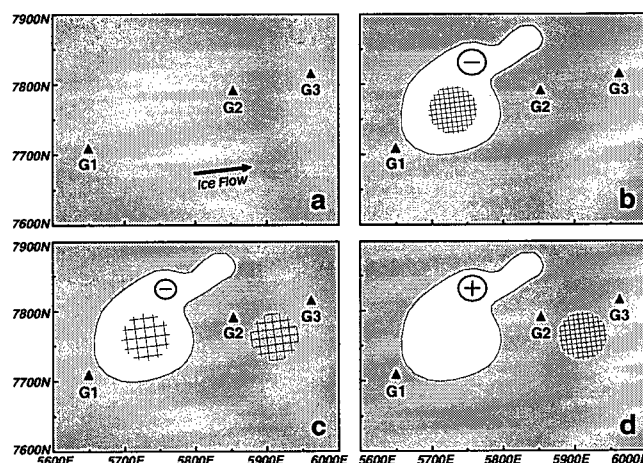
Figure 3.9: Inferred migration of local "sticky spot" during events. Shaded areas represent hydraulically-unconnected regions; unshaded areas represent region of high hydraulic connectivity. Cross-hatched area denotes possible location of sticky spot. (a) Prior to hydraulic connection. Locations for geophones G1–G3 are shown. (b) Possible sticky spot configuration during event 1. Water pressure in connected region is lower than that in the unconnected region at this time. (c) Possible sticky spot configuration during event 2. Water pressure in connected region is slightly lower that that in the unconnected region at this time. (d) Possible sticky spot configuration following event 3. Water pressure in connected region is greater than that in the unconnected region at this time.

Because the effective listening range of a geophone varies with icequake magnitude, it is not possible to determine the proximity of an icequake source relative to the geophone placement. The true location and extent of a nearby sticky spot, therefore, cannot be determined from geophone records. Figure 3.9b illustrates one possible configuration at

the time of event 1; other plausible sticky-spot configurations are certainly possible. The sticky spot, represented by the cross-hatched area, is located within the connected region of the bed (unshaded area). Shading represents hydraulically-unconnected regions of the bed.

Event 1 occurs at 0500 h, immediately following the onset of the diurnal pressure rise of day 162. This indicates a high degree of instability in this region, as only a slight pressure increase is needed to trigger failure of the sticky spot. As outlined above, perturbations associated with basal motion during this failure gave rise to a broad range of instrument responses. Figure 3.10a shows the location of instruments that recorded responses during event 1. Instrument locations have been corrected for glacier flow, though some overlapping symbols have been shifted slightly.

Pressure changes are seen in the records for 15 transducers at this time (Fig. 3.10a). Of these 15 records, 10 show step increases and 1 shows a transient increase. Pressure drops are also evident in several records, with 3 records exhibiting step decreases and 1 showing a transient pressure drop. These widespread pressure changes result from damaging pressure pulses or from minor, local pressure adjustments following glacier motion. Small transient responses noted in the records for conductivity and turbidity sensors indicate brief disturbances associated with glacier motion rather than lasting changes in the subglacial drainage system.

Basal motion during event 1 is indicated in the record for sensor LB1, which exhibits an increase in measured forcing at the time of the event. The record for vertical strain sensor VS1 (Fig. 3.6) shows steadily-increasing values in the first portion of the record, indicating continuous longitudinal compression. This trend stops at event 1, suggesting that basal motion during the event temporarily halted the accumulation of strain in this region of the glacier. No further change is indicated until event 2. Failure of one pressure transducer is also noted at this time (Fig. 3.10a). This transducer was installed
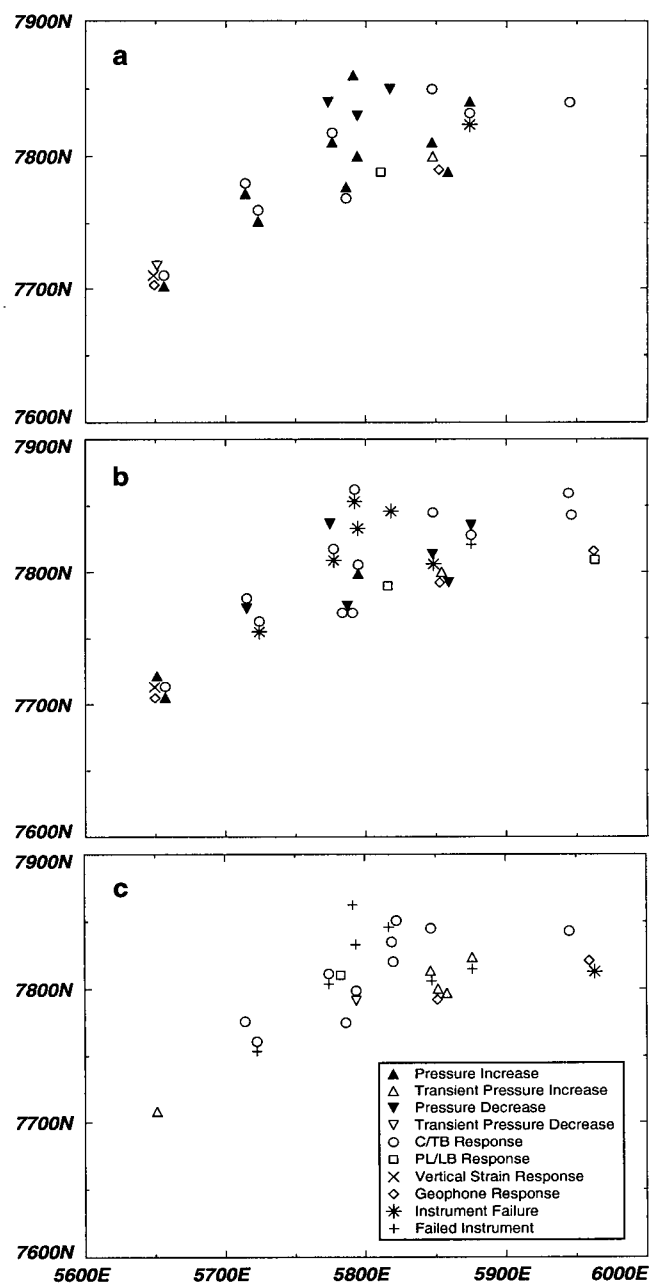
Figure 3.10: Map view of instrument locations. Locations have been corrected for glacier flow, and overlapping symbols have been shifted slightly. (a) Instrument responses during event 1. (b) Instrument responses during event 2. (c) Instrument responses during event 3.

in the basal sediments in order to measure pore water pressure; this placement made it particularly susceptible to damage during glacier motion. Because these events occurred before our arrival at Trapridge Glacier, no survey data exists during the time of the events. Similarly, no slidometer or bed tilt instruments (Blake and others, 1994) were in operation at the end of the winter. It is thus not possible to determine the magnitude of glacier motion during the events.

Event 2 occurs at 0820 h following an increase in drainage system pressures. Although system pressures at the time of the event are lower than those measured in the unconnected region, the increasing pressures likely resulted in the weakening of sediments in the sticky spot, which precipitated a second episode of vigorous basal motion. This motion is evidenced by large force responses in the records for PL1 and LB1 (Fig. 3.5a, b) and by substantial longitudinal extension in the record for VS1 (Fig. 3.6). The period of elevated count rates in the record for G1 (Fig. 3.7a) ends at event 2, and no further counts appear in the record for the remainder of the day. In contrast, counts first appear in the record for G3 (Fig. 3.7c) at this time. These records indicate reorganization of basal shear stresses during the strong basal motion of event 2, during which a portion of the basal traction is transferred from the connected region to the hydraulically-unconnected region near G2 and G3 (Fig. 3.9c).

Pressure records show strong responses during event 2. Step changes are present in the records for 9 transducers (Fig. 3.10b), and one record exhibits a transient increase during the event. In addition, 6 transducers fail at the time of the event. These responses indicate pervasive pressure transducer damage during the event, resulting from extreme pressure pulses generated by the strong basal motion. In general, pressure changes associated with event 2 are of greater magnitude than those recorded during event 1, indicating that pulses were correspondingly larger. This is consistent with evidence for strong basal motion presented in the records for PL1, LB1 and VS1. The transient responses noted

in the records for conductivity and turbidity sensors (Fig. 3.10b) are likely the result of glacier motion and do not represent significant lasting changes in the drainage system.

Extremely high count rates are apparent in the record for G3 (Fig. 3.7c) during a 7 h period spanning event 3. Increasing drainage system pressures are also indicated during this period, with values measuring greater than the local flotation pressure. These increasing pressures cause continual weakening of sediments in the connected region, resulting in the transfer of additional shear stress to the new sticky spot during this period.

Event 3 occurs at 1820 h, 40 min prior to peak diurnal pressure on day 162. Transient responses are noted in the records for 6 pressure transducers at this time (Fig. 3.10c); no step changes are recorded during the event. While the failure of six pressure transducers during event 2 precludes measurement in those locations, the relatively minor responses indicated by surviving pressure transducers suggest that pulse magnitudes during event 3 are lower than those during events 1 and 2. Responses noted in the records for conductivity and turbidity sensors are similar to those recorded during events 1 and 2. Glacier motion during event 3 is indicated by strong responses in records for two ploughmeters. Failure of PL1 (Fig. 3.5a) occurs at this time, and the record for PL2 (Fig. 3.5c) shows a transient force increase during the event.

No evidence for strong basal motion is seen in the instrument records for several weeks following event 3, suggesting that the mechanical adjustments made over the course of the events resulted in a stable configuration of basal stresses. Relocation of the sticky spot to the unconnected region during the events (Fig. 3.9d) likely contributed greatly to the stability in the study area, as sediments there are less susceptible to pressure-induced weakening than are sediments in the connected region.

3.4 Conclusions

Hydraulic conditions beneath alpine glaciers can vary on both seasonal and diurnal timescales. These variations can drive significant changes in subglacial mechanical conditions. The instrument records presented above suggest a seasonal change in sticky-spot geometry. In addition, Fischer (1995) has suggested that the effectiveness of local sticky spots can vary on diurnal timescales. Such temporal variations are in marked contrast to the relatively fixed sticky spots assumed to occur beneath ice streams. Because the water found beneath ice streams is generated by basal melt, hydraulic conditions beneath the ice streams can be remarkably consistent. Without the diurnal and seasonal variations in meltwater input, basal mechanical conditions – and therefore the location of sticky spots – are expected to be far more stable beneath ice streams than alpine glaciers. Diurnal variations in basal hydrological and mechanical conditions beneath an alpine glacier are investigated in the following chapters.

While the events of 11 June 1995 clearly demonstrate how changes in subglacial hydrological conditions strongly influence glacier dynamics, they also serve to illustrate how unstable situations can be quickly accommodated by mechanical adjustments at the glacier bed. Pressure transducer records indicate that hydraulic connection was established simultaneously over a $\sim$20 000 m^2 area, creating a region of instability that could have covered much of this region. This raises the question of how the glacier response would have differed had the unstable region been larger. Any portion of the driving stress not supported by the unstable region would be transferred to surrounding regions (e.g., Iverson, 1999; Truffer and others, in press). Sufficiently large transferred stresses could exceed the strength of sediments in the regions balancing the driving stress or of the ice itself. Extensive failure at the ice–bed interface could result in widespread mechanical instability and, ultimately, glacier surging. Because the removal of basal waters

increases coupling between the glacier and its bed, it is likely that the establishment of a high-capacity drainage system precludes formation of an unstable region large enough to enable surging. Thus while seasonal hydraulic switching can create brief periods of glacier instability, greater overall stability results from the increased removal of basal water following the establishment of a drainage system.

Chapter 4

A coupled three-column model of subglacial hydromechanical behaviour

4.1 Introduction

Sediment deformation and basal sliding can contribute greatly to the motion of glaciers that are underlain by water-saturated sediments. Basal motion is the dominant flow mechanism of some alpine glaciers (e.g., Raymond, 1971; Engelhardt and others, 1979; Boulton and Hindmarsh, 1987) and provides the key to understanding fast flow of ice streams (e.g. Blankenship and others, 1986; Alley and others, 1987a,b), tidewater glaciers (Meier and Post, 1987) and surging glaciers (e.g., Meier and Post, 1969; Kamb and others, 1985; Fowler, 1987; Kamb, 1987; Raymond, 1987). Much recent emphasis has been placed on the flow dynamics of Antarctic ice streams, which play an important role in the mass balance of the potentially-unstable West Antarctic Ice Sheet (Mercer, 1978) and provide modern analogues to fast-flowing regions of the Laurentide and Cordilleran Ice Sheets inferred from geologic evidence (e.g., Morner and Dreimanis, 1973; Clayton and Moran, 1982; Brown and others, 1987). Despite the fundamental role basal motion plays in glacier dynamics, our understanding of the underlying processes remains incomplete.

While early models of basal motion assumed that glaciers slide over a clean rigid bed (e.g., Weertman, 1957; Lliboutry, 1968, 1987; Nye, 1969; Kamb, 1970), measurements of sediment deformation at the margin of Breidamerkurjökull, Iceland (Boulton and Jones, 1979; Boulton and Hindmarsh, 1987) identified an additional component of basal motion.

The interest in basal deformation was further stimulated by the discovery of a metres-thick layer of water-saturated sediments beneath Antarctic ice stream B (Blankenship and others, 1986), which was interpreted to be soft and deforming (Alley and others, 1986). The flow characteristics of till play a critical role in the stability of ice sheets and glaciers, as an ice mass underlain by a highly-nonlinear till is more prone to unstable behaviour than is one resting on a linear-viscous till (Alley, 1990; Kamb, 1991). The rheological nature of till remains as one of the more pressing questions in glaciology. Boulton and Hindmarsh (1987) concluded that till behaviour is only slightly nonlinear, and models of ice stream dynamics have typically assumed till to behave as a linear-viscous (Alley and others, 1987b; MacAyeal, 1989) or mildly nonlinear (Alley, 1989) fluid. In contrast, shear tests on till samples recovered from beneath ice stream B suggest behaviour that is highly non-linear (Kamb, 1991) or independent of the applied shear stress (Tulaczyk and others, 2000a). Rate-independent behaviour is also indicated by ring-shear tests performed on tills collected from beneath the margin of Storglaciären, Sweden and from part of the southern margin of the Laurentide ice sheet (Iverson and others, 1997; Iverson and others, 1998). *In situ* measurements of sediment deformation, till strength and water pressure by Hooke and others (1997) also suggest highly-nonlinear till behaviour. Another area of interest is the relative contribution of glacier sliding and sediment deformation to total basal motion.

Since 1988, investigations into the nature of interactions between subglacial hydrological and mechanical conditions have been performed at Trapridge Glacier, Yukon Territory, Canada. Trapridge Glacier is underlain by a till layer that is up to ~10 m thick in some locations (Stone, 1993). Studies by Blake (1992) indicate that the top ~0.30 m of the till layer is actively deforming. Basal sliding and sediment deformation contribute roughly equally to basal motion, which accounts for ~90% of the total ice flow rate; the remaining ~10% is due to creep of the glacier ice (Blake, 1992). Of particular interest are

the effects of variations in drainage system pressure on sediment deformation (Blake and others, 1992), till strength (Fischer and Clarke, 1994) and basal sliding (Blake and others, 1994; Fischer and Clarke, 1997a, 1997b). Regions that are hydraulically connected to the subglacial drainage system typically show strong diurnal variations in basal water pressure and mechanical responses. One aim of the Trapridge Glacier project is to elucidate the mechanisms that drive these variations.

I present a simple hydromechanical model of the processes governing basal motion of a soft-bedded alpine glacier based on our observations at Trapridge Glacier. The glacier bed is classified into three general regions: soft-bedded regions that are hydraulically-connected to the subglacial drainage system, soft-bedded but poorly connected regions and hard-bedded regions. Each basal region is modelled as a single one-dimensional column. The time-evolution of pore-water pressure, till dilatancy, sediment deformation and glacier sliding is calculated in the soft-bedded regions; the hard-bedded region is considered rigid and impermeable. Till properties are determined by the pore-water pressure p, porosity n and preconsolidation history of the till. The columns are coupled by a simple ice-dynamics model, allowing investigation of the effects of shear stress bridging between regions.

Sediment deformation profiles are calculated using four different till flow laws, including linear-viscous, nonlinear-viscous, nonlinear-Bingham and Coulomb-plastic (i.e., rate independent). I model instrument responses for a variety of sensors from the calculated pore-water pressure, till deformation, sliding and till strength conditions. These synthetic responses are compared to simultaneous measurements of basal sliding, sediment strength, sediment deformation, basal water pressure and pore-water pressure within the till layer recorded during July 1996 at Trapridge Glacier. Comparison of model responses with field records allows us to test proposed till flow laws and provides a framework for further examining our understanding of basal processes.

In this chapter I develop mathematical relations for the time evolution of pore-water pressure, till porosity, shear stress transfer between basal regions, sediment deformation and glacier sliding. I also develop models describing instrument responses to the modelled hydrological and mechanical conditions. In Chapter 5 I discuss the application of this model to the discrimination of proposed till flow laws.

4.2 The model

4.2.1 Basal representation and model geometry
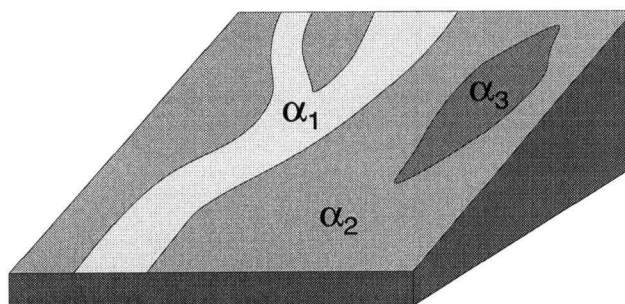
Figure 4.1: Representation of glacier bed used in model. Soft-bedded regions that are hydraulically-connected to the subglacial drainage system cover areal fraction α_1, unconnected soft-bedded regions fraction α_2, and hard-bedded regions fraction α_3.

Spatial variations in drainage system morphology and sediment properties lead to considerable nonuniformity in mechanical and hydraulic characteristics of the bed. Much complexity could be introduced to account for these variations and may eventually prove necessary to explain the broad range of subglacial phenomena observed in instrument records. Our goal, however, is to explore general subglacial behaviours under typical conditions. I thus take a simplified view of the subglacial environment, in which the glacier bed is classified into three categories (Fig. 4.1): (1) soft-bedded regions that are
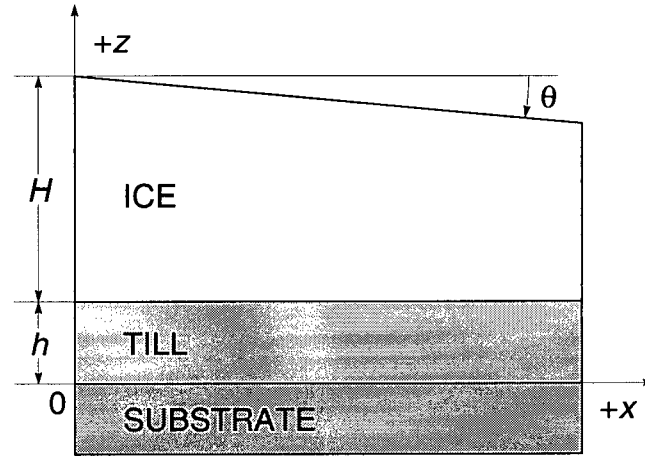
Figure 4.2: Coordinate system for soft-bedded regions.

hydraulically-connected to the subglacial drainage system, (2) soft-bedded but poorly-connected regions and (3) hard-bedded regions. While no assumptions are made about the actual distribution of bed types, each region is assumed to cover an areal fraction α_i of the bed such that

$$\alpha_1 + \alpha_2 + \alpha_3 = 1. \tag{4.1}$$

Consider a glacier with geometry shown in Figure 4.2. The glacier is assumed to rest on a horizontal bed and to have uniform surface slope θ. Ice thickness at the location of each column is H; the ice-overburden pressure is thus $p_I = \rho_I g H$ and the driving stress $\rho_I g H \sin \theta$. Till in soft-bedded regions is assumed to have uniform thickness h. The z axis is oriented vertically, positive upward with the origin located at the base of the till layer. The x axis is taken to be aligned with the direction of glacier flow.

In the following sections I will develop relations for the time-evolution of till porosity, hydraulic permeability, pore-water pressure, and sediment deformation profiles. I will also discuss the methods used to model glacier sliding and the transfer of driving stress between regions. Finally, I develop relations for calculating the responses of a number of

instruments to the modelled basal conditions.

4.2.2 Till porosity and dilatancy

Subglacial sediment is considered a fully-saturated two-component mixture comprising water, having density ρ_w and occupying a volume fraction n, and solid particles having density ρ_s and occupying a volume fraction $1 - n$. It is usual and convenient to assume that the solid phase is incompressible and that water satisfies a simple equation of state

$$\rho_w(p) = \rho_w(p_0) \exp[\beta(p - p_0)] \tag{4.2}$$

where β is the coefficient of compressibility, p the water pressure and p_0 a reference pressure value. The compressibility of the bulk water–solid mixture is a more subtle matter. By compressing the sediment and expelling water the bulk density is increased; by shearing it, assuming the mixture is dilatant, the porosity n is increased and bulk density decreases.

Although the water content of till is typically expressed in terms of porosity n, use of the void ratio e allows us to apply equations derived from geotechnical measurements of soil compressibility. Conversion between the two variables is a simple matter, as porosity and void ratio are related by

$$n = \frac{e}{1 + e}. \tag{4.3}$$

It follows that

$$\frac{\partial n}{\partial t} = \frac{1}{(1 + e)^2} \frac{\partial e}{\partial t}. \tag{4.4}$$

As noted earlier, subglacial water pressure is often expressed in terms of effective pressure $p' = p_I - p$, where p_I is the ice overburden pressure. Although water pressure is

the measurable quantity, the effective pressure p' is of greater significance to soil mechanics because it represents the portion of the total pressure acting on the solid skeleton. Pressure records are alternately expressed in terms of the pressure head $p_h = p/\rho_w g$.

The compressibility α of a soil, which can be expressed as

$$\alpha = \frac{1}{1-n}\frac{\partial n}{\partial p}, \tag{4.5}$$

is strongly dependent on the strain history of the soil. Compression of a soil that has never been subjected to loading (a "virgin soil") results in repositioning of grains in the solid matrix and thus a decrease in porosity or void ratio. Because the grains do not return to their original positions following subsequent unloading, the decrease in void ratio is largely irreversible. Following Clarke (1987b), I express the void ratio of a virgin soil as

$$e = e_0 - \frac{1}{B_c}\ln\left[(p' + p_1')/p_0'\right], \tag{4.6}$$

where B_c is a compression index and e_0 and p_0 are reference values of void ratio and effective pressure. The term p_1 prevents the void ratio from diverging as p' approaches zero, and can be determined by the void ratio e_1 at zero effective pressure:

$$p_1' = p_0'\exp\left[-B_c(e_1 - e_0)\right]. \tag{4.7}$$

Equation (4.6) defines the "normal consolidation line" (NCL; Fig. 4.3, long dashes), which relates the void ratio to effective stress for a virgin soil. States with lower void ratios for a given effective pressure are considered overconsolidated and are assumed to behave elastically so that further compaction under compression is recoverable. A "swelling index" B_s replaces B_c in the equation relating void ratio to effective pressure
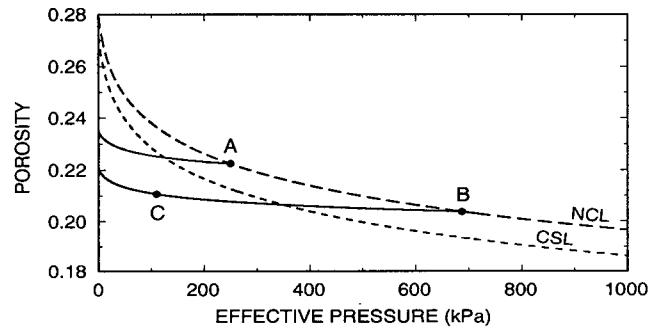
Figure 4.3: Compressibility characteristics of modelled till, adapted from Clarke (1987b, Fig. 1). The normal consolidation line (NCL, long dashes) relates porosity to effective pressure for virgin, or previously uncompressed, till. The solid lines intersecting the NCL at A and B ("swelling lines") demonstrate compressibility characteristics of overconsolidated tills. If a normally consolidated till at point A is subjected to increasing effective pressure, porosity decreases until point B is reached. The effective pressure corresponding to point B is called the preconsolidation pressure. If the effective pressure is subsequently reduced, the former compression state is not recoverable, and the state path follows a swelling line to point C. If effective pressure is then increased, the state path again traverses the swelling line to point B and then follows the normal consolidation line. The critical state line (CSL, short dashes) represents the porosity of a fully dilated till. Shearing drives the consolidation state vertically towards the CSL at a rate proportional to both the rate of shearing and the distance from the CSL. States lying above the CSL compact upon deformation; porosity of states lying below the CSL increase with deformation.

for overconsolidated states (Clarke, 1987b):

$$e(p', P') = e_0 - \left(\frac{1}{B_c} - \frac{1}{B_s}\right) \ln\left[(P' + p_1')/p_0'\right]$$
$$- \frac{1}{B_s} \ln\left[(p' + p_1')/p_0'\right].$$

(4.8)

The term P' is the preconsolidation effective pressure, determined by

$$P' = \begin{cases} p' & \text{on NCL} \\ p'_0 \left[\exp \left(\dfrac{e - e_0}{\frac{1}{B_s} - \frac{1}{B_c}} \right) \right] \left(\dfrac{p' + p'_1}{p'_0} \right)^{\frac{1}{1 - \frac{B_s}{B_c}}} - p'_1 & \text{left of NCL.} \end{cases} \tag{4.9}$$

Because changes in effective pressure affect the void ratio of normally-consolidated and overconsolidated tills differently, the compressibility α depends on the consolidation state:

$$\alpha(p') = \begin{cases} \dfrac{1}{(1 + e)B_c(p' + p'_1)} = \dfrac{1 - n}{B_c(p' + p'_1)} & \text{on NCL} \\ \dfrac{1}{(1 + e)B_s(p' + p'_1)} = \dfrac{1 - n}{B_s(p' + p'_1)} & \text{left of NCL.} \end{cases} \tag{4.10}$$

Many granular materials exhibit dilatancy, or a change in porosity upon shearing (Reynolds, 1885; Andrade and Fox, 1949). Dilatant expansion can increase the porosity of an overconsolidated till, and thus basal deformation can influence the porosity and permeability structure of subglacial sediments. Given sufficient shearing, the void ratio of a soil will reach a critical state e_{CS} determined by the relation

$$e_{CS}(p') = e_0^\dagger - \frac{1}{B_c} \ln \left[(p' + p'_1)/p'_0 \right] \tag{4.11}$$

(Clarke, 1987b) in which $e_0^\dagger$ is a reference void ratio value and B_c is the compression index used in (4.6). Equation (4.11) defines the "critical state line"(CSL; Fig. 4.3, short dashes), which is parallel to the NCL but yields slightly lower void ratio values for a given effective stress. States with lower void ratios for a given effective pressure CSL expand upon shearing, while states which lie between the CSL and NCL become more closely packed when sheared. I assume the rate of expansion or contraction to be proportional to both the strain rate in the soil and the difference between actual and critical-state void ratios:

$$\dot{e}_D(\dot{\varepsilon}) = -D_0 \dot{\varepsilon}(e - e_{CS}). \tag{4.12}$$

Here $\dot{e}_D$ is the rate-of-change in void ratio due to dilatant reorganization and D_0 is a scaling factor. Differentiating (4.6) and (4.8) with respect to time and adding (4.12) (and noting that $\partial p / \partial t = -\partial p' / \partial t$ for constant values of p_I) yields

$$\frac{\partial e}{\partial t} = \begin{cases} \dfrac{1}{B_s(p' + p_1')}\dot{p} - D_0\dot{\varepsilon}(e - e_{CS}) & \text{left of NCL} \\[3mm] \dfrac{1}{B_c(p' + p_1')}\dot{p} - D_0\dot{\varepsilon}(e - e_{CS}) & \text{on NCL.} \end{cases} \tag{4.13}$$

It follows from (4.4) that

$$\frac{\partial n}{\partial t} = \begin{cases} \dfrac{1}{(1 + e)^2}\left[\dfrac{1}{B_s(p' + p_1')}\dot{p} - D_0\dot{\varepsilon}(e - e_{CS})\right] & \text{left of NCL} \\[3mm] \dfrac{1}{(1 + e)^2}\left[\dfrac{1}{B_c(p' + p_1')}\dot{p} - D_0\dot{\varepsilon}(e - e_{CS})\right] & \text{on NCL,} \end{cases} \tag{4.14}$$

Equation 4.14 allows us to relate the time-evolution of the porosity to the rate-of-change of pore-water pressure, the strain rate and the consolidation state.

4.2.3 Hydraulic permeability

The porosity n of a soil gives an averaged measure of the packing of grains in the solid matrix. Because tight packing of the grains results in highly restricted water passageways, low-porosity soil will exhibit a low hydraulic permeability κ. Much effort has been made to determine the relationship between the porosity and permeability of a soil. Perhaps best known is the Kozeny-Carman relation (Carman, 1961):

$$\kappa = \frac{n^3}{5(1 - n)^2 S_0^2}. \tag{4.15}$$

The term S_0 is the solid surface area per unit volume; the factor of $1/5$ is that suggested by Carman. This relation has yielded reasonable estimates of porosity for clean sands (Bourbié and others, 1987), but its applicability to tills remains unclear.

4.2.4 Lagrangian representation of water transport

The usual approach to modelling water flux through a porous medium is to cast the problem in terms of the Eulerian, or spatial, description. This approach is appropriate for elastic aquifers that experience only small strains, in which case the distinction between unstrained and strained states can be neglected. For materials that can undergo a large volume change, such as dilatant till, this simplification is inappropriate. One possible choice is to describe various physical properties (such as the pore-water pressure p) as functions of a spatially-fixed coordinate system x_k so that the spatial and temporal variability of p is expressed as $p(x_k, t)$. The disadvantage of this approach is that the deforming medium moves relative to the spatially-fixed coordinate system. An alternative approach is to express spatial and temporal variability in terms of the initial configuration so that $p(X_k, t)$ describes the spatial and temporal distribution of pressure. To be mathematically rigorous, it is customary to emphasize the fact that $p(x_k, t)$ and $p(X_k, t)$ are different mathematical functions by introducing two different pressure functions that describe the same physical property. In the following discussion, Eulerian functions are denoted by a "tilde" (e.g., in the Eulerian scheme $n = \tilde{n}(x_k, t)$, and in the Lagrangian $n = n(X_k, t)$).

I assume that properties of the bed are uniform for some distance both up- and down-glacier from the location of the till column. Thus as deformation within the column moves sediments down-glacier and therefore away from the one-dimensional column, those sediments are immediately replaced by up-glacier sediments with identical properties. With this assumption, we can express p and other physical properties as functions their height (Z, t) within the till column, where Z is the initial position of a particle in the column. The height of such a particle changes with time in response to dilation and compression, and thus a solid particle having initial position Z will at some later time

be located at z, where

$$z(Z,t) = \int_0^Z \left(\frac{1 - n(Z',0)}{1 - n(Z',t)}\right) dZ'. \qquad (4.16)$$

From (4.16) the Jacobean of the transformation from Z to z is

$$J(t) = \frac{\partial z}{\partial Z} = \frac{1 - n(Z,0)}{1 - n(Z,t)}. \qquad (4.17)$$

If the till layer thickness is h at time $t = 0$, at some later time the thickness is

$$\tilde{h}(t) = \int_0^{h(0)} J(t) \, dZ. \qquad (4.18)$$

The solid mass m_s (per unit area of bed) can be expressed in either the spatial description or the material description. If we make the usual assumption that solids are incompressible, we have in the spatial description

$$\tilde{m}_s = \rho_s \int_0^{\tilde{h}(t)} \left(1 - \tilde{n}(z,t)\right) dz \qquad (4.19)$$

and in the material description

$$m_s = \rho_s \int_0^{h(0)} \left(1 - n(Z,t)\right) J(t) \, dZ. \qquad (4.20)$$

The former expression is likely to be more familiar but the latter one, though ostensibly more complicated, has computational advantages. The condition for conservation of solid mass is $dm_s/dt = 0$, which leads to the local-form expressions

$$\frac{\partial}{\partial t}\left(1 - \tilde{n}(z,t)\right) + \frac{\partial}{\partial z}\left(\tilde{v}_s(z,t)[1 - \tilde{n}(z,t)]\right) = 0 \qquad (4.21)$$

$$\frac{\partial}{\partial t}\left[\left(1 - n(Z,t)\right) J(t)\right] \equiv 0. \qquad (4.22)$$

The term v_s in (4.21) is the component of sediment velocity in the z direction. This equation, derived using the Reynolds' Transport Theorem, is similar in form to (but distinct from) the material derivative. The term $v_s(z,t)[1 - n(z,t)]$ represents the *convective flux of solid volume.*

Equation (4.21) is a condition that must be satisfied if mass conservation is satisfied, whereas (4.22) is an identity: solid mass is automatically conserved in the Z–t coordinate system. Thus in the Lagrangian representation the solid mass balance condition is automatically satisfied and the water balance condition is the one that leads to field equations. In the Lagrangian representation the water mass (per unit area of bed) is

$$m_{\mathrm{w}} = \int_0^{h(0)} \rho_{\mathrm{w}}(Z,t) n(Z,t) J(t) \, dZ. \tag{4.23}$$

Within the region $0 \le Z \le h(0)$ water mass varies because of dilatation or compression of the till layer. This change in water mass is a consequence of the fact that water moves independently of the solid matrix. As the pore volume in a given region increases or decreases in response to dilatation or contraction of the solid matrix, water flows in or out of the region to accomodate the changes in pore volume. The change in total water mass for column of till is given by the difference in water mass flux $\rho_{\mathrm{w}} q_{\mathrm{w}}$ between the upper and lower boundaries of the column $Z = 0$ and $Z = h$; here q_{w} denotes the volume flux of water. Thus

$$\frac{dm_{\mathrm{w}}}{dt} = -\rho_{\mathrm{w}}(h,t) q_{\mathrm{w}}(h,t) + \rho_{\mathrm{w}}(0,t) q_{\mathrm{w}}(0,t) \tag{4.24}$$

$$= -\int_0^{h(0)} \frac{\partial}{\partial Z}\Big(\rho_{\mathrm{w}}(Z,t) q_{\mathrm{w}}(Z,t)\Big) \, dZ. \tag{4.25}$$

Equations (4.23) and (4.25) lead to the local form expression of water balance

$$\frac{\partial}{\partial t} \{\rho_{\mathrm{w}}(Z,t) n(Z,t) J(t)\} = -\frac{\partial}{\partial Z} \{\rho_{\mathrm{w}}(Z,t) q_{\mathrm{w}}(Z,t)\}. \tag{4.26}$$

From (4.26) it is clear that changes in pore volume due to dilatation or compression or water mass due to changes in pore volume space From (4.2) we get

$$\frac{\partial \rho_{\mathrm{w}}}{\partial t} = \beta \rho_{\mathrm{w}} \frac{\partial p}{\partial t} \tag{4.27}$$

$$\frac{\partial \rho_{\mathrm{w}}}{\partial Z} = \beta \rho_{\mathrm{w}} \frac{\partial p}{\partial Z}. \tag{4.28}$$

I assume that transport of water in the cross- or down-glacier directions is negligible compared to vertical flow driven by diurnal pressure variations. Water flux q_w in the column is assumed to be governed by Darcy's law, which in the material description is given by

$$q_w(Z,t) = -\frac{\kappa(Z,t)}{\mu_w}\left[\frac{1}{J(t)}\frac{\partial p(Z,t)}{\partial Z} + \rho_w g\right].\tag{4.29}$$

Expanding the left-hand side of (4.26) and using relations (4.5), (4.17) and (4.27) leads to

$$\frac{\partial}{\partial t}\{\rho_w(Z,t)n(Z,t)J(t)\} = \rho_w(Z,t)\big(\alpha(p) + n(Z,t)\beta\big)J(t)\frac{\partial}{\partial t}p(Z,t).\tag{4.30}$$

Expanding the right-hand side of (4.26) and incorporating (4.28) gives

$$-\frac{\partial}{\partial Z}\Big(\rho_w(Z,t)q_w(Z,t)\Big) = -\rho_w(Z,t)\left[q_w(Z,t)\beta\frac{\partial}{\partial Z}p(Z,t) + \frac{\partial}{\partial Z}q_w(Z,t)\right].\tag{4.31}$$

Equating (4.30) and (4.31), substituting the Lagrangian expression of Darcy's law (4.29), and rearranging yields the pressure evolution equation

$$\begin{aligned}
\frac{\partial}{\partial t}p(Z,t) = \Bigg\{&\frac{1}{\mu}\left[\frac{d\kappa}{dp} + \beta\,\kappa(p)\right]\left[\frac{1}{J(t)}\frac{\partial p}{\partial Z} + \rho_w g\right]\frac{\partial p}{\partial Z}\\
&-\frac{\kappa(p)}{\mu(1-n(Z,0))}\frac{dn(p)}{dp}\left(\frac{\partial p}{\partial Z}\right)^2 + \frac{\kappa(p)}{\mu}\frac{1}{J(t)}\frac{\partial^2 p}{\partial Z^2}\Bigg\}\\
&\times\left\{\big(\alpha(p) + n(Z,t)\beta\big)J(t)\right\}^{-1}.
\end{aligned}\tag{4.32}$$

4.2.5 Till flow laws

Proposed empirical till flow laws, which relate the strain rate to shear stress and effective pressure conditions, can be written in the general form

$$\dot{\varepsilon} = \begin{cases} B(\tau - \sigma_Y)^a(p' + p_1')^{-b} & \text{if } \tau \geq \sigma_Y \\ 0 & \text{if } \tau < \sigma_Y. \end{cases}\tag{4.33}$$
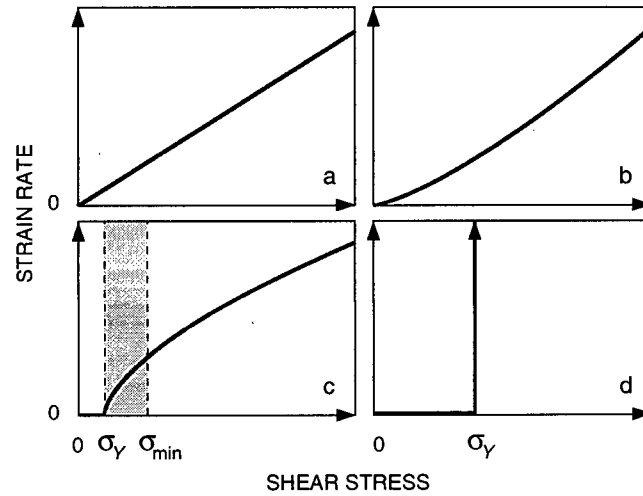
Figure 4.4: Stress-strain rate relations for modelled till flow laws. (a) Linear-viscous till. (b) Nonlinear-viscous till. Flow behaviour shown is that for values of $a = 1.33$ and $b = 1.80$. (c) Nonlinear-Bingham till. Flow behaviour shown is that for values of $a = 0.625$ and $b = 1.25$. Shaded region represents transition zone between elastic $(\tau < \sigma_Y)$ and viscous $(\tau > \sigma_{min})$ behaviours. The term σ_{min} is defined in section 4.2.9. (d) Coulomb-plastic till. Below yield stress σ_Y no deformation occurs; above this value deformation is instantaneous and proceeds at the rate required to prevent the applied stress from exceeding the yield stress.

Here B is a scaling constant, σ_Y the yield strength of the material and p' the effective pressure. The constant term p'_1 is to prevent runaway deformation as $p' \rightarrow 0$. In till mechanics, the yield stress σ_Y is typically determined by the Mohr-Coulomb failure criterion

$$\sigma_Y = c_0 + p' \tan \phi, \qquad (4.34)$$

in which c_0 is the cohesion, ϕ the friction angle and p' the effective pressure.

I will investigate four till flow laws. The first assumes till to deform as a Newtonian viscous material (Fig. 4.4a):

$$\dot{\varepsilon} = \frac{1}{2\eta_0}\tau. \qquad (4.35)$$

This is equivalent to assigning values $B = 1/2\eta_0$, $a = 1$, $b = 0$, $p' = 0$ and $\sigma_Y = 0$ in (4.33). This relation has been used to model the flow of ice streams (e.g., MacAyeal, 1989; Alley and others, 1987b; Alley and others, 1989) and alpine glaciers (e.g., Fischer and Clarke, 1994).

Two flow laws proposed by Boulton and Hindmarsh (1987) are investigated. These relations are were derived from long-term observations of till deformation and effective pressure profiles and shear stress taken in near-margin till beneath Breidamerkurjökull, Iceland. These observations represent the only set of field data extensive enough to determine a flow relation for till. The first relation considers till a nonlinear-viscous material (Fig. 4.4b):

$$\dot{\varepsilon} = B_1 \tau^a (p')^{-b}. \qquad (4.36)$$

The second relation treats till as a Bingham material (Fig. 4.4c), in which the strain rate depends on the amount by which the shear stress exceeds the yield strength σ_Y:

$$\dot{\varepsilon} = B_2 (\tau - \sigma_Y)^a (p')^{-b}. \qquad (4.37)$$

The shear stress τ and effective pressure p' in (4.36) and (4.37) are expressed in kPa, and the yield strength σ_Y is determined by the Mohr-Coulomb failure criterion. The till behaves elastically at stress values below σ_Y; at values above the yield strength the till deforms viscously.

The fourth flow law investigated assumes that till behaves as a Coulomb-plastic material (Fig. 4.4d). The strength of such a material is independent of the strain rate but is linearly related to the effective pressure. Laboratory studies by Iverson and others (1998) and Tulaczyk and others (2000a) suggest that till behaviour can be approximated as Coulomb-plastic, and this behaviour has been used to model basal motion of the Puget Lobe of the Cordilleran Ice Sheet (Brown and others, 1987) and of both alpine glaciers

(e.g., Iverson, 1999) and ice streams (e.g. Tulaczyk and others, 2000b). Coulomb-plastic behaviour is given by (4.33) for $a = \infty$. Highly nonlinear flow is also suggested by analysis of till from the base of Antarctic Ice Stream B by Kamb (1991), which yielded values of a as large as ~ 100; such highly nonlinear flow would be difficult to distinguish from purely plastic behaviour.

Coulomb-plastic materials exhibit highly nonlinear behaviour. At stresses below the yield strength determined by the Mohr-Coulomb failure criterion (4.34), the behaviour is elastic and no permanent deformation occurs. Flow at stress values above the yield strength is instantaneous:

$$\dot{\varepsilon} = \begin{cases} \infty & \text{if } \tau \geq \sigma_Y \\ 0 & \text{if } \tau < \sigma_Y. \end{cases} \tag{4.38}$$

The use of the term ∞ in (4.38) indicates that no direct relationship between shear stress and deformation rate exists for values of $\tau \geq \sigma_Y$; deformation occurs at such a rate to prevent the applied shear stress from exceeding σ_Y. The abrupt transition between non-deforming and deforming states in 4.38 creates a high degree of numerical stiffness. I reduce this stiffness by modelling Coulomb-plastic behaviour as

$$\dot{\varepsilon} = \frac{1}{2}\dot{\varepsilon}_0 \left[1 + \tanh\left(2\pi(\tau - \sigma_Y)/\Delta\tau\right)\right]. \tag{4.39}$$

Assigning a sufficiently large value to the reference strain rate $\dot{\varepsilon}_0$ and a small failure range $\Delta\tau$ allows close approximation to the Coulomb-plastic behaviour of 4.38.

Strictly speaking, the rate independence shown in Figure 4.4d and modelled in Equations (4.38) and (4.39) is only true for tills that have been strained sufficiently to reach a residual state. In laboratory testing, tills often show a brief initial period during which the strength varies slightly. Such variations are caused by reorganization of the till fabric in response to the imposed stress field. Although a more complete picture of till behaviour would account for these variations, the processes that govern them are poorly

understood. In the modelling studies that follow, I will assume the till to be in a residual state.

4.2.6 Deformation profile

Assuming simple shear in the till, the strain rate is given by

$$\dot{\varepsilon} = \frac{1}{2J(t)} \frac{\partial v_x}{\partial Z}. \tag{4.40}$$

Solving (4.40) for $\partial v_x / \partial Z$ and integrating up from the base of the till layer yields the velocity profile $v(Z, t)$:

$$v_x(Z, t) = 2 \int_0^Z J(t)\, \dot{\varepsilon}(Z', t)\, dZ' \tag{4.41}$$

Depending on the flow law chosen, the strain rate $\dot{\varepsilon}(Z, t)$ is determined by equation (4.35), (4.36), (4.37) or (4.39). It is assumed that there is no slip between the till base and the underlying substrate. Till displacement is calculated by integrating the velocity field with respect to time:

$$\frac{\partial}{\partial t} s(Z, t) = v_x(Z, t) \tag{4.42}$$

4.2.7 Glacier sliding

Models have been developed to relate glacier sliding to basal shear stress, effective pressure and bed roughness (e.g., Weertman, 1957, 1964; Lliboutry, 1968, 1987; Kamb, 1970). These models assume the glacier bed to be rigid and impermeable, and thus I present an alternate sliding model. Increased subglacial water pressure facilitates both basal sliding (by decoupling ice from the bed) and deformation (through weakening of till as pore-water pressure increases). These two phenomena can occur simultaneously, and where both operate they compete: decoupling of the ice–bed interface allows sliding to

occur but reduces the transmission of shear stress to the till and thus decreases the deformation rate. High subglacial water pressures weaken ice-bed coupling through the submergence of roughness features. In this manner the magnitude of shear stress transmitted to the bed decreases with increasing water pressure. The balance of the driving stress is transferred to neighbouring regions by glacier sliding.
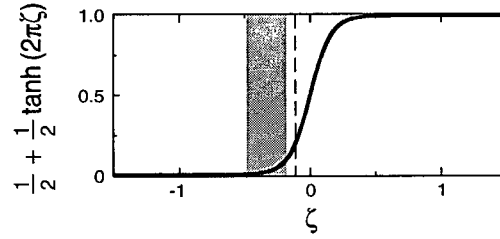
Figure 4.5: Variation of the sliding coefficient C_{SL} with water pressure. The variable ζ is related to the water pressure at the ice–bed interface by $\zeta(t) = \left(p(h_0, t) - p_{SL}\right)/\Delta p_{SL}$ (see text for details). Given the values of p_{SL} and Δp_{SL} used the model simulations of Chapter 5 (Table 5.5), modelled drainage system pressures lie within the shaded region above. Modelled ice overburden pressure is indicated by the dashed vertical line.

I assume that the sliding velocity is related to the local driving stress τ acting upon the region by

$$v_{SL}(t) = C_{SL}(p)\frac{h_{SL}}{\mu_{SL}}\,\tau(t);\tag{4.43}$$

the sliding coefficient C_{SL} is assumed to be related to the water pressure at the ice–bed interface:

$$C_{SL}(p) = \frac{1}{2}\left[1 + \tanh\left(2\pi\frac{p(h_0, t) - p_{SL}}{\Delta p_{SL}}\right)\right].\tag{4.44}$$

As shown in Figure 4.5, the sliding coefficient varies between zero and unity depending on the water pressure at the ice–bed interface. At water pressures much greater than the reference pressure p_{SL} in 4.44, $C_{SL} = 1$ and the sliding velocity is $v_{SL} = (h_{SL}/\mu_{SL})\tau$. This

velocity is equal to the rate at which a layer of lubricating material with thickness h_{SL} and viscosity μ_{SL} would deform when subjected to a shear traction of magnitude τ. At such pressures, roughness features of the bed are assumed to be completely submerged and the shear stress is transferred to the bed by viscous coupling through the layer of lubricating material (hereafter referred to as a "slurry"). At water pressures that are significantly lower than the reference pressure, sliding is assumed to be negligible because of the strong mechanical coupling between the ice and bed provided by the roughness features. The transition between non-sliding and sliding modes is assumed to occur over a pressure range given by Δp_{SL}. In this transition zone, partial submergence of roughness features reduces their effectiveness and allows increased sliding rates. At these intermediate pressures, the shear traction is assumed to be transferred to the bed by a combination of mechanical resistance (provided by any unsubmerged roughness features) and viscous coupling (provided by the deforming slurry layer). It should be noted that the hyperbolic tangent $\tanh(x)$ is an exponential, rather than circular, function, and thus the factor of 2π appears to be misplaced. However, this factor has the effect of confining the range of pressures over which the transition between non-sliding and sliding behaviours occurs to the interval $p - p_{SL}/2\Delta p_{SL}$ and $p + p_{SL}/2\Delta p_{SL}$ (i.e. in the range $-0.5 < \zeta < 0.5$ in Fig. 4.5). Without this factor, the transition would occur over a wider range of pressures.

The sliding velocity v_{SL} is simply the rate-of-change of the sliding distance $s_{SL}(t)$, given by

$$\frac{\partial}{\partial t}s_{SL}(t) = v_{SL}(t) = C_{SL}(p(Z,t))\frac{h_{SL}}{\mu_{SL}}\tau(t). \qquad (4.45)$$

The total ice velocity and displacement in each column are simply the sum of deformational and sliding components:

$$V(t) = v(h(0),t) + v_{SL}(t) \qquad (4.46)$$

$$S(t) = s(h(0), t) + s_{SL}(t). \tag{4.47}$$

4.2.8 Ice-dynamics model and basal shear stress

For a glacier with thickness H and surface slope θ, the nominal shear stress acting upon the bed is $\tau_0 = \rho_I g H \sin \theta$. The shear stress in individual columns (or basal regions) can vary from this nominal value if basal conditions favour the transfer of stress between columns. For a glacier of uniform thickness and surface slope, transferred or longitudinal stresses can arise when basal drag varies between neighboring regions: a region in which basal motion occurs rapidly will transfer a portion of the nominal shear stress to regions that exhibit greater resistance to motion. Because subglacial water pressure strongly influences both sediment strength and basal sliding, diurnal pressure variations can drive a cyclic transfer of shear stress between regions of the bed. Although the transfer of shear stress between columns can result in unequal stress distribution, the area-averaged shear stress is equal to the nominal value:

$$\alpha_1 \tau_1 + \alpha_2 \tau_2 + \alpha_3 \tau_3 = \tau_0, \tag{4.48}$$

where α_1, α_2 and α_3 are assumed fixed. It follows that

$$\alpha_1 \frac{\partial}{\partial t} \tau_1 + \alpha_2 \frac{\partial}{\partial t} \tau_2 + \alpha_3 \frac{\partial}{\partial t} \tau_3 = 0. \tag{4.49}$$

A rigorous treatment of the transfer of stresses between regions would require computation of the full three-dimensional stress and velocity fields within the ice. Although such algorithms have been developed (e.g., Blatter 1995), they add greatly to the computational complexity and require knowledge of the distribution of basal stresses. I instead employ a simple ice-dynamics model adapted from Fischer and Clarke (1997b) that allows investigation of the effects of stress bridging while retaining computational simplicity. I assume that the columns representing the different basal regions are located across-slope
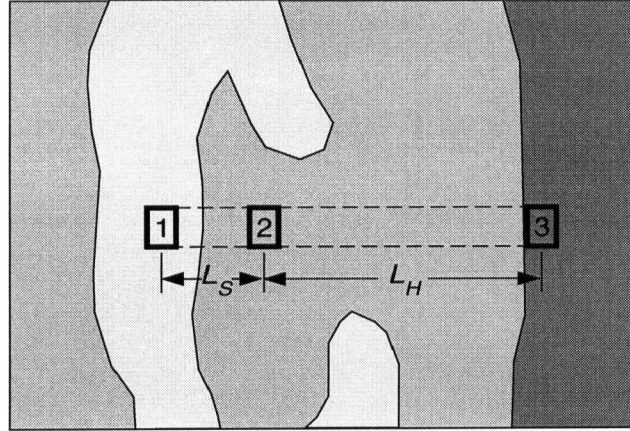
Figure 4.6: Plan view of glacier bed showing one possible configuration of basal regions. The till column arrangement is that used to determine stress transfer for column 2. Glacier flow is oriented towards the top of the page. Columns 1 and 2 are situated in connected (light grey) and unconnected (mid-tone grey) soft-bedded regions, with column 3 located in a hard-bedded region (dark grey). Soft-bedded columns 1 and 2 are separated by distance L_S; hard-bedded column 3 is distance L_H from column 1. This geometry allows calculation of stress bridging by considering only simple shear in the ice separating the columns.

(i.e. aligned perpendicularly to the flow direction) (Fig. 4.6). Soft-bedded regions are assumed to be separated by characteristic distance L_S; hard- and soft-bedded regions are separated by distance L_H. This geometry allows us to calculate stress bridging in terms of simple shear of the ice between the columns. Ice is treated as a nonlinear Maxwell material:

$$\dot{\varepsilon} = \frac{1}{2G_I}\dot{\tau} + A_0\tau^N. \tag{4.50}$$

The short-term elastic response is determined by the rigidity G_I; over long timescales the material deforms according to Glen's Law (Glen, 1958). If we designate the shear stress transferred from column b to column a as $\tau_{b\to a}$, rearranging (4.50) yields

$$\dot{\tau}_{b\to a} = 2G_I\left(\dot{\varepsilon}_{b\to a} - A_0\tau_{b\to a}^N\right). \tag{4.51}$$

Assuming uniform simple shear of the ice between columns gives

$$\dot{\varepsilon}_{b \to a} = \dot{\varepsilon}_{xy} = \frac{1}{2} \frac{\partial v_x}{\partial y} = \frac{\Delta V}{2L},$$ (4.52)

where $\Delta V = V_b - V_a$ is the difference in total ice velocity between columns and L is the characteristic distance separating columns. Depending on which pair of columns are being considered, L is replaced by either L_S or L_H. Substitution of (4.52) into (4.51) yields

$$\dot{\tau}_{b \to a} = 2G_I \left(\frac{\Delta V}{2L} - A_0 \tau_{b \to a}^N \right).$$ (4.53)

For situations in which $\dot{\tau}_{b \to a} = 0$, (4.53) reduces to

$$\frac{\Delta V}{2L} = A_0 \tau_{b \to a}^N.$$ (4.54)

It is apparent from (4.54) that for situations in which the velocity contrast ΔV remains constant, the shear stress $\tau_{b \to a}^N$ transferred between columns is simply equivalent to that required to drive an equivalent amount of ice deformation. Any increase in the velocity contrast ΔV results in a positive value of $\dot{\tau}_{b \to a}$ and thus the transfer of additional shear stress from column b to column a. Conversely, a decrease in ΔV reduces the transferred stress.

The preceding discussion considers stress bridging between two columns. Full accounting of stress bridging considers the transfers between each pair of columns and the relative areal coverage of each column in a manner that satisfies equation (4.49):

$$\frac{\partial}{\partial t} \tau_1 = \dot{\tau}_{2 \to 1} + \dot{\tau}_{3 \to 1}$$

$$\frac{\partial}{\partial t} \tau_2 = -\frac{\alpha_1}{\alpha_2} \dot{\tau}_{2 \to 1} + \dot{\tau}_{3 \to 2}$$ (4.55)

$$\frac{\partial}{\partial t} \tau_3 = -\frac{\alpha_1}{\alpha_3} \dot{\tau}_{3 \to 1} - \frac{\alpha_2}{\alpha_3} \dot{\tau}_{3 \to 2}.$$

Values for $\dot{\tau}_{2 \to 1}$, $\dot{\tau}_{3 \to 1}$ and $\dot{\tau}_{3 \to 2}$ are calculated by substituting appropriate values for velocity contrast ΔV, separation distance L and transferred stress $\tau_{b \to a}$ into (4.53). The

shear stress acting upon the till in a given region is assumed constant throughout the layer (i.e. no z-variation; Alley (1989b) has called this the "thin till approximation").

For simplicity I further neglect any vertical velocity gradient in the ice (i.e. the ice moves as plug flow). Although this assumption is not valid for regions in which ice–bed coupling is strong, it reasonably approximates the situation in soft-bedded regions. Ice deformation accounts for only $\sim 1\,\mathrm{m}$ of the approximately $\sim 30\,\mathrm{m}$ annual displacement measured in the study region at Trapridge Glacier (unpublished data, Trapridge Glacier), which is largely underlain by soft, deformable sediments (Blake, 1992; Blake and others, 1992). Other flow mechanisms, such as enhanced creep of the basal ice, regelation and ploughing, are also ignored.

This ice-dynamics model assumes uniform simple shear of ice between basal regions. Uniform deformation is likely to occur only if basal conditions are homogeneous across the bed separating the columns, as changes in basal conditions would tend to localize deformation. Blatter and others (1998) modelled the stress and velocity conditions in the vicinity of an isolated sliding spot in an otherwise homogeneous non-sliding slab. Their modelling results suggest that the surface velocity distribution would vary smoothly over lengthscales equivalent to several ice thicknesses. The assumption of uniform simple shear between columns is therefore likely to be a reasonable simplification.

4.2.9 Synthetic instrument responses

Instrument responses are modelled for four sensor types based on pore-water pressure, till strength, till deformation and sliding conditions in both soft-bedded regions. Instruments modelled include pressure transducers, ploughmeters (Fischer and Clarke, 1994), bed tilt sensors (Blake and others, 1992) and slidometers (Blake and others, 1994). In the field, these instruments are hammered ~ 0.05–$0.25\,\mathrm{m}$ into the subglacial till depending on instrument type, local bed properties, and degree of installation success. The true depth

of installation is uncertain, however, as hot-water drilling disturbs the sediments at the base of the borehole. In addition, it is possible for soft sediments to ooze up into the borehole. Because variations in installation depth influences the instrument response, I calculate instrument responses for a range of installation depths.

Bed tilt
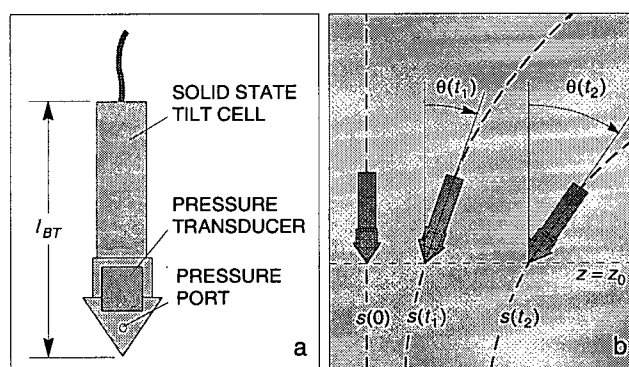
Figure 4.7: (a) Construction details for tilt cell and pore-water pressure transducer. Overall length is $l_{BT} = 0.11$ m. (b) Assumed tilt cell behaviour. The tilt cell is assumed vertical upon installation to depth Z_0. Deformation profiles s and corresponding tilt angles θ are shown for later times t_1 and t_2.

Tilt cells (Fig. 4.7a; Blake and others, 1992) measure deformation of the subglacial till. Upon installation the cell is oriented approximately vertically, and any deformation of till in the range of depth occupied by the sensor results in rotation of the device. Interpretations of bed tilt records (e.g., Blake and Clarke, 1992; Iverson and others, 1995) typically assume uniform deformation over a till layer several decimeters thick. If deformation occurs in discrete regions (as in the case of highly nonlinear till flow), the measured tilt rate can be strongly influenced by installation depth.

Assuming simple shear of the sediments, the average strain rate over the height of

the tilt cell is given by

$$\dot{\varepsilon} = \frac{1}{2}\frac{\partial \tan\theta_{BT}}{\partial t}. \tag{4.56}$$

The tilt cell is advected passively with the deforming till, with the top and bottom of the device taken to coincide with the deformation profile $s(Z,t)$ (Fig. 4.7b). The location of the instrument bottom is thus given by $[x_b(t), z_b(t)] = [s(Z_0,t), Z_0]$, where Z_0 is the installation depth. The tilt cell top is located by the point on the deformation profile with distance l_{BT} (the device length) away from $[x_b(t), z_b(t)]$. The tilt angle is given by

$$\theta_{BT} = \tan^{-1}\left(\frac{z_t - z_b}{x_t - x_b}\right). \tag{4.57}$$

Because the Eulerian coordinates z_b and z_t used in determining the tilt angle are calculated from the Lagrangian representation of the till matrix, rotation of the device due to dilatant expansion and contraction of the till is incorporated into (4.57).

Pressure transducer

Small pressure transducers are usually incorporated into the tilt cell housing (Fig. 4.7a), allowing simultaneous measurement of basal deformation and pore-water pressure. As the pressure transducer is built into the bottom of the device housing, and the pore-water pressure is given by

$$p_{PZ}(t) = p(Z_0, t) \tag{4.58}$$

where Z_0 is the installation depth of the tilt cell.

Slidometer

Slidometers (Blake and others, 1994) consist of a potentiometer, a spool of string and an anchor (Fig. 4.8). The potentiometer and spool are suspended in the borehole, and the anchor is hammered some distance into the subglacial sediment. As the glacier slides over the bed, string is pulled from the spool, turning the potentiometer. The displacement is
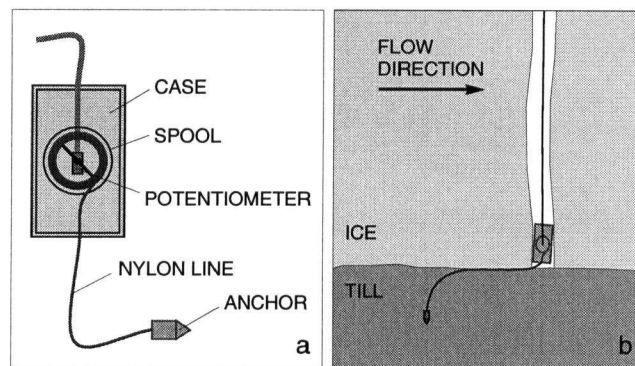
Figure 4.8: (a) Construction details for slidometer. (b) Installation geometry. Indicated sliding rate includes a component due to deformation of sediments above anchor.

then related to the potentiometer resistance measured by the data logger. Ideally, the measured displacement would result solely from glacier sliding and would be unaffected by basal deformation. Because it is necessary to firmly affix the string to the bed, the anchor is placed a finite distance into the till, and thus the displacement signal is contaminated by any till deformation above the anchor placement. Assuming that the slidometer string does not cut through the till and no slippage of the anchor, the total amount of displacement indicated by the slidometer is

$$
x_{SL}(t) = \left\{ \int_{Z_0}^{h(0)} J(t) \left[1 + \left(\frac{\partial x(Z,t)}{\partial Z} \right)^2 \right]^{\frac{1}{2}} dZ \quad - Z_0 \right\} + s_{SL}(t), \qquad (4.59)
$$

where $s_{SL}(t)$ is the true sliding distance and Z_0 the installation depth of the anchor. The first term on the right-hand-side of 4.59 is the component of total apparent sliding distance contributed by sediment deformation.

Ploughmeter

The ploughmeter (Fischer and Clarke, 1994) consists of a 1.54 m steel rod that is instrumented with strain gauges (Fig. 4.9). The ploughmeter is installed so that the tip is
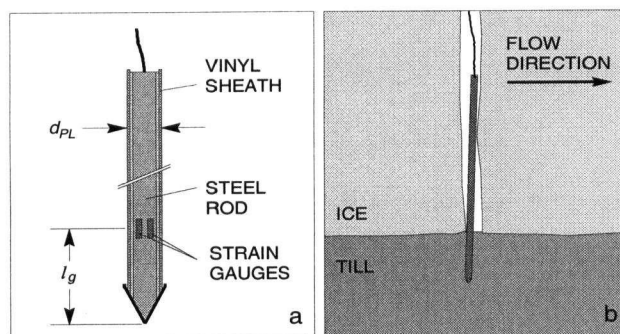
Figure 4.9: (a) Ploughmeter construction details. Overall length is 1.54 m, with a diameter $d_{PL} = 0.03$ m and tip-to-gauge-centre distance $l_g = 0.10$ m. (b) Installation geometry.

embedded ~0.1–0.2 m into the subglacial sediments. Relative motion between the sediments and the ploughmeter results in a drag force which bends the steel rod; this bending is in turn measured by the strain gauges. The magnitude of the bending moment depends on some combination of sediment strength and the rate at which the ploughmeter is dragged through the sediment; the functional dependence of these parameters is determined by the till flow law. Ploughmeters thus provide a means of measuring in-situ properties of subglacial till. The bending moment acting upon the ploughmeter tip is

$$M = \int_{Z_0}^{h_g} [h_g - Z] \, J(t) \, F'(Z) \, dZ, \tag{4.60}$$

where $F'(Z)$ is the force per unit length applied between Z and $Z + dZ$. The integration limits are the locations of the ploughmeter tip (Z_0) and the strain gauge centres ($h_g = Z_0 + l_g$, where l_g is the tip-to-gauge-centre distance). This relation assumes that the drag force is acting perpendicularly to the ploughmeter axis. This assumption is likely valid because the ploughmeter length is much greater than the borehole diameter. Furthermore, the ploughmeter is encased in a vinyl sheath, making regelation-driven intrusion of the upper portion of the ploughmeter into the borehole wall unlikely. As a

result, down-glacier rotation of the ploughmeter over time is likely to be insignificant.

Depending on the till flow law, one of two relations is used to calculate $F'(Z)$. For flow laws that exhibit linear or nearly-linear dependence on τ, $F'(Z)$ is obtained by approximating the ploughmeter as an ellipsoidal body with semi-major axis c_{PL}, assumed equivalent to the tip-to-gauge offset l_g, and semi-minor axis a_{PL}, taken as the ploughmeter radius. This is a reasonable approximation of the ploughmeter geometry, as the ploughmeter body is cylindrical for most of its length with a conical tip. The force acting upon such a body moving through a viscous fluid is proportional to both the velocity contrast $\Delta V(Z,t) = V(t) - v(Z,t)$ between the ploughmeter and sediments at depth Z and the effective viscosity η at that depth:

$$F' = \frac{4\pi\eta(Z,t)\Delta V(Z,t)}{\ln(2c_{PL}/a_{PL}) + 0.5}$$ (4.61)

(Batchelor, 1970; Cox, 1970; Tillett, 1970). The effective viscosity η, defined as

$$\eta(Z,t) = \frac{1}{2\dot{\varepsilon}(Z,t)}\tau(t),$$ (4.62)

incorporates any any stress- and pressure-dependent nonlinearities in flow; for linear-viscous tills $\eta(Z,t) = \eta_0$. This approximation is likely accurate only for materials that are nearly linear in behaviour (i.e. a and $b \approx 1$ in (4.33)). Values for a and b suggested by Boulton and Hindmarsh (1987) for (4.36), at 1.33 and 1.80, and (4.37), at 0.625 and 1.25, do not indicate a large degree of nonlinearity. Equation (4.61) would not be applicable to the highly-nonlinear behaviour suggested by Kamb (1991), for which $a \approx 100$. Combining (4.60) and (4.61) yields

$$M(t) = \frac{4\pi}{\ln(2c_{PL}/a_{PL}) + 0.5}\int_{Z_0}^{h_g}[h_g - Z]\, J(Z,t)\eta(Z,t)\Delta V(Z,t)\, dZ.$$ (4.63)

Calculation of the bending moment produced by motion through Coulomb-plastic till follows the analysis of both Humphrey and others (1993) and Fischer and Clarke

(1994). This is based on a relation derived by Hill (1956) for the indentation of a flat rigid punch into a semi-infinite plastic body under conditions of plane strain. At the onset of deformation, the pressure exerted on the punch by the plastic body is

$$\sigma = (2 + \pi)\sigma_Y, \tag{4.64}$$

where σ_Y is the yield strength of the medium (Hill, 1956, p. 356). An additional stress term must be introduced to account for the drag felt as the void is closed. Humphrey and others (1993) accounted for this additional stress by introducing a "negative indenter" that contributes a stress with equal magnitude to that for the intruding body. Approximating the ploughmeter as a flat indenter of width equivalent to the ploughmeter diameter, the total force per unit length acting upon a ploughmeter is thus

$$F'(Z, t) = 4a_{PL}(2 + \pi)\sigma_Y(Z, t), \tag{4.65}$$

with the yield stress σ_Y given by the Mohr-Coulomb failure criterion (4.34). Because the yield strength of Coulomb-plastic till is independent of the strain rate, the velocity contrast between the ploughmeter and till does not appear in 4.65. This relation holds even for zero velocity contrast, as once strained the ploughmeter is supported elastically by the till. The total moment acting upon a ploughmeter due to motion through a plastic body is given by combining (4.60) and (4.65):

$$M(t) = 4a_{PL}(2 + \pi) \int_{Z_0}^{h_g} [h_g - Z] J(Z, t) \sigma_Y(Z, t) \, dZ. \tag{4.66}$$

The behaviour of nonlinear-Bingham material is strongly dependent on the applied basal shear stress: at high basal shear stresses, Bingham till behaves as a nonlinear-viscous material, while at stresses below σ_Y elastic behaviour dominates. In the region of elastic behaviour, I assume that the force acting upon the ploughmeter is equivalent to that due to motion through a plastic material with the same yield strength. The

force per unit length at low values of shear stress is thus given by (4.65). In the region of viscous behaviour, the force per unit length is determined by (4.61). The relation used to calculate the force acting on a ploughmeter moving through a Bingham material therefore depends on the magnitude of the basal stress. Because $\dot{\varepsilon} \rightarrow 0$ as $\tau \rightarrow \sigma_Y$ for Bingham till, the effective viscosity approximation (4.62) blows up for shear stresses near σ_Y. For given values of a and σ_Y in (4.37), the minimum effective viscosity η_{min} occurs at $\sigma_{min} = \sigma_Y/(1-a)$. For shear stress values $\sigma_Y < \tau < \sigma_{min}$ (Fig. 4.4c, shaded region), till behaviour is neither truly elastic nor truly viscous, and the bending moment is taken to be the greater of (a) the moment due to viscous deformation, determined using η_{min} in (4.61), and (b) the moment calculated for a Coulomb-plastic material of the same yield strength σ_Y in (4.65).

Ploughmeter calibrations are typically performed by hanging objects of known weight from the device tip. As a result, calibrations and subsequent field records are expressed in units of force (kN) rather than bending moment (N m). I thus divide the modelled bending moment M by the tip-to-gauge-centre distance l_g to allow direct comparison with field records:

$$F = \frac{M}{l_g}.\qquad(4.67)$$

4.3 Summary

I have developed a simple hydromechanical model of the processes governing basal motion of a soft-bedded alpine glacier. In this model, the glacier bed is classified into three general regions, representing (1) soft-bedded regions that are hydraulically-connected to the subglacial drainage system, (2) soft-bedded but poorly connected regions and (3) hard-bedded regions. Each region is modelled as a single one-dimensional column, and the three regions are coupled by a simple ice-dynamics model. I have developed relations

to calculate the time-evolution of state variables $\tau_i(t)$, $n(Z,t)$, $p(Z,t)$, $s(Z,t)$ and $s_S(t)$ in each till column, subject to specified initial and boundary conditions. In the following chapter I will apply this model to the discrimination of proposed till flow laws.

Chapter 5

Application of the subglacial hydromechanical model to till flow law discrimination

5.1 Introduction

In this chapter I apply the coupled three-column hydromechanical model developed in Chapter 4 to the discrimination of proposed till flow laws. This is motivated by the critical role till flow characteristics play in determining the stability of ice sheets and glaciers that are underlain by soft sediments (Alley, 1990; Kamb, 1991). Initial and boundary conditions are chosen to mimic typical summer-mode conditions at Trapridge Glacier, Yukon Territory, Canada. I present modelled pore-water pressure and deformation profiles for linear-viscous, nonlinear-viscous, nonlinear-Bingham and Coulomb-plastic tills. I compare the magnitude and phase relationships of synthetic instrument responses for each flow law with *in situ* measurements of basal water pressure, pore-water pressure, sediment strain rate, basal sliding and sediment strength recorded at Trapridge Glacier. These comparisons allow determination of the flow law that provides the best qualitative match to observed variations in hydrological and mechanical conditions beneath Trapridge Glacier.

5.2 Field instrument records
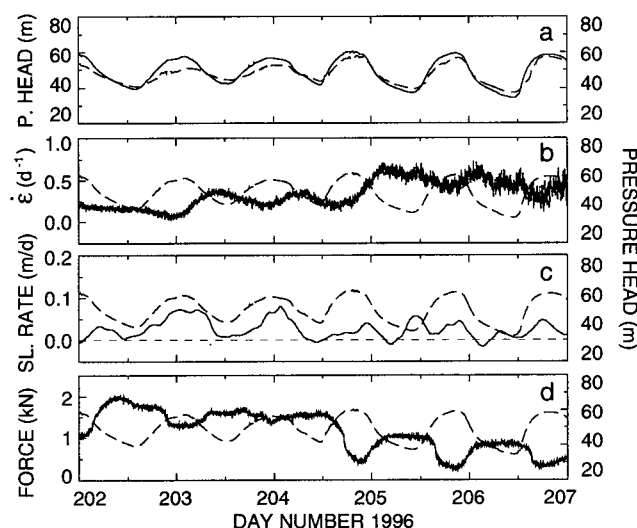
Figure 5.1: Field instrument records during 20–25 July (days 202–207) 1996. (a) Records for P1 (solid line) and PZ1 (dashed line). (b) Strain rate in till calculated from the tilt record for BT1 (solid line). (c) Sliding rate determined from displacement record for SL1. Short-dashed horizontal line represents zero sliding rate; negative values are discussed in the text. (d) Force record for PL1 (solid line). The dashed lines in (b–d) represent the pressure record for P1, shown for comparison.

Figure 5.1 shows simultaneous measurements of basal water pressure, pore-water pressure, sediment strain rate, basal sliding and sediment strength recorded by five instruments during the period 20–25 July 1996. The responses exhibit typical magnitudes and phase relations (with respect to diurnal water pressure fluctuations) for each instrument type during the summer season at Trapridge Glacier. These instruments were located within ∼7.0 m of each other (Fig. 5.2c), increasing the likelihood that similar basal conditions and forcings were acting on each instrument. The five instruments were installed in a total of three boreholes, with sensors P1 and PL1 sharing one hole and PZ1 and BT1 sharing another. Water level fluctuations in each borehole immediately following

the completion of drilling indicates that all three boreholes were placed in hydraulically-connected regions of the bed.

The extreme pressure pulses discussed in Chapter 2 occurred at 2120 h on day 202 (20 July) of 1996. The pulses thus occurred during the first day of the records presented in Figure 5.1. As seen in Figure 1.2, the instruments shown in Figure 5.1 are located within the region affected by the pressure pulses. None of the records shown in Figure 5.1 exhibits any response at this time. Pressure transducer P1 in this chapter is the same sensor as transducer P1 in Chapter 2; no reflection of the pulses is seen in this pressure record. As discussed in Chapter 2, no response was observed in any tilt cell, slidometer or ploughmeter record at the time of the event, indicating no significant local mechanical response occurred at the time of the pressure pulses.
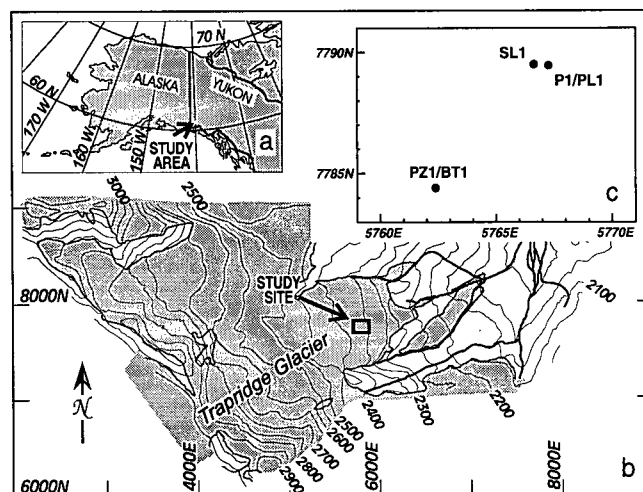
Figure 5.2: Study area. (a) Location map, southwestern Yukon Territory, Canada. (b) Trapridge Glacier, showing location of instrument study. (c) Study site.

Figure 5.1a shows records for pressure transducers P1 and PZ1 during the period 20–25 July (day numbers 202–205) 1996. Pressure transducer PZ1 was installed at a depth of

approximately 0.15 m within the subglacial till and is taken to represent the pore-water pressure within the sediments at this depth. The records for both P1 and PZ1 show strong diurnal pressure fluctuations, indicating continued hydraulic connection with the subglacial drainage system. The record for transducer P1 exhibits peak pressures of 56.7–60.5 m and minimum pressures ranging between 34.3 and 42.3 m. Sensor PZ1, which is installed approximately 0.15 m into the subglacial sediments, exhibits pressure variations that are slightly lower in amplitude and lagged in phase with respect to those indicated in the record for P1.

Figure 5.1b shows the strain rate in the subglacial sediments inferred from the tilt record for tilt cell BT1. The tilt cell, which measures 0.11 m long and incorporates pressure transducer PZ1 (Fig. 5.1a), was installed ∼0.15 into the sediments. During the five-day period shown in Figure 5.1, the tilt sensor rotated approximately 14.7° (assumed down-glacier), from 63.5° to 78.2°. The tilt angle time-series data were smoothed with a 3-hour moving-boxcar filter prior to differentiation. Strain rate variations are out-of-phase with water pressure fluctuations, exhibiting peak daily strain rates of 0.29–0.51 d^{-1} (110–190 a^{-1}) and minima of 0.03–0.30 d^{-1} (11–110 a^{-1}).

Figure 5.1c shows inferred glacier sliding rates from the record for slidometer SL1. The anchor was hammered ∼0.12 m into the subglacial till. Prior to differentiation, raw sliding displacement data were smoothed with a 3-hour moving boxcar filter. Peak sliding rates during the period reach 0.08 m d^{-1}. The slightly negative sliding rates indicated in the record are clearly non-physical and are likely artifacts of the instrument design. Possible sources for these errors include potentiometer noise, elastic relaxation of the grease used to waterproof the device or gradual water infiltration. Strong correlation between sliding rate and subglacial water pressure are observed during days 202–204, sliding rates during days 205–206 are not as clearly related to pressure variations.

Ploughmeter PL1 (Fig. 5.1d) was installed in the same borehole as pressure transducer P1 (Fig. 5.1a). Upon installation, the tip of PL1 was inserted approximately 0.14 m into the till. Measured forces range between 0.28 and 2.0 kPa, and exhibit diurnal variations that are out-of-phase with water pressure fluctuations: low force values occur during times of high water pressure; high forces coincide with times of low pressure.

5.2.1 Model parameters

Table 5.1 shows values for physical constants used in the model. Is this table and the tables that follow, parameter values are shown to the same precision as used in the model runs.

Table 5.1: Physical constants used in the Trapridge Glacier model.

Constant	Value	Description
g	$9.81 \, \text{m s}^{-2}$	Gravitational acceleration
ρ_w	$1000.0 \, \text{kg m}^{-3}$	Density of water
β	$5.10 \times 10^{-10} \, \text{Pa}^{-1}$	Compressibility of water
μ_w	$1.787 \times 10^{-3} \, \text{Pa s}$	Viscosity of water

Table 5.2 shows assumed values for the ice-dynamics model. Although the basal ice at Trapridge Glacier is at the melting point, the bulk of the ice is at sub-freezing temperatures and is therefore stiffer; it is this stiffer ice that largely determines the flow characteristics of the ice. The parameter values shown here are appropriate for glacier ice at $-5°C$. The rigidity modulus $G_I = 3.50 \times 10^9 \, \text{Pa}$ represents an average of values determined for ice at this temperature by Ewing and others (1934), Northwood (1947), Jona and Scherrer (1952) and Gold (1958) using sonic techniques. The value $A_0 = 1.6 \times 10^{-15} \, \text{s}^{-1}(\text{kPa})^{-3}$ for Glen flow is that suggested by Paterson (1994, p. 97) for ice at $-5°C$ and $N = 3$. The value of A_0 varies strongly with temperature and thus

plays a large role in determining the flow characteristics of ice. In the ice-dynamics model developed in Chapter 4, it is the quantity $A_0 L$, where L is the characteristic lengthscale between columns, that determines ice behaviour. This is most clearly seen in Equation (4.54). I will thus consider A_0 fixed and take L as the adjustable parameter.

Table 5.2: Assumed ice properties for the Trapridge Glacier model.

Parameter	Value	Description
ρ_I	$917.0\,\mathrm{kg\,m}^{-3}$	Density of ice
G_I	3.5×10^9	Rigidity modulus of ice
A_0	$1.6 \times 10^{-15}\,(\mathrm{kPa})^{-3}\mathrm{s}^{-1}$	Glen flow parameter
N	3.00	Glen flow exponent

The geotechnical properties of Trapridge Glacier till are not currently well known. Size-distribution analysis of a sample of recently-exposed basal till from Trapridge Glacier showed that fine-grained solids (silt- and clay-sized particles) account for roughly 40% of the solid volume (Clarke, 1987b). High clay content is also suggested for Trapridge Glacier till by the thick slurry of fine sediments that commonly coats the insertion hammer tip following instrument installation. Other quantities, such as the *in situ* porosity, compressibility, permeability and shear strength, are poorly constrained for Trapridge Glacier till. I take parameter values pertaining to these properties from previous instrument studies at Trapridge Glacier or from geotechnical tests of tills obtained from other locations. When taking parameter values from other studies, I use the value presented to its full precision; in cases where a range of values is presented, I take a mid-ranged value.

Table 5.3 shows assumed till properties used in the model. These parameters determine the hydraulic permeability and dilatant properties of the till and govern how these properties vary in response to modelled fluctuations in drainage system pressures.

The value chosen for the sediment density ρ_s is likely slightly high; values of 2700–2800 kg m^{-3} are probably more representative of the mix of metamorphic and igneous materials found beneath Trapridge Glacier. Values used for the compression and swelling indices $B_c = 32.9$ and $B_s = 164.0$ are those determined by Clarke (1987b) based on studies of Glasgow till (McKinlay and others, 1978, Table 3). Reference values for normal consolidation void ratio are taken to be $e_0 = 0.266$ at $p'_0 = 500$ kPa and $e_1 = 0.389$ at 0 kPa; the critical-state reference void ratio is taken as $e_{CS} = 0.250$. These values are slightly lower than those used by Clarke (1987b) and are likely more representative of Trapridge till, yielding initial porosities of $0.21 \leq n \leq 0.28$ for the range of effective pressures encountered beneath Trapridge Glacier. Assuming a surface-to-volume ratio of $S_0 = 5.0 \times 10^6$ m^{-1} (corresponding to a clay-sized particle with grain diameter 1.2 μm) results in hydraulic permeabilities of $k = 1.19$–3.39×10^{-16} m^2, reasonable values for till. The rate of dilatant till expansion or contraction is determined by the scaling factor $A_{CR} = 0.20$; this value results in a time constant of $\dot{\varepsilon}/5$.

Table 5.3: Assumed till properties for the Trapridge Glacier model.

Parameter	*Value*	*Description*
ρ_s	3000.0 kg m^{-3}	Density of sediment
S_0	5.00×10^6 m^{-1}	Surface-to-volume ratio of sediments
e_0	0.266	Reference value void ratio for NCL
p'_0	500.0 kPa	Reference value of effective pressure
e_1	0.389	Zero effective pressure void ratio
e_0^t	0.250	Reference value of void ratio for CSL
B_c	32.9	Compression index
B_s	164.0	Swelling index
D_0	0.20	Dilatant response scaling factor

Table 5.4 shows the assumed parameter values for the four modelled till flow laws. The viscosity chosen for the linear-viscous flow law is taken from earlier instrument studies

performed at Trapridge Glacier. Blake (1992) estimated an effective viscosity of $\eta_0 = 2.0 \times 10^{10}$ Pa s based on deformation rates calculated from tilt cell records. Fischer and Clarke (1994) used ploughmeter records to estimate effective viscosities ranging between 3.0×10^9 Pa s and 3.1×10^{10} Pa s. This range brackets the value suggested by Blake (1992). Based on these studies, I assume a linear viscosity of $\eta_0 = 2.0 \times 10^{10}$ Pa s. For the nonlinear-viscous and nonlinear-Bingham flow laws I adopt the values for a and b in (4.36) and (4.37) proposed by Boulton and Hindmarsh (1987). These values are given to an unreasonable degree of certainty: for the nonlinear-viscous till, $a = 1.33$ and $b = 1.80$; for the nonlinear-Bingham till the values given are $a = 0.625$ and $b = 1.25$. I choose to retain the full precision of these values (rather than, for instance, rounding these exponents to the nearest integer value) in order to model the behaviours proposed by the authors. The value I have chosen for flow constant B_0 in (4.36) a factor of ~ 30 greater than the value proposed by Boulton and Hindmarsh. This increase was made in order to produce modelled till deformation rates closer to those measured beneath Trapridge Glacier. To model nonlinear-Bingham till deformation, I use the value for flow constant B_1 in (4.37) suggested by Boulton and Hindmarsh (1987).

Both nonlinear-Bingham and Coulomb-plastic tills deform only at shear stresses greater than a yield stress determined by the Mohr-Coulomb failure criterion. The shear strength of Trapridge Glacier till has not been measured in the laboratory. I take values for $c_0 = 0$ and $\phi = 18.6°$ measured for a clay-rich till by Iverson and others (1998). Although clay-rich materials often exhibit marked cohesion, cohesion is expected to be negligible for tills that are in a residual state (Lambe and Whitman, 1979). In modelling Coulomb-plastic materials, adopting these values for the Mohr-Coulomb failure criterion result in yield strengths ranging 14–80 kPa for the modelled effective pressures. Fischer and Clarke (1995) have estimated the yield strength of Trapridge Glacier till to be 48–57 kPa based on ploughmeter records at Trapridge Glacier. This yield strength estimate

is based on values measured by one ploughmeter during a period of relatively constant force values. The range of yield strengths suggested by other ploughmeter records, and indeed by the full range of force values in the same record, is greater.

Shear failure of an ideal plastic material would be localized to an infinitely thin layer. However, because till is composed of particles with sizes ranging from clays (diameter $<1\,\mu$m) to boulders (diameter >1 m), till deformation will be distributed over a layer with finite thickness. The values I have chosen for the reference strain rate $\dot{\varepsilon}_0 = 1.0 \times 10^5\,\mathrm{s}^{-1}$ and failure range $\Delta\tau = 5.0\,\mathrm{kPa}$ in (4.39) result in deformation that is distributed over a layer 0.1–0.2 m thick, comparable in scale to the diameter of the largest commonly-occurring clasts.

Clearly, model results are strongly influenced by the choice of till flow law parameters. I discuss the effects of varying the flow law parameters in a section 5.3.2.

Table 5.4: Assumed till flow law parameters for the Trapridge Glacier model.

Parameter	Value	Description
Linear-viscous till:		
η_0	2.0×10^{10} Pa s	Till viscosity
Nonlinear-viscous till:		
B_1	$1.0 \times 10^3 \, (\text{kPa})^{0.47} \text{a}^{-1}$	Flow parameter
a	1.33	Shear stress exponent
b	1.80	Effective pressure exponent
Mohr-Coulomb failure criterion parameters:		
c_0	0.00	Residual cohesion constant
ϕ	18.6°	Residual friction angle
Nonlinear-Bingham till:		
B_2	$121.0 \, (\text{kPa})^{0.625} \text{a}^{-1}$	Flow parameter
a	0.625	Shear stress exponent
b	1.25	Effective pressure exponent
Coulomb-plastic till:		
$\dot{\varepsilon}_0$	$1.0 \times 10^{-4} \, \text{s}^{-1}$	Reference strain rate
$\Delta\tau$	5.0 kPa	Failure range

5.2.2 Boundary conditions and initial conditions

Table 5.5 lists values prescribed to boundary and initial conditions for the models presented. The main "tuning" parameters in the model include the basal pressure p_B, till layer thickness h, hard- and soft-bedded variational scales L_H and L_S used in equation 4.54 to determine shear stress transfer, areal fractions α_i, and glacier sliding reference pressure p_{SL}. The effects of varying these key parameters are discussed in section 5.3.3.

Values for ice thickness $H = 70.0$ m and surface slope $\theta = 7.0°$ were chosen to represent the geometry of Trapridge Glacier, and the thickness of the deformable till layer is assumed to be 1.0 m. Appropriate values for areal fractions α_1, α_2 and α_3 have not been established. In the study area, attempts to install instruments in the bed are usually successful. In rare cases when installation in a particular borehole is difficult, drilling

Table 5.5: Model parameters for response tests.

Parameter	Value	Description
Model geometry:		
θ	7.00°	Ice surface slope
H	70.0 m	Thickness of ice
h	1.0 m	Thickness of till layer
Areal fractions:		
α_1	0.20	Areal fraction of connected region
α_2	0.60	Areal fraction of unconnected region
α_3	0.20	Areal fraction of hard-bedded region
Length scales of basal variation:		
L_H	1500.0 m	Hard-bedded and soft-bedded variational scale
L_S	150.0 m	Soft-bedded variational scale
Glacier sliding parameters:		
p_{SL}	698.5 kPa	Reference pressure for glacier sliding
Δp_{SL}	629.1 kPa	Pressure range for glacier sliding
h_{SL}	0.01 m	Thickness of lubricating layer
μ_{SL}	2.0×10^7 Pa s	Viscosity of lubricating layer
Connected region water pressure:		
p_{T1}	490.0 kPa	Mean water pressure at $Z = H$
$p_{\Delta T1}$	98.0 kPa	Amplitude of diurnal pressure variation
p_{B1}	294.0	Water pressure at $z = 0$
Unconnected region water pressure:		
p_{T2}	588.0 kPa	Mean water pressure at $Z = H$
p_{B2}	294.0	Water pressure at $z = 0$

a second hole a metre or so away usually provides a suitable site. This suggests that installation difficulties are caused by large clasts rather than by hard-bedded spots and that study area is largely soft-bedded. Crevasse patterns in the vicinity of the study area suggest that resistance to flow could be provided mainly by marginal drag. Further down-glacier, two ridges with generally along-flow trends restrict glacier flow. These ridges give Trapridge Glacier its triple-lobed terminus (e.g., Fig. 1.1b), as ice flowing between these

ridges bulges beyond the slower-moving ice pinned to the ridges. I make the rough assumptions that (1) hydraulic connection occurs in ~25% of soft-bedded regions and (2) hard-bedded and hydraulically-connected regions cover approximately equal portions of the bed. These assumptions give nominal values $\alpha_1 = 0.20$, $\alpha_2 = 0.60$ and $\alpha_3 = 0.20$.

Water pressure values are prescribed at the ice–bed interface in the two soft-bedded columns. In order to model general summer behaviours at Trapridge Glacier, I choose pressure forcing functions for columns 1 and 2 that mimic typical summer-mode pressure records in connected and unconnected regions, respectively. Hydraulic connection in column 1 is simulated by assigning a sinusoidally-varying pressure function to the top of the till column:

$$p_1(h, t) = p_{T1} + p_{\Delta T1} \cos(\omega t). \tag{5.1}$$

The pressure $p_1(h, t)$ thus represents the drainage system pressure. Taking $p_{T1} = 490.0\,\text{kPa}$, $p_{\Delta T1} = 98.0\,\text{kPa}$ $\omega = 2\pi\,\text{d}^{-1}$ yields diurnally-varying pressures ranging between 40.0 and 60.0 m of head, similar to the record for P1 (Fig. 5.1a). Unconnected regions generally exhibit steady, near-flotation pressure values; water pressure at the top of column 2 is thus given by

$$p_2(h, t) = p_{T2} \tag{5.2}$$

with $p_{T2} = 588.0\,\text{kPa}$ ($h = 60.0\,\text{m}$).

Pore-water pressure at the base of each till layer is held at a constant value:

$$p_1(0, t) = p_B 1 \tag{5.3}$$

$$p_2(0, t) = p_B 2. \tag{5.4}$$

For the modelling scenarios presented here, $p_B 1 = p_B 2$. It is unclear what value p_B should take. If the region beneath the till layer is relatively impermeable, p_B would likely reflect

an average value of the ice–bed-interface pressure. If the till layer is underlain by a highly-permeable aquifer, p_B may vary from this value depending upon the aquifer pressure. I select a nominal pore-water pressure of $p_B = 294.0\,\text{kPa}$ ($h = 30.0\,\text{kPa}$); the effects of varying p_B will be discussed in a later section. The initial pore-water pressure profile within the till layer is assumed to vary linearly with depth:

$$p_1(Z,0) = p_B + (p_{T1} - p_B 1)(H - Z)/H \qquad (5.5)$$

$$p_2(Z,0) = p_B + (p_{T2} - p_B 2)(H - Z)/H. \qquad (5.6)$$

Void ratios are initialized to the critical state value (4.11) given the assumed pressure profiles:

$$e_1(Z,0) = e_{CS}(p_I - p_1(Z,0)) \qquad (5.7)$$

$$e_2(Z,0) = e_{CS}(p_I - p_2(Z,0)). \qquad (5.8)$$

In the majority of the modelling scenarios presented here, I assume that the volume of free water in the hydraulically-unconnected regions is insufficient to submerge roughness elements of the glacier bed to the degree necessary to permit glacier sliding. With this assumption, glacier sliding is allowed only in the hydraulically-connected regions of the bed even though modelled water pressures in the hydraulically-unconnected region are near flotation. This assumption is clearly open to debate, and in reality the degree of sliding is likely to be highly variable over the glacier bed in both connected and unconnected regions. Here I have made this assumption primarily to prevent pervasive ice–bed decoupling, as such a configuration is likely to be highly unstable. Restricting basal motion in unconnected regions to sediment deformation results in greater overall stability. This assumption can therefore be thought of as providing the most stable

glacier configuration for the given modelled till properties. I discuss relaxation of this assumption in Section 5.3.3.

The sliding parameters in (4.44) assigned to column 1, at $p_{SL} = 698.5 \, \text{kPa}$ and $\Delta p_{SL} = 629.1 \, \text{kPa} (= p_I)$, result in 20% decoupling at flotation ($p = p_I$) and 7% decoupling at $p = 0.90 \, p_I$. This value of p_{SL} was chosen to yield sliding velocities similar to those recorded by SL1 (Fig. 5.1); the effects of varying this parameter are discussed in section 5.3.3. I assume that the lubricating slurry has viscosity $\eta_{SL} = 2.0 \times 10^7 \, \text{Pa s}$ (0.1% of the linear till viscosity) and a layer thickness of 0.01 m.

In Nature, glacier motion in hard-bedded regions is likely due to some combination of creep flow, ice fracture and basal sliding. The simple ice-dynamics model employed in this study considers only ice creep in the region *between* individual columns and ignores the component of flow resulting from deformation of the ice above the columns. With the additional assumption that no sliding occurs in hard-bedded regions, these regions are assumed static and provide necessary resistance to glacier flow. Indeed, without the pinning points provided by the hard-bedded regions, the modelled glacier would accelerate unchecked. I choose the value $L_H = 1500 \, \text{m}$ for the length scale of variation between hard- and soft-bedded regions to give flow rates comparable to those observed at Trapridge Glacier during the summer field season ($\sim 0.07\text{--}0.12 \, \text{m d}^{-1}$). This value is unrealistic, as it exceeds the glacier width at the elevation of the study area, but accounts for the contributions to ice motion made by the mechanisms of enhanced creep, regelation and crevassing not directly incorporated into the ice-dynamics model. Making the rough assumption that the variational length scale between soft-bedded regions $L_S \approx L_H/10$ yields $L_S = 150.0 \, \text{m}$. I shall discuss the effects of varying L_H and L_S in a later section.

Evolution of the state variables $\tau_i(t)$, $n(Z,t)$, $p(Z,t)$, $s(Z,t)$ and $s_{SL}(t)$ is calculated in each till column by numerically integrating equations (4.53), (4.14), (4.32), (4.42) and (4.45), respectively, subject to the specified initial and boundary conditions.

5.3 Modelling results

Figures 5.3a–d show modelled pore-water pressure profiles in the connected region at 0.125 d intervals. Water pressure variations at the ice–bed interface in this region drive all other model responses. In the following discussions, I will refer to this pressure as the modelled drainage system pressure. Pore-water pressures at the time of maximum system pressure are shown in Figure 5.3a (solid line). Pressures in the till layer vary between 30.0 and 60.0 m at this time. Figures 5.3a, b show profiles during times of decreasing system pressure, while Figures 5.3c, d show pressures increasing from the daily minimum of 40.0 m. The diurnal pressure signal diffuses into the till layer to a depth of ∼0.5 m. Figure 5.3e shows the pressure profile for the unconnected region. The flotation pressure of 64.2 m is indicated in the shaded region above $Z = 1.0$ m in each plot.

The dilatant response to diurnal pressure fluctuations result in variations in till column thickness of 1.6 mm for all flow laws. This small response is due in part to the fact that void ratios were assumed to be initially at the critical state value e_{CS} throughout the till column. If the till were initialized to an significantly overconsolidated state, a large initial dilatant response would be noted as till deformation would drive the void ratio towards the critical value (as determined by Eq. (4.12)). The resulting increase in pore volume would lead to decreased pore-water pressures within the sediments and thus stiffening the till. Such "dilatancy hardening" could provide increased resistance to basal motion. Following sufficient deformation of the till, the void ratio would reach the critical value and the dilatant response would be similar to that observed here. When the void ratio of till is near the critical-state value, the dilatant properties of till likely play only a small role in determining its behaviour. In contrast, dilatant properties may significantly affect till behaviour in situations where the void ratio differs substantially from the critical-state value. Thus while the modelling results presented here show only
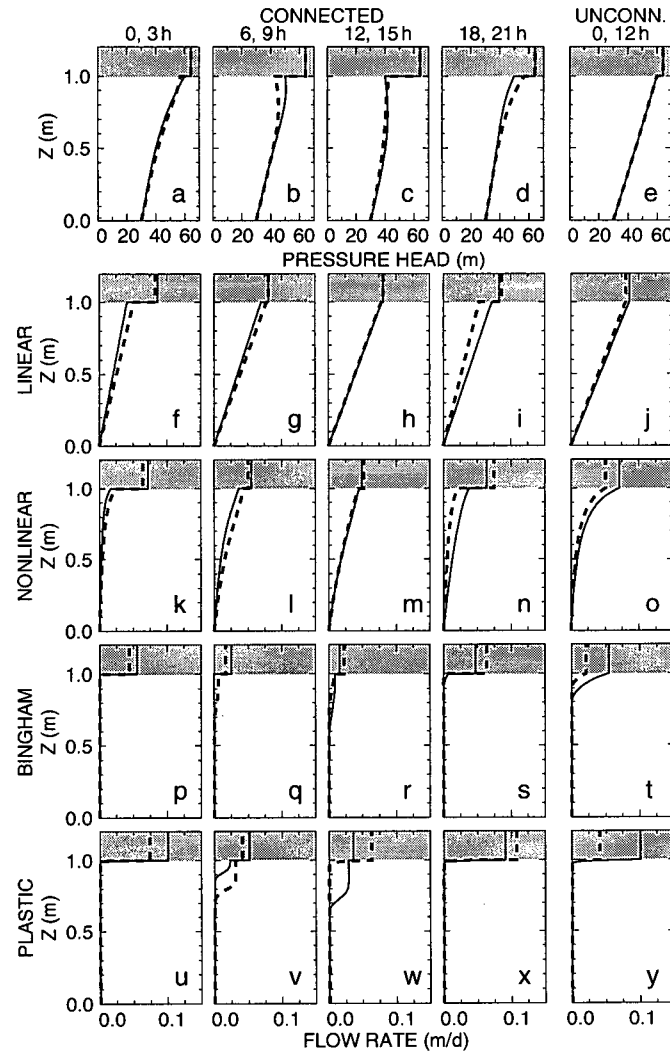
Figure 5.3: Modelled pore-water pressure and deformation profiles. (a–d) Modelled pore-water pressure profiles in the connected region. Pressure value in shaded region above $Z = 1.0\,m$ represents the flotation pressure. (a) Profiles at $t = 0$, corresponding to peak system pressure (solid line), and $t = 0.125$ d (dashed line). (b) Profiles at $t = 0.250$ d (solid line) and $t = 0.375$ d (dashed line). (c) Profiles at $t = 0.500$ d (minimum system pressure; solid line) and $t = 0.375$ d (dashed line). (d) Profiles at $t = 0.750$ d (solid line) and $t = 0.875$ d (dashed line). (e) Modelled pressure profile in unconnected region. for times of maximum (solid line) and minimum (dashed line) system pressure. (f–y) Modelled till deformation profiles. Total ice velocity is shown in shaded region above $Z = 1.0$ m. (f–i) Connected-region deformation profiles for linear-viscous till at times corresponding to pressure profiles in (a–d). (j) Deformation profiles in unconnected region at times of maximum (solid line) and minimum (dashed line) system pressure modelled for linear-viscous till. (k–o) Deformation profiles for nonlinear-viscous till; times and connection status correspond to (a–e). (p–t) Deformation profiles for nonlinear-Bingham till. (u–y) Deformation profiles for Coulomb-plastic till.

minor dilatant responses, their inclusion could prove important in modelling such scenarios as the onset of deformation in a highly-overconsolidated till. For this reason, I believe it is essential to retail the Lagrangian representation of till despite the minor dilatant response associated with the above model experiments.

Modelled till deformation profiles are shown in Figures 5.3f–y. Each row corresponds to a different till flow law: Figures 5.3f–j represent linear-viscous deformation; Figures 5.3k–o show nonlinear-viscous flow; Figures 5.3p–t and 5.3u–y represent nonlinear-Bingham and Coulomb-plastic deformation, respectively. The first four plots in each row represent deformation profiles in the hydraulically-connected region at times corresponding to those for pressure profiles presented in Figures 5.3a–d. The final plot in each row presents deformation profiles in the hydraulically-unconnected region at maximum (solid line) and minimum (dashed line) connected-region pressure. The ice flow rate V is shown in the shaded region above $Z = 1.0$ in each plot.

Linear-viscous till (Fig. 5.3f–j) exhibits uniform deformation over the full thickness of the till layer. In the connected region, ice–bed decoupling during times of high modelled system pressure (e.g., Fig. 5.3f) results in reduced shear traction acting upon the bed, decreasing deformation rates and increasing glacier sliding. At peak modelled pressure, bed deformation accounts for 48% of the 0.086 m/d flow rate. At low system pressures, ice–bed coupling is strong, with bed deformation accounting for 98% of the 0.082 m/d ice velocity at minimum diurnal pressure (Fig. 5.3h). Maximum and minimum flow rates in the unconnected region (Fig. 5.3j), at 0.086 and 0.081 m/d, closely match those for the connected region.

Deformation profiles for nonlinear-viscous till (Fig. 5.3k–o) also exhibit deformation over the full till thickness. During times of high modelled system pressure, deformation is concentrated near the top of the till layer as high pore-water pressures soften the till. The nearly-linear pressure profile at day 4.625 (Fig. 5.3c, dashed line) results in

uniform deformation over the depth of the till layer (Fig. 5.3m, dashed line). At peak system pressure, bed deformation accounts for 24% of the 0.072 m/d ice velocity. The ice velocity decreases to 0.049 m/d at minimum system pressure, 91% of which is due to bed deformation. In the unconnected region (Fig. 5.3o), ice velocities are 0.071 and 0.051 m/d at maximum and minimum system pressures, respectively. Because till characteristics in the unconnected region do not vary over time, increased flow velocities during high modelled system pressures are the result of additional shear stress transferred from the connected region.

Profiles for nonlinear-Bingham till (Fig. 5.3p–t) exhibit deformation that is confined to the top ~0.4 m of the till layer. At any given time, deformation occurs only over the depth range in which the Mohr-Coulomb yield stress is lower than the applied shear traction. At times of high modelled system pressure, ice–bed decoupling reduces the shear stress transmitted to the bed. At peak system pressure (Fig. 5.3q, solid line) sliding accounts for all of the 0.064 m/d ice flow rate; at minimum system pressure (Fig. 5.3r, solid line) deformation contributes 0.009 m/d of the 0.016 m/d total ice velocity. Deformation in the unconnected region (Fig. 5.3t) occurs in the top 0.20 m at peak modelled system pressure, at which time the ice flow rate is 0.055 m/d. At minimum system pressure the flow rate decreases to 0.021 m/d, with deformation occurring in the top 0.09 m of till. Because pore-water pressures decrease with depth in the till layer, till strength increases with depth. Deformation in the unconnected region occurs to the depth at which the Mohr-Coulomb yield strength is greater than the applied shear stress. The additional shear stress transferred from the connected region during times of high system pressures results in till deformation to greater depths.

Modelled deformation of Coulomb-plastic till (Fig. 5.3u–y) occurs over localized regions ranging in thickness from 0.01 m at maximum system pressure to 0.24 m at minimum system pressure. These variations in deforming-layer thickness result from our

treatment of plastic deformation, in which failure is assumed to occur over some stress range $\Delta\tau$ in (4.39). Because the yield stress varies with pore-water pressure, steep pressure gradients in the till (as seen at maximum pressure, Fig. 5.3a, solid line) result in an abrupt transition between deforming and non-deforming states, with deformation confined to the upper 0.01 m of till. Lower pressure gradients, as seen at the time of minimum system pressure (Fig. 5.3c, solid line), yield a more gradual transition.

Because till strength is determined by effective pressure, deformation occurs where pore-water pressures are greatest in the till column (compare, for example, Fig. 5.3b and v;). This behaviour can result in rapid changes in the depth of active deformation. At the time of minimum system pressure, the deforming region is centred at $Z = 0.73$ m (Fig. 5.3w, solid line). This location corresponds to the depth of maximum pore-water pressure within the till layer (Fig. 5.3c, solid line). Three hours later, the water pressure at the ice–bed boundary has surpassed the pore-water pressures deeper in the till layer (Fig. 5.3w, dashed line), resulting in deformation immediately at the glacier sole.

For Coulomb-plastic till, deformation accounts for 36% of the 0.101 m/d ice velocity at peak system pressure and 81% of the 0.035 m/d flow rate at minimum system pressure. Deformation occurs to a depth of 0.45 m in the connected region. Modelled deformation in the hydraulically-unconnected region is confined to the upper 0.01 m of the till layer (Fig. 5.3y). Modelled deformation rates in the unconnected region range from 0.041 m/d at minimum system pressure to 0.101 m/d at peak pressure.

Figure 5.4 shows total daily sediment deformation in the connected (Fig. 5.4a–d) and unconnected (Fig. 5.4e–h) regions for each of the four till flow laws. In all cases the total deformation is greater in the unconnected region because (1) glacier sliding accounts for a portion of glacier motion in the connected region and (2) for nonlinear flow laws, stiffening of till in the connected region during times of low system pressure reduces the deformation rate there. Linear-viscous till (Fig. 5.4a, e) exhibits uniform
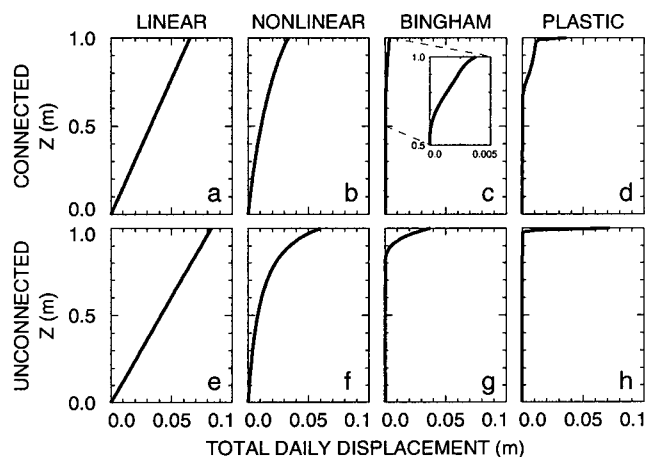
Figure 5.4: Total till displacement profiles for one model day. (a–d) Modelled displacements for connected region. (e–h) Modelled displacements for unconnected region. Profiles (a,e) correspond to linear-viscous till, (b,f) to nonlinear-viscous till, (c,g) to nonlinear-Bingham till and (d,h) to Coulomb-plastic till.

deformation over the full till layer. Deformation is increasingly concentrated at the ice–bed interface as the degree of till flow-law nonlinearity increases. This is most evident in the unconnected region: for nonlinear viscous till, 69% of deformation occurs in the top 0.25 m of the till layer, whereas deformation of nonlinear-Bingham and Coulomb-plastic tills is limited to the top 0.20 m and 0.03 m, respectively. Deformation of nonlinear-Bingham and Coulomb-plastic tills extends to greater depths in the connected region (Fig. 5.4c, inset; 12d) due to diffusion of pressure variations, reaching depths of 0.41 and 0.32 m.

Figure 5.5 shows modelled five-day records of basal shear stress in each region for the four till flow laws. Shear traction is expressed in terms of the nominal shear stress $\tau_0 = \rho_I g H \sin\theta$, and the modelled drainage system pressure is shown for reference. All four plots show that shear stress is predominantly concentrated on the hard-bedded region, which supports an average of $3.75\,\tau_0$. Also evident in all four cases is the system-pressure
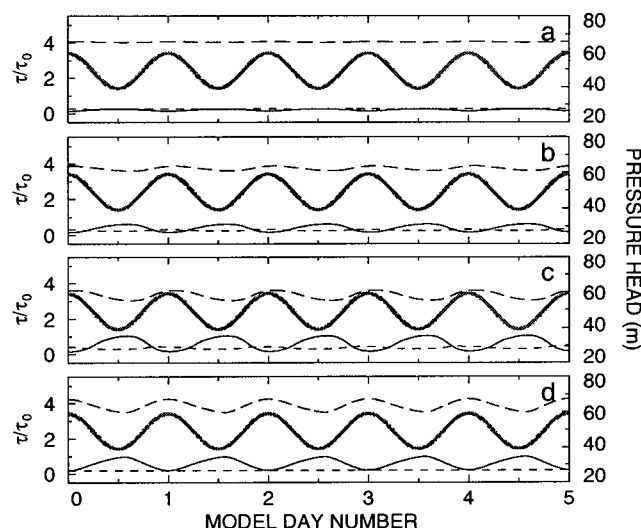
Figure 5.5: Modelled five-day basal shear stress for connected (solid lines), unconnected (short dashes) and hard-bedded (long dashes) regions. Modelled drainage system pressure (thick grey line) shown for comparison. (a) Basal shear stresses for linear-viscous till. (b) Shear stresses for nonlinear-viscous till. (c) Basal shear stresses for nonlinear-Bingham till. (d) Shear stresses for Coulomb-plastic till.

driven transfer of shear stress between regions. During times of high pressure, stress is transferred from the connected region to the unconnected and hard-bedded regions by enhanced deformation and glacier sliding. Drainage system pressure and connected-region shear-stress signals are thus out-of-phase, while stresses in the unconnected and hard-bedded regions show nearly in-phase responses to drainage system pressure changes.

Table 5.6 lists the minimum and maximum modelled shear stress supported in each region. The modelled shear stress supported by the connected region displays an out-of-phase relationship with those supported by the unconnected and hard-bedded regions (Fig 5.5). for this region, the maximum shear stress supported by the connected region in Table 5.6 corresponds to the minimum shear stress in the other two regions. The shear stress supported by connected regions at maximum system pressure range between

Table 5.6: Modelled basal shear stresses.

Flow Law	Minimum Shear Stress	Maximum Shear Stress
Linear-viscous till:		
Connected region	$0.14\,\tau_0$	$0.24\,\tau_0$
Unconnected region	0.24	0.26
Hard-bedded region	4.03	4.08
Nonlinear-viscous till:		
Connected region	0.16	0.63
Unconnected region	0.25	0.32
Hard-bedded region	3.61	3.87
Nonlinear-Bingham till:		
Connected region	0.17	1.05
Unconnected region	0.30	0.42
Hard-bedded region	3.04	3.58
Coulomb-plastic till:		
Connected region	0.18	0.98
Unconnected region	0.18	0.18
Hard-bedded region	3.49	4.25

14–18% of the nominal driving stress τ_0; at minimum system pressure the connected region supports 24–105% of the driving stress. Only 18–42% of the driving stress is supported by the unconnected region. Hard-bedded regions provide the majority of resistance to ice motion for all flow laws, as implicit in the model assumptions. These values are similar to estimates of basal stress for Ice Stream B by Kamb (1991) and Tulaczyk and others (2000c), which suggest that basal drag accounts for ∼10–50% of the total flow resistance; the remaining support is provided by the ice stream margins (Echelmeyer and others, 1994; Jackson and Kamb, 1998; Raymond, 1996; van der Veen and Whillans, 1996; Whillans and van der Veen, 1997) and localized sticky spots (Alley, 1993; Anandakrishnan and Alley, 1994).

Linear-viscous till (Fig. 5.5a) shows only minor redistribution of basal stresses with

variations in drainage system pressure. Because the deformation rate given by this flow law is independent of pore-water pressure, till stiffness in the connected region does not vary with changing system pressures. Ice–bed decoupling at high system pressures results in the transfer of shear stress to the unconnected region. Little sliding occurs at low system pressure, and thus both soft-bedded regions support similar shear stresses at these times. Nonlinear-viscous and Bingham tills (Fig. 5.5b and c) exhibit more pronounced changes in stress distribution. This is due to stiffening of till in the connected region during times of low system pressure, which results in the transfer of shear stress onto the connected region.

For Coulomb-plastic till (Fig. 5.5d), system pressure variations cause cyclic stress transfer between the connected and hard-bedded regions, while the stress supported by the unconnected region remains constant. Because the till fails instantaneously at the Coulomb yield stress determined by (4.34), the shear traction supported by a given soft-bedded region does not exceed the strength of the weakest portion of the till layer. The supported stress is therefore determined by the maximum pore-water pressure within the till column. In the unconnected region, the pressure profile remains constant, and thus so does the supported shear stress.

Linear-viscous, nonlinear-viscous and Bingham tills exhibit maximum shear stress in the hard-bedded region at times 60, 90 and 106 min following peak system pressure (Fig. 5.5a–c). For Coulomb-plastic till, this lag is 8 min (Fig. 5.5d). The greater lag observed for viscous tills indicates that the rate of shear-stress transfer is controlled largely by the deformation rate in the unconnected region. Because plastic till provides no additional resistance to flow at greater velocities, the rate of stress transfer is instead determined by the visco-elastic properties of the glacier ice.

5.3.1 Modelled instrument responses

In the following discussions I compare the field instrument records (Fig. 5.1) to modelled instrument records for each of the four till flow laws. Because the field instruments included in this study were located in connected regions of the glacier bed, discussion will be limited to instrument responses calculated for the connected region. No field instrument records representative of unconnected regions are available.
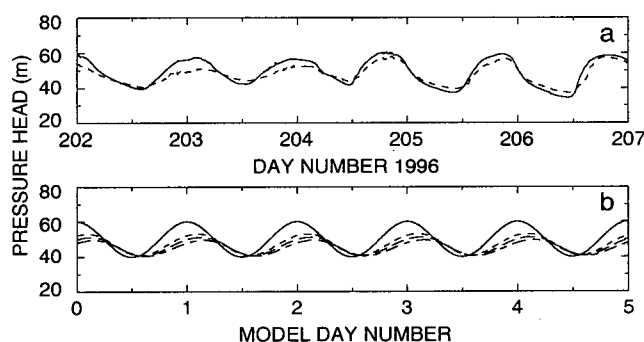
Figure 5.6: Comparison of field and modelled pore-water pressure records. (a) Records for P1 (solid line) and PZ1 (dashed line) during 20-25 July (days 202–207) 1996. Transducer PZ1 was installed at an estimated depth of 0.15 m. (b) Five-day pore-water pressures modelled for linear-viscous till at depths of 0.15 (short dashes), 0.25 (long dashes) and 0.35 m (short-long dashes). The solid line represents the drainage system pressure. Pore-water pressures for other till flow laws are similar.

Records for field and modelled pressure transducers are shown in Figure 5.6. The pressure records for P1 (solid line) and PZ1 (dotted line) are shown in Figure 5.6a; modelled responses shown in Figure 5.6b. The solid line in Figure 5.6b represents the prescribed pressure function at the ice–bed interface. Modelled pore-water pressures at depths of 0.15 (dotted line), 0.25 (dashed line) and 0.35 m (dot-dashed line) for linear-viscous till are also shown. The other till flow laws produced similar pressure profiles, with pore-water pressures differing by less than 0.025 m in all cases. These small differences are

due to slight dilatancy-driven variations in permeability structure. Modelled drainage-system and pore-water pressures show a relationship similar to that between P1 and PZ1, with pressures within the till layer exhibiting variations that are smaller in amplitude and lagged in phase in comparison with those in the drainage system. The record for PZ1 shows peak-to-peak pressure variations 44–78% of those indicated by P1 and exhibit lags of 40–86 min. Modelled pore-water pressure variations range between 39 and 73% of the 20.0 m diurnal pressure variation and lag by 94–258 min. Although modelled and field records at the estimated installation depth for PZ1 (0.15 m) show reasonable agreement, the lower amplitudes and greater lags indicated by synthetic records suggests that modelled permeabilities are too low.

Figure 5.7 shows till strain rates calculated from field (Fig. 5.7a) and modelled (Fig. 5.7b–e) tilt cell records. Modelled responses are calculated for installation depths of 0.15 (solid line), 0.25 (dotted line) and 0.35 m (dashed line). All synthetic records indicate minimum deformation rates at times of high system pressure due to ice–bed decoupling during these times. This behaviour is also seen in the record for BT1 (Fig. 5.7a). Because deformation of linear-viscous till (Fig. 5.7b) is uniform over the full till depth, similar responses are reported for the three modelled installation depths. Although the response for linear-viscous till is of similar form to that for BT1, the indicated strain rate is an order of magnitude lower, ranging between 0.019 and 0.040 d^{-1}. Deformation rates for nonlinear-viscous till (Fig. 5.7b) vary with installation depth, with higher strain rates seen nearer the top of the till layer. Till stiffening at low system pressures results in a slight reduction in deformation rate during these times. Indicated peak deformation rates of 0.031–0.037 d^{-1} are 6–13% those indicated by BT1.

Records for nonlinear-Bingham and Coulomb-plastic tills (Fig. 5.7d, e) indicate no deformation at high system pressures. The stiffness of the Bingham till dictates that sliding dominates at these times; for Coulomb-plastic till, deformation is confined to a
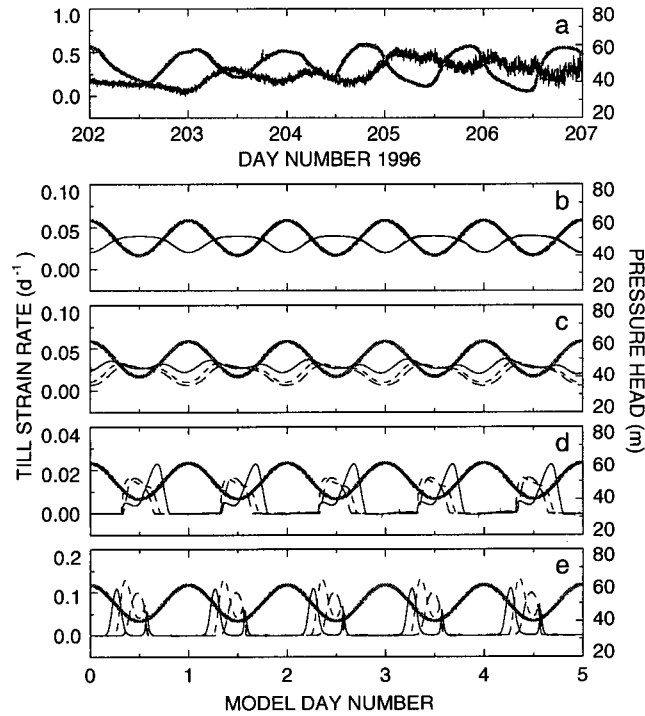
Figure 5.7: Comparison of till strain rates calculated from field and modelled tilt cell records. (a) Strain rate record for BT1 (black line) during 20-25 July (days 202-207) 1996. The pressure record for P1 (grey line) shown for comparison. Tilt cell BT1 was installed at an estimated depth of 0.15 m. (b-e) Modelled five-day strain rates for installation depths of 0.15 (solid line), 0.25 (short dashes) and 0.35 m (long dashes). Modelled drainage system pressure (thick grey line) shown for comparison. (b) Modelled strain rates for linear-viscous till. (c) Modelled strain rates for nonlinear-viscous till. (d) Modelled strain rates for nonlinear-Bingham till. (e) Modelled strain rates for Coulomb-plastic till.

thin region above the tilt cell. The calculated strain rate for both records show strong dependence on installation depth, with peak strain rates occurring later with deeper installation. Peak deformation rates for Bingham till are 0.016-$0.023\,\mathrm{d}^{-1}$, $\sim$3-8% of those indicated by BT1. Coulomb-plastic till exhibits higher deformation rates, with maximum values of 0.10-$0.13\,\mathrm{d}^{-1}$. The twin strain rate peaks at installation depths of

0.15 and 0.25 m arise from cyclic migration of the deforming region with system pressure variations. Slightly negative strain rates indicated in the responses for Bingham and Coulomb-plastic tills at peak system pressure is due to dilatant expansion of the till.
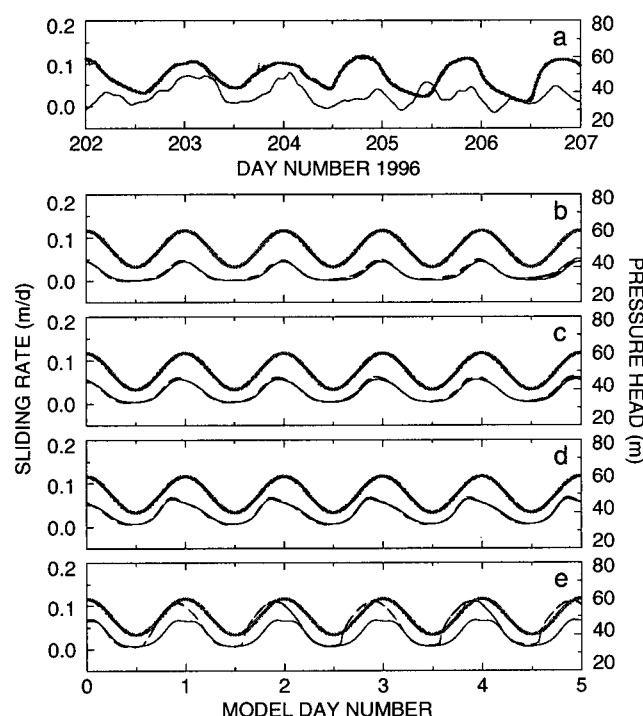
Figure 5.8: Comparison of indicated sliding rates calculated from field and modelled slidometer records. (a) Indicated sliding rates for SL1 (black line) during 20-25 July (days 202–207) 1996. Pressures reported by P1 (grey line) shown for comparison. The anchor for slidometer SL1 was installed at an estimated depth of 0.12 m. (b-e) Modelled five-day sliding rates for installation depths of 0.10 (short dashes), 0.20 (long dashes) and 0.30 m (short-long dashes). The true sliding rate is shown as the solid line, with the modelled drainage system pressure (thick grey line) included for comparison. (b) Indicated strain rates for linear-viscous till. (c) Indicated strain rates for nonlinear-viscous till. (d) Indicated strain rates for nonlinear-Bingham till. (e) Indicated strain rates for Coulomb-plastic till.

Figure 5.8 shows glacier sliding rates determined from field (Fig. 5.8a) and modelled

(Fig. 5.8b–e) slidometer records. Responses are calculated for installation depths of 0.10 (dotted line), 0.20 (dashed line) and 0.30 m (dot-dashed line), and the true modelled sliding rate is also shown (solid line). Modelled records show sliding rates and phase relations similar to those indicated during days 202.5–204.5 in the record for SL1 (Fig 16a). Peak sliding rates indicated by SL1 during this two-day period are 0.072 and 0.079 m/d. Peak indicated sliding rates for linear-viscous, nonlinear-viscous and Bingham tills (Fig. 5.8b–d) are close to the true value for all installation depths, with deformation adding ∼0.005–0.007 m/d to the true value. Coulomb-plastic till exhibit significant deformation in the uppermost portion of the till layer at times of rising system pressure, resulting in peak indicated sliding rates 168% of the true value at this time (Fig. 5.8e). This behaviour has been observed in sliding records for Trapridge Glacier (Blake and others, 1994; Fischer and Clarke, 1997b). Peak indicated sliding rates for linear-viscous, nonlinear-viscous, Bingham and Coulomb-plastic tills are 0.051, 0.063, 0.068 and 0.112 m/d, respectively; minimum sliding rates for the four till flow laws range between 0.002 and 0.005 m/d.

Modelled ploughmeter records are shown in Figure 5.9b–e, with the record for PL1 shown for comparison (Fig. 5.9a). Ploughmeter responses are calculated for installation depths of 0.10 m (solid line), 0.20 m (dotted line) and 0.30 m (dashed line), with greater installation depths resulting in higher calculated force values. The ploughmeter diameter is taken to be $d_{PL} = 0.03$ m and the tip-to-gauge offset $l_g = 0.10$ m. Figure 5.9b shows the modelled ploughmeter response for linear-viscous till. Force values are seen to be in-phase with system pressure (thick grey line). Because till properties do not vary with time, variations in the calculated force result from increased sliding velocities at times of high system pressure. Peak force values range between 2.3 and 2.6 kN for the modelled installation depths. Minimum force values, which occur at the time of minimum system pressure (and thus minimum sliding) are between 0.3 and 1.1 kN. Although forces in the record for PL1 (Fig. 5.9a, solid line) are of similar magnitude to those shown in Figure
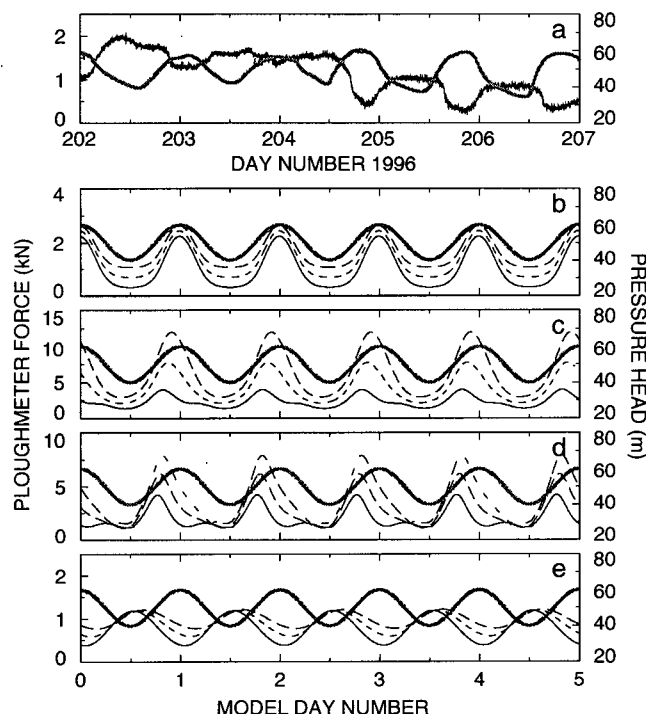
Figure 5.9: Comparison of field and modelled ploughmeter records. (a) Force record for PL1 (black line) during 20-25 July (days 202–207) 1996. The pressure record for P1 (grey line) shown for comparison. Ploughmeter PL1 was installed at an estimated depth of 0.14 m. (b–e) Modelled five-day ploughmeter records for installation depths of 0.10 (solid line), 0.20 (short dashes) and 0.30 m (long dashes). Modelled drainage system pressure (thick grey line) shown for comparison. (b) Modelled force records for linear-viscous till. (c) Modelled force records for nonlinear-viscous till. (d) Modelled force records for nonlinear-Bingham till. (e) Modelled force records for Coulomb-plastic till.

5.9a, peak modelled force values exhibit an in-phase relation with water pressure (grey line), as opposed to the out-of-phase relation seen in the records for PL1 and P1.

Maximum ploughmeter force values for non-linear viscous till (Fig. 5.9c) occur at times of rising system pressure. At this time, increasing sliding rates drag the ploughmeter through till that is relatively stiff. Diffusion of high pressures down into the

till layer results in till softening and reduced ploughmeter force values, with softening occurring at later times for greater installation depths. Stiffening of the till following peak system pressure gives rise to the small increase noted in the 0.10 m response (solid line). Maximum force values range between 4.1 and 12.1 kN, with minimum values of 1.4–2.9 kN. Ploughmeter responses for Bingham till (Fig. 5.9d) exhibit similar characteristics to those for non-linear viscous till. Neither till flow law reproduces the observed phase relationship between ploughmeter force values and drainage-system pressure seen in records for instruments PL1 and P1 (Fig. 5.9a). Maximum force values calculated for Bingham till are 4.2–7.9 kN; minimum values are 1.1–1.5 kN

Ploughmeter responses for Coulomb-plastic till (Fig. 5.9e) are similar in both magnitude and phase to records for field instruments PL1 and P1 (Fig. 5.9a). Maximum force values occur immediately following the time of minimum system pressure, with magnitudes of 1.18–1.21 kN. Minimum forces values range between 0.38 and 0.77 kN and lag peak pressure by 62–148 min due to the low permeability of the till.

5.3.2 Variation of till flow law parameters

Estimates of effective till viscosity (equation 4.62) range between 2×10^8 and 5×10^{11} Pa s (Paterson, 1994, Table 8.2); values estimated from Trapridge Glacier studies range from 3×10^9 (Fischer and Clarke, 1994) to 1.5×10^{11} Pa s (Blake, 1992). Results presented above assume a linear viscosity of $\eta_0 = 2.0 \times 10^{10}$ Pa s in (4.35). Decreasing this value by an order of magnitude changes modelled responses considerably. At this viscosity value, soft-bedded regions support less than 5% of the driving stress, resulting in increased ice velocities and deformation rates. The relative contribution of glacier sliding to the total basal motion decreases, and maximum ploughmeter force values are an order of magnitude lower, at 0.12–0.26 kN. Increasing the viscosity to $\eta_0 = 2.0 \times 10^{11}$ Pa s produces opposite effects, leading to lower ice velocities, lower deformation rates and maximum

ploughmeter force values measuring 10.4–10.7 kN, ~400% larger than those calculated for the nominal viscosity value. Modelled ice velocities, sliding rates and ploughmeter force values at an effective viscosity of $\eta_0 = 2.0 \times 10^{10}$ Pa s most closely match Trapridge Glacier observations.

The stiffness of nonlinear-viscous till is determined by the value of B_1 in (4.36). The value used for modelling the responses presented above, at 1.0×10^3 (kPa)$^{0.47}$a^{-1}, is ~30 times that suggested by Boulton and Hindmarsh (1987). Increasing this value by an order of magnitude produces changes similar to those resulting from decreasing the effective viscosity of a linear-viscous till, yielding higher flow velocities, increased deformation rates and lower ploughmeter force values. Ploughmeter responses are ~20% of those calculated for the nominal value, with peak force values of 0.5–2.1 kN. Soft-bedded regions support only 8–24% of the driving stress at this value of B_1. Decreasing the value of B_1 by a decade produces reduced ice velocities and deformation rates, and peak ploughmeter responses ranging between 28.2 and 57.5 kN, 375–590% larger than those for the nominal value of B_1.

Modelled deformation rates for nonlinear-Bingham till are 3–8% of those indicated by BT1 using the value $B_2 = 121.0$ (kPa)$^{0.625}$a^{-1} in (4.37) suggested by Boulton and Hindmarsh. Because the strain rate is related to the reduced shear stress $\tau - \sigma_Y$, this flow law is stiff for low values of B_2. Increasing the value of B_1 to soften the till and encourage greater deformation results in Coulomb-plastic behaviour: when the shear stress reaches the yield strength σ_Y of the material, deformation proceeds at a rapid rate, preventing the applied stress from exceeding the yield strength. Increasing the value of B_2 by an order of magnitude results in instrument responses similar to those for Coulomb-plastic till of the same yield strength σ_Y.

For Coulomb-plastic till, modelled ice velocities show little dependence on the yield strength σ_Y in (4.34). Increasing the value of ϕ in (4.34) limits basal deformation in

the connected region during times of low system pressure but does not strongly affect sliding or deformation rates at high system pressures. For values of ϕ greater than $\sim 30°$, (assuming $c_0 = 0$), the yield strength is sufficiently high to limit deformation to the uppermost $0.03\,\mathrm{m}$ of the till layer and thus preclude tilt cell rotation. High basal water pressures in the unconnected region allow deformation for all reasonable yield strength values.

5.3.3   Model sensitivity

Modelled responses discussed in the preceding sections were calculated using parameter values listed in Tables 5.1, 5.2, 5.3, 5.4 and 5.5. In this section I summarize the effects of varying several key parameters.

The value prescribed to the pore-water pressure p_B at the base of the till layer determines both the pressure gradient within the layer and, for nonlinear-viscous, Bingham and plastic tills, stiffness of the till at depth. Because the effective pressure does not appear in the flow relation (4.35) for linear-viscous till, no changes in modelled responses are noted with variations in basal pressure. For the pressure-dependent flow laws, lower basal pressures yield steeper pressure gradients and slightly lower deformation rates, and slight increases in ploughmeter force values. Soft-bedded regions for nonlinear-viscous and Bingham tills support marginally greater portions of the basal shear stress due to till stiffening at depth. Higher basal pressures produce opposite results, yielding higher deformation rates, lower ploughmeter force values and lower basal stresses in soft-bedded regions for nonlinear-viscous and Bingham tills. These tills also exhibit increased total ice velocities with increased basal pressure. For Coulomb-plastic till, variations in basal pressure do not noticeably affect the total ice velocity.

The depth to which diurnal pressure fluctuations penetrate into the till layer is largely determined by the steepness of the pressure gradient. Low basal pressures (and steep

pressure gradients) result in shallow penetration depths, with deeper penetration resulting from higher basal pressures. Because till strength depends on pore-water pressure, the basal pressure plays a strong role in determining the depth to which deformation occurs in the till layer. For nonlinear-viscous tills, the depth above which 50% of the total deformation occurs is 0.44 m at a basal pressure of 45.0 m. This depth decreases to 0.34 m at $p_B = 30.0$ m and 0.27 m at $p_B = 15.0$ m. This effect is more pronounced for Bingham and Coulomb-plastic tills. For nonlinear-Bingham till, all deformation occurs in the uppermost 0.94 m at $p_B = 45.0$ m in the till layer; decreasing the basal pressure value to 30.0 and 15.0 m results in maximum deformation depths of 0.44 m and 0.15 m, respectively. Deformation of Coulomb-plastic till occurs to depths of 0.79 m , 0.37 m and 0.18 m at basal pressures of 45.0, 30.0 and 15.0 m.

Variations in till-layer thickness affect linear-viscous and nonlinear-viscous tills differently than Bingham and Coulomb-plastic tills. Depth-integrated deformation rates for the viscous flow laws scale roughly with layer thickness. Total basal deformation rates for linear-viscous till average 0.065 m/d for till layer thickness of $h = 1.0$ m. Halving the layer thickness to 0.50 m reduces the total deformation rate to 0.040 m/d, while doubling the thickness to 2.0 m increases the total deformation rate to 0.096 m/d. The relationship between layer thickness and deformation rate is not 1:1 because any adjustment in flow velocity results in redistribution of basal shear stresses. Nonlinear-viscous till exhibits average total basal deformation rates of 0.018 m/d for a layer thickness of 0.50 m, 0.034 m/d at 1.00 m and 0.055 m/d at 2.00 m. Because deformation rates and till characteristics in the upper portion of the till layer are similar for these layer thicknesses, modelled instrument responses show only minor variations with till-layer thickness.

Deformation of nonlinear-Bingham and Coulomb-plastic tills is strongly determined by pore-water pressures and occurs in the uppermost portion of the till layer. Changes in till thickness affect Bingham and Coulomb-plastic tills mainly through their influence on

the pore-water pressure gradient: for a given value of basal pore-water pressure, greater till depths result in lower pressure gradients and thus deeper deformation. For nonlinear-Bingham tills, deformation occurs to depths of 0.12 m in a till layer of thickness 0.50 m, to 0.44 m in a till of thickness 1.00 m and 0.77 m in a 2.00 m-thick till. For Coulomb-plastic till, layer thicknesses of 0.50, 1.00 and 2.00 m yield deformation to depths of 0.08, 0.37 and 0.62 m. The steep pressure gradient in the 0.50 m till results in rapid stiffening of the till with depth for both till models, yielding higher ploughmeter force values and lower deformation rates at depth; till stiffness for both flow relations is sufficient to preclude any deformation at the greatest modelled tilt cell installation depth. The lower pressure gradient in the the 2.00 m layer thickness results lower ploughmeter force values and greater deformation rates at depth. Although the total ice velocity scales with till thickness for Bingham till, ice velocity for Coulomb-plastic till shows no dependence on layer thickness.

The ice flow rate is determined to a large extent by the value chosen for L_H, which represents the average length scale of variation between soft- and hard-bedded regions. The nominal value $L_H = 1500$ m yields average modelled ice velocities ranging between 0.04 m/d for Bingham till to 0.08 m/d for linear-viscous till. Increasing the length scale to $L_H = 3000.0$ m results in a moderate increase in ice velocities, to 0.05–0.14 m/d; modelled deformation rates, sliding rates and ploughmeter force values are ~135–175% those calculated for the nominal value of L_H. Reducing the length scale to $L_H = 750.0$ m yields ice velocities of 0.04–0.06 m/d and modelled instrument responses ~50–75% of those for the nominal value of L_H. At the longer length scale, a slight increase is noted in the shear stress supported by soft-bedded regions, resulting from increased viscous drag at the higher deformation rates. At the shorter length scale, the lower deformation rates result in lower shear stresses in these regions. Because the strength of Coulomb-plastic till is independent of deformation rate, the shear stress supported by soft-bedded

regions does not vary with L_H for this flow law. Similarly, ploughmeter force values are independent of L_H.

The value chosen for the length scale of variation between connected and unconnected regions L_S has little effect on modelled instrument responses or shear stress distribution. This parameter determines the velocity difference between soft-bedded regions. The nominal value $L_S = 150\,\mathrm{m}$ yields velocity contrasts at peak system pressure measuring 1–12% of the total ice velocity. Increasing L_S to 300.0 m results in velocity differences of 2–25%; decreasing L_S to 75.0 m yields differences ranging between <1% and 7%.

During times of high modelled system pressure, enhanced basal motion in the connected region transfers shear stress to the unconnected region, driving additional deformation there. At low system pressures, the stress transfer is reversed, with the unconnected region driving deformation in the connected region. Increasing the hydraulically-connected areal coverage α_1 at the expense of the unconnected coverage α_2 thus increases the proportion of the bed that drives glacier motion during times of high system pressure while decreasing the fraction driving motion at low system pressure. Larger values of α_1 result in higher peak ice velocities but decreased flow rates at low system pressure. In the case of Bingham and Coulomb-plastic tills, increasing α_1 such that $\alpha_1/\alpha_2 \gtrsim \sim 3.5$ results in driving stresses below the till yield strength σ_Y during times of low system pressure (for the assumed value of α_3). Because deformation is indicated at low system pressures by BT1, this suggests an upper limit to the ratio of connected to unconnected regions α_1/α_2 for Bingham and Coulomb-plastic tills.

Varying the areal fraction α_3 of hard-bedded regions has no effect on either glacier motion or instrument response for any of the four modelled flow laws. A series of model runs in which α_3 was varied while the ratio of connected to unconnected regions was held at $\alpha_1/\alpha_2 = 1/3$ showed that only the basal stress supported by the hard-bedded region τ_3 varies with changes in α_3. No change is noted in the shear stress supported

by either of the soft-bedded regions. This result is not surprising, as the flow rate of the glacier is controlled by the ice properties, the lengthscale of variation L_H, and the sediment properties. Given that the stresses τ_1 and τ_2 supported by the soft-bedded regions are unchanged by changes in α_3, the stress supported by the hard-bedded region is determined by Equation (4.48). Doubling the nominal value of α_3 from 0.20 to 0.40 results in diurnally-varying values for τ_3 of 2.13–2.16 τ_0 for linear-viscous till and 1.98–2.08 τ_0 for nonlinear-viscous till. Nonlinear-Bingham and Coulomb-plastic tills give values for τ_3 ranging 1.76–1.97 τ_0 and 1.93–2.22 τ_0, respectively. Decreasing the areal fraction of hard-bedded regions to $\alpha_3 = 0.10$ greatly increases the stress supported by hard-bedded regions: for a Coulomb-plastic till at peak drainage system pressure, the hard-bedded regions support a stress 8.31 times the nominal driving stress. For the other flow laws, peak stresses range between 6.83 τ_0 and 7.93 τ_0. These tests show that the magnitude of shear stress supported by the hard-bedded region depends strongly on the value of α_3 chosen, while the stresses supported by soft-bedded regions are independent of this value. If a glacier is predominantly soft-bedded, as Trapridge Glacier appears to be, hard-bedded regions could support very high stress values. Failure of the these pinning points – or of the ice coupling them to the soft-bedded regions – could allow unstable behaviour.

For a given drainage system pressure, the value p_{SL} in Equation (4.44) determines the relative contributions of mechanical and viscous coupling in the total ice–bed coupling. Increasing the value of p_{SL} increases the degree of mechanical coupling for a given water pressure, while decreasing p_{SL} increases the contribution of viscous coupling. Thus for a given drainage system pressure, lower values of p_{SL} yield higher sliding rates. Because the ice velocity is ultimately limited by the ice coupling the various regions together, varying p_{SL} does not significantly alter the modelled ice velocity: doubling the portion of the driving stress supported by viscous coupling results in only slight (4–9%) increases

in ice velocity at peak system pressure, while decreasing the portion of the driving stress supported by viscous coupling by 50% yields ice velocities only 1–8% lower. Because till softening also accompanies high system pressures, the degree of viscous coupling (i.e. as opposed to mechanical coupling) determines the relative contributions of sliding and basal deformation to the total ice velocity. With viscous coupling providing 20% of the total ice–bed coupling at flotation pressure, sliding accounts for 75% of the total ice velocity for linear-viscous till. At 10% viscous coupling, sliding comprises 34% of basal motion; at 40%, sliding accounts for 75%. This effect is largest for Coulomb-plastic till, with sliding contributing 29, 64 and 100% of the total basal motion at flotation-pressure viscous coupling of 10, 20 and 40%. However, because modelled deformation of Coulomb-plastic till occurs in the top 0.01–0.03 m of the layer at high system pressures, there is little practical difference between deformation and sliding.

In the model runs discussed above, it was assumed that no sliding occurred in the unconnected region. Because all four till flow laws yield relatively weak tills, only a small portion of the driving stress is supported by the unconnected region even with this assumption. Permitting sliding in the unconnected region results in an additional reduction of the shear stress supported there. Table 5.7 shows the minimum and maximum shear stresses supported by each region for modelling scenarios in which basal sliding is allowed in the unconnected region. Reductions in the shear stress supported by the unconnected region range between 17% for Coulomb-plastic till and 68% for nonlinear-Bingham till. The balance of the shear stress is redistributed onto the hard-bedded region and, to a lesser extent, connected regions. It can be seen in Table 5.7 that permitting sliding in the unconnected region further increases the role of hard-bedded in maintaining glacier stability. Allowing sliding also results in peak ice velocities that are 26%, 28% and 65% greater than the non-sliding case for linear-viscous, nonlinear-viscous and nonlinear-Bingham tills, respectively. No significant change in peak ice velocity is seen

Table 5.7: Modelled basal shear stresses, sliding allowed in unconnected region.

Flow Law	Minimum Shear Stress	Maximum Shear Stress
Linear-viscous till:		
Connected region	$0.17\,\tau_0$	$0.29\,\tau_0$
Unconnected region	0.16	0.17
Hard-bedded region	4.23	4.32
Nonlinear-viscous till:		
Connected region	0.22	0.76
Unconnected region	0.14	0.20
Hard-bedded region	3.83	4.19
Nonlinear-Bingham till:		
Connected region	0.25	1.13
Unconnected region	0.13	0.25
Hard-bedded region	3.47	4.03
Coulomb-plastic till:		
Connected region	0.18	0.98
Unconnected region	0.15	0.18
Hard-bedded region	3.56	4.22

for Coulomb-plastic till. Minimum ice velocities also show increased values. Of the flow laws modelled, nonlinear-Bingham till shows the largest increase, with a minimum ice velocity 129% of that modelled in the non-sliding case.

In general, the higher ice velocities result in increased deformation rates, and sliding rates, and ploughmeter force values. For linear-viscous till, peak deformation and sliding rates indicated by modelled tilt cell and slidometer responses measure ∼25% higher than those for the non-sliding case. Similar increases are noted in peak ploughmeter force values. Nonlinear-viscous tills show peak deformation rates that are approximately 30% greater, while peak deformation rates for nonlinear-Bingham till are approximately double those calculated in the non-sliding case. Peak sliding rates for these two tills

are approximately 30% and 38% greater. Nonlinear-viscous and nonlinear-Bingham tills exhibit peak ploughmeter responses ~20% and ~40% greater, respectively. Although permitting sliding in the unconnected region increases the magnitude of instrument responses for these flow laws, no significant changes are seen in the phase of these responses with respect to the drainage system pressure.

Because the strength of Coulomb-plastic till is independent of the strain rate, no change is observed in the modelled ploughmeter response for this flow law. Similarly, only minor increases are noted in peak deformation and sliding rates. In addition, no change is noted in the phase of these responses with respect to the drainage system pressure. Because of the rate-independent and therefore inherently unstable behaviour of Coulomb-plastic till, permitting sliding in the unconnected region does not significantly change the modelled flow or stability characteristics of a glacier underlain by such a material.

5.4   Discussion

In the following discussion I compare modelled instrument responses with field records in an effort to determine the till flow law that provides the best qualitative match to observed variations in hydrological and mechanical conditions.

Modelled deformation of linear-viscous and nonlinear-viscous tills occurs over the full till-layer thickness (Fig. 5.3f–j, k–o). Because of this behaviour, the total deformation rates for these flow laws tills are relatively high while the *strain rate* at any given depth is low. As a result, these flow laws exhibit modelled strain rates that are an order of magnitude lower than those indicated by the field record for BT1 (Fig. 5.7a–c). Decreasing the till thickness results in lower ice velocities and only marginally increased deformation rates for these tills.

Deformation of nonlinear-Bingham till is limited to the upper portion of the till layer (Fig. 5.3p–t), but the inherent stiffness of this flow law results in peak modelled strain rates that are just 3–8% of those indicated by the record for BT1 (Fig. 5.7d). Peak modelled strain rates for Coulomb-plastic till are significantly greater than rates calculated for the other flow laws, measuring 20–45% of those indicated by BT1. The record for BT1 indicates rotation throughout the diurnal pressure cycle. In this regard, the signal for linear-viscous till (Fig. 5.7b) most closely matches the field record, though at strain rates an order of magnitude lower. Modelled tilt cell rotation for Coulomb-plastic till occurs only during times of low system pressure due to strain localization. A more realistic treatment of strain distribution for Coulomb-plastic till, taking into account grain–grain interactions that would distribute failure over a length scale related to the grain-size distribution, could produce a deformation signal closer in character to that for a linear-viscous till. Strain rates indicated in the record for BT1 (Fig. 5.7a) are too high to be representative of strain rates over a significant layer thickness and are likely indicative of localized deformation.

Modelled slidometer records for all flow relations show similar character to that for SL1 (Fig. 5.8) and are thus not diagnostic. In contrast, significant differences between flow laws are seen in the phase relationship between modelled ploughmeter force values and drainage system pressures. Because of these differences, comparison of field and modelled ploughmeter responses provides perhaps the clearest means of identifying the flow law that best describes till behaviour. The magnitude of computed force values for linear-viscous till are in reasonable agreement with those for PL1 (Fig. 5.9a, b), but the phase relation with system pressure is opposite to that for PL1. Synthetic ploughmeter responses for nonlinear-viscous and Bingham tills (Fig. 5.9c, d) are approximately an order of magnitude larger than those for PL1. The ploughmeter force/system pressure phase characteristics also differ, with peak force values occurring at times of rising system

pressure. Modelled ploughmeter responses for Coulomb-plastic till show magnitudes similar to those indicated by PL1. In addition, the relationship between system pressure and ploughmeter force is similar to that exhibited by PL1 and P1, with peak force values occurring at minimum system pressure.

These comparisons of field and modelled responses for tilt cells, slidometers and ploughmeters indicate that of the four flow laws investigated, till behaviour is best represented by Coulomb-plastic failure. Of these instruments, the ploughmeter is perhaps the most diagnostic indicator of till behaviour. Only Coulomb-plastic till reproduces the out-of-phase relationship with drainage system pressure commonly observed in field records from Trapridge Glacier. Over the range of model parameter and boundary-condition values that I have investigated, no combination has produced the observed phase relationship for any of the three other flow laws. In contrast, this phase relationship is a robust feature of Coulomb-plastic till that results directly from the fact that the strength of such a material is rate-independent.

Features in the records for PL1 and SL1 (Fig. 5.1c, d) further suggest rate-independent behaviour. No correlation is seen between ploughmeter force and sliding rate in these records. This is most apparent during days 205–207, during which time the sliding rate varies strongly in a manner unrelated to variations in water pressure. The record for PL1, which was installed <1 m away, does not reflect these variations. Similar independence between ploughmeter force values and glacier flow rate have been observed at Storglaciären, Sweden (Hooke and others, 1997). These behaviours strongly suggest Coulomb-plastic behaviour.

Coulomb-plastic behaviour has important implications for glacier dynamics. While linear-viscous, nonlinear-viscous and nonlinear-Bingham tills support greater shear stress values at higher deformation rates (and thus resist runaway deformation), Coulomb-plastic till provides no additional resistance at elevated flow rates. In addition, the

modelled basal shear stress records shown in Figure 5.5 suggest that the viscous properties of the other till models act to dampen any changes in basal shear stress, lessening the rate at which longitudinal stresses are transferred to pinning points. For Coulomb-plastic tills, any additional longitudinal stresses are transferred directly and immediately to pinning points, increasing the possibility of failure. These behaviours suggest that Coulomb-plastic till can contribute greatly to flow instability of glaciers and ice streams.

The Figure 5.1d shows the total deformation during one model day in the connected region for Coulomb-plastic till. Although at any one time deformation occurs over a narrow band 0.01–0.24 m thick (Fig. 5.2u, w), total deformation over a diurnal cycle shows a nearly linear profile between depths of 0.03 and 0.32 m. This demonstrates that determination of flow law parameters from long-term deformation profiles can lead to decreased estimates of flow law nonlinearity in areas subject to pressure fluctuations. Similarly, deformation in the uppermost portion of the till can lead to overestimation of the contribution of sliding to basal motion; this is especially true for Coulomb-plastic tills, which exhibit strain localization. In the unconnected region, modelled deformation totals 0.07 m/d for Coulomb-plastic till, with deformation limited to the top 0.03 m of the till layer. In the field, it would not be possible to distinguish this deformation from glacier sliding; from a practical standpoint, little distinction exists between the two behaviours.

It is likely that the simple ice-dynamics model used in these studies greatly over-simplifies the nature of the interactions between various regions of the glacier bed. The across-glacier arrangement of the columns assumed in this model approximates the situation in which boundaries between the basal regions are aligned parallel to the direction of glacier flow. While the similarities between field instrument records from Trapridge Glacier and modelled instrument responses suggest that this approximation is acceptable, it is unclear how the glacier response would differ assuming different configurations of basal regions. For any reasonable basal geometry, however, it is unlikely that several

key behaviours would change significantly. For instance, given the generally weak tills modelled in this study, hard-bedded regions are likely to support a large portion of the driving stress. Diurnal variations in the drainage system pressure would result in fluctuations of sediment strength and ice–bed coupling, resulting in diurnal changes in the ice flow rate and the cyclic transfer of shear stress between basal regions. Given these similar characteristics, it is unlikely that instrument responses would differ fundamentally from those presented here. Thus while incorporating a more general and complex ice-dynamics model could refine the details of these behaviours and allow fine-tuning of the other components of this hydromechanical model, I doubt that doing so would lead to significantly different conclusions about the mechanical behaviour of till.

5.5   Conclusions

Of the four tested rheological models, modelled instrument responses for Coulomb-plastic till yield the best qualitative match to field instrument records from Trapridge Glacier. Synthetic tilt cell, slidometer and ploughmeter responses show good agreement in both magnitude and phase with field responses. Modelled responses for linear-viscous, nonlinear-viscous and nonlinear-Bingham tills fail to produce the observed phase relationship between system water pressure and ploughmeter force values, and till deformation rates for these laws are an order magnitude lower than those indicated by the field record.

For the modelled ranges of till thickness and basal pore-water pressure, Coulomb-plastic deformation occurs to depths of 0.08–0.77 m, with the "best fit" model indicating deformation to 0.37 m. These values show good agreement with the estimated deformation depth of $\sim$0.3 m at Trapridge Glacier by Blake (1992). Although at any one time deformation of Coulomb-plastic till can be localized to a narrow depth range, migration of the actively-deforming zone with cyclic pressure variations leads to time-averaged

deformation profiles that imply nearly-linear flow.

Unlike the other flow models, Coulomb-plastic till provides no additional resistance at elevated flow rates, making it more prone to unstable behaviour. Modelling results suggest that, for Coulomb-plastic till, the connected region of the bed supports only ~20% of the basal driving stress during times of high drainage system pressure, with the unconnected region supporting a similar portion. These results are in agreement with estimates of basal stress supported by sediments beneath Antarctic ice streams by Kamb (1991) and Tulaczyk and others (2000c) and highlight the importance of local pinning points in maintaining glacier stability. Indeed, surge initiation could be a matter of overwhelming key pinning points rather than further softening the till.

Chapter 6

Conclusions

This thesis contains the results of investigations into the hydromechanical behaviour of a surge-type glacier. Central to these investigations are *in situ* instrument measurements, which allow direct examination of the subglacial environment and provide necessary constraints for numerical modelling.

I have identified a mode of pressure transducer failure that clarifies the interpretation of records that otherwise challenge understanding. Instrument records suggest that pressure pulses are generated by abrupt glacier motion that compresses or dilates the subglacial hydraulic system. Laboratory studies indicate that pulse magnitudes ranging from $\sim$900 m to greater than 1500 m could account for the pressure offsets noted in transducer records from Trapridge Glacier. Instrument records suggest that pulses can be transmitted to remote regions through the subglacial drainage system. Such transmission could provide mechanical teleconnection between regions of the bed that are weakly coupled by longitudinal stresses.

Analysis of instrument records taken during early summer 1995 indicates that a series of subglacial hydromechanical events occurred following the establishment of a subglacial drainage system. Pressure transducer records indicate that hydraulic connection was established simultaneously over a $\sim$20 000 m^2 area, creating a region of instability that could have covered much of this region. Pressure fluctuations in the drainage system could have weakened a region of the bed that was acting as a local pinning point, resulting in three episodes of strong basal motion. Vigorous motion during the events is indicated

141

by damage to a number of mechanical instruments. Pressure transducer records suggest the generation of high-pressure pulses during the events.

I have developed a numerical model of subglacial conditions beneath a soft-bedded alpine glacier. The model calculates the time-evolution of pore-water pressure, porosity, till deformation, basal sliding and shear-stress transfer in different basal regions to prescribed variations in subglacial drainage system pressure. Sediment deformation profiles are calculated using four different till flow laws, including linear-viscous, nonlinear-viscous, nonlinear-Bingham and Coulomb-plastic. Synthetic instrument responses for a variety of sensors are calculated from the modelled pore-water pressure, till deformation, sliding and till strength conditions.

Comparison of synthetic instrument responses with simultaneous measurements of basal sliding, sediment strength, sediment deformation, basal water pressure and pore-water pressure recorded at Trapridge Glacier suggests that till is best modelled as a Coulomb-plastic material. Synthetic tilt cell, slidometer and ploughmeter responses for this flow law show good agreement in both magnitude and phase with field responses. Modelled responses for linear-viscous, nonlinear-viscous and nonlinear-Bingham tills fail to produce the observed phase relationship between system water pressure and ploughmeter force values, and till deformation rates for these laws are an order magnitude lower than those indicated by the field record.

Coulomb-plastic behaviour has important implications for glacier dynamics. While linear-viscous, nonlinear-viscous and nonlinear-Bingham tills support greater shear stress values at higher deformation rates (and thus resist runaway deformation), Coulomb-plastic till provides no additional resistance to fast flow. Modelling results also suggest that soft-bedded regions support, on average, only $\sim$20% of the basal driving stress. These results are in agreement with estimates of basal stress supported by sediments beneath Antarctic ice streams and highlight the important role local pinning points play

in maintaining glacier stability. This role is also indicated by the episodes of strong basal motion described in Chapter 3. Instrument records suggest that these events resulted from the failure of a local pinning point. These studies raise the intriguing possibility that surge initiation could be a matter of overwhelming key pinning points rather than further softening the till.

References

Anandakrishnan, S. and R. B. Alley. 1994. Ice Stream C, Antarctica, sticky spots detected by microearthquake monitoring. *Ann. Glaciol.*, **20**, 183–186.

Alley, R. B. 1989. Water-pressure coupling of sliding and bed deformation: II. velocity-depth profiles. *J. Glaciol.*, **35**(119), 119–129.

Alley, R. B. 1990. Multiple steady states in ice-water-till systems. *Ann. Glaciol.*, **14**, 1–5.

Alley, R. B. 1993. In search of ice-stream sticky spots. *J. Glaciol.*, **39**(133), 447–454.

Alley, R. B., D. D. Blankenship, C. R. Bentley and S. T. Rooney. 1986. Deformation of till beneath ice stream B, West Antarctica. *Nature*, **322**(6074), 57–59.

Alley, R. B., D. D. Blankenship, C. R. Bentley and S. T. Rooney. 1987a. Till beneath Ice Stream B: 3. Till deformation: evidence and implications. *J. Geophys. Res.*, **92**(B9), 8921–8929.

Alley, R. B., D. D. Blankenship, S. T. Rooney and C. R. Bentley. 1987b. Till beneath Ice Stream B: 4. Till deformation: A coupled ice–till flow model. *J. Geophys. Res.*, **92**(B9), 8931–8940.

Andrade, E. N. da C. and J. W. Fox. 1949. The mechanism of dilatancy. *Proc. Phys. Soc.*, Ser. B, **62**, 483–500.

Batchelor, G. K. 1970. Slender-Body Theory for Particles of Arbirary Cross-Section in Stokes Flow. *J. Fluid Mech.*, **44**(3), 419–440.

Bear, J., and A. Verruijt. 1987. *Modeling Groundwater Flow and Pollution.* D. Reidel Publishing Co., Dordrecht.

Blankenship, D. D., C. R. Bentley, S. T. Rooney and R. B. Alley. 1986. Seismic measurements reveal a saturated porous layer beneath an active Antarctic ice stream. *Nature*, **322**(6074), 54–57.

Blankenship, D. D., C. R. Bentley, S. T. Rooney and R. B. Alley. 1987. Till beneath Ice Stream B: 1. Properties derived from seismic travel times. *J. Geophys. Res.*, **92**(B9), 8903–8911.

Blake, E. 1992. The deforming bed beneath a surge-type glacier: measurements of mechanical and electrical properties. (Ph. D. thesis, University of British Columbia.)

Blake, E. and G. K. C. Clarke. 1989. *In situ* bed strain measurements beneath a surge-type glacier. *EOS*, **70**(43), 1084. [Abstract].

Blake, E., G. K. C. Clarke and M. C. Gérin. 1992. Tools for examining subglacial bed deformation. *J. Glaciol.*, **38**(130), 388–396.

Blake, E., U. H. Fischer and G. K. C. Clarke. 1994. Direct measurement of sliding at the glacier bed. *J. Glaciol.*, **40**(136), 595–599.

Blatter, H. 1995. Velocity and stress fields in grounded glaciers: a simple algorithm for including deviatoric stress gradients. *J. Glaciol.*, **41**(138), 333–344.

Blatter, H., G. K. C. Clarke and J. Colinge. 1998. Stress and velocity fields in glaciers: Part II. Sliding and basal stress distribution. *J. Glaciol.*, **44**(148), 457–466.

Boulton, G. S., D. L. Dent and E. M. Morris. 1974. Subglacial shearing and crushing and the role of water pressures in tills from south-east Iceland. *Geogr. Ann.*, Ser.

A., **56**, 135–145.

Boulton, G. S. and R. C. A. Hindmarsh. 1987. Sediment deformation beneath glaciers: rheology and geological consequences. *J. Geophys. Res.*, **92**(B9), 9059–9082.

Boulton, G. S. and A. S. Jones. 1979. Stability of temperate ice caps and ice sheets resting on beds of deformable material. *J. Glaciol.*, **24**(90), 29–43.

Bourbié, T., O. Coussy and B. Zinszner. 1987. *Acoustics of Porous Media*, Gulf Publishing Co., Houston.

Briggs, L. J. 1953. Limiting negative pressure of water. *J. Appl. Phys.*, **21**, 721–722.

Brown, N. E., B. Hallet and D. B. Booth. 1987. Rapid soft bed sliding of the Puget glacial lobe. *J. Geophys. Res.*, **92**(B9), 8985–8997.

Carman, P. C. 1961. *L'écoulement des gaz à travers les milieux poreux*, Bibliothèque des Sciences et Techniques mucléaires, Presses Universitaires de France, Paris.

Clarke, G. K. C. 1987a. A short history of scientific investigations on glaciers. *J. Glaciol.*, Special Issue, 1–21.

Clarke, G. K. C. 1987b. Subglacial till: a physical framework for its properties and processes. *J. Geophys. Res.*, **92**(B9), 9023–9036.

Clarke, G. K. C. 1996. Lumped-element analysis of subglacial hydraulic circuits. *J. Geophys. Res.*, **101**(B8), 17,547–17,559.

Clarke, G. K. C. and E. W. Blake. 1991. Geometric and thermal evolution of a surge-type glacier in its quiescent state: Trapridge Glacier 1969–89. *J. Glaciol.*, **37**(125), 158–169.

Clarke, G. K. C., S. G. Collins and D. E. Thompson. 1984. Flow, thermal structure, and subglacial conditions of a surge-type glacier. *Ca. J. Earth Sci.*, **21**, 232–240.

Clarke, G. K. C., U. Nitsan and W. S. B. Paterson. 1977. Strain heating and creep instability in glaciers and ice sheets. *Rev. Geophys. Space Phys.*, **15**(2), 235–247.

Clayton, L. and S. R. Moran. 1982. Chronology of Late Wisconsinan glaciation in middle North America. *Quat. Sci. Rev.*, **1**, 55–82.

Collins, S. G. 1972. Survey of the Rusty Glacier area, Yukon Territory, Canada, 1967–70. *J. Glaciol*, **11**(62), 235–253.

Cooper, H. H., Jr. 1966. The equation of groundwater flow in fixed and deforming coordinates. *J. Geophys. Res.*, **71**(20), 4785–4790.

Cox, R. G. 1970. The motion of long slender bodies in a viscous fluid. *J. Fluid Mech.*, **44**(4), 791–810.

Deeley, R. M. and P. H. Parr. 1914. The Hintereis Glacier. *Philosophical Magazine*, Ser. 6, **27**(157), 85–111.

Engelhardt, H. F., W. D. Harrison and B. Kamb. 1978. Basal sliding and conditions at the glacier bed as revealed by borehole photography. *J. Glaciol.*, **20**(84), 469–508.

Echelmeyer, K. A., W. D. Harrison, C. Larsen and J. E. Mitchell. 1994. The role of the ice margins in the dynamics of an active ice stream. *J. Glaciol.*, **40**(136), 527–538.

Engelhardt, H. F., N. Humphrey, B. Kamb and M. Fahenstock. 1990. Physical conditions at the base of a fast moving Antarctic ice stream. *Science*, **248**(4951), 57–59.

Ewing, M., A. P. Crary and A. M. Thorne. 1934. Propagation of elastic waves in ice Part I. *Physics*, **5**, 165–168.

Fischer, U. H. 1995. Mechanical conditions beneath a surge-type glacier. (Ph.D. thesis, University of British Columbia.)

Fischer, U. H. and G. K. C. Clarke. 1994. Ploughing of subglacial sediment. *J. Glaciol.*, **40**(134), 97–106.

Fischer, U. H. and G. K. C. Clarke. 1997a. Clast collision frequency as an indicator of glacier sliding rate. *J. Glaciol.*, **43**(145), 460–466.

Fischer, U. H. and G. K. C. Clarke. 1997b. Stick-slip sliding behaviour at the base of a glacier. *Ann. Glaciol.*, **24**, 390–396.

Fischer, U. H. and G. K. C. Clarke. In press. A review of subglacial hydro-mechanical coupling: Trapridge Glacier, Canada. *Quat. Int.*

Fischer, U. H., G. K. C. Clarke and H. Blatter. 1999. Evidence for temporally-varying "sticky spots" at the base of Trapridge Glacier, Yukon Territory, Canada. *J. Glaciol.*, **45**(150), 352–360.

Flowers, G. E. 2000. A multicomponent coupled model of glacier hydrology. (Ph.D. thesis, University of British Columbia.)

Flowers, G. E. and G. K. C. Clarke. 1999. Surface and bed topography of Trapridge Glacier, Yukon Territory, Canada: digital elevation models and derived hydraulic geometry. *J. Glaciol.*, **45**(149),165–174.

Flowers, G. E. and G. K. C. Clarke. 2000. An integrated modelling approach to understanding subglacial hydraulic release events. *Annals of Glaciology*, **31**.

Fountain, A. G. 1994. Borehole water-level variations and implications for the sub-glacial hydraulics of South Cascade Glacier, Washington State, U.S.A. *J. Glaciol.*, **40**(135), 293–304.

Fowler, A. C. 1986. A sliding law for glaciers of constant viscosity in the presence of subglacial cavitation. *Proc. Royal Soc. London*, **407**(1832), 147–170.

Fowler, A. C. 1987. A theory of glacier surges. *J. Geophys. Res.*, **92**(B9), 9111–9120.

Gold, L. W. 1958. Some observations on the dependence of strain on stress for ice. *Can. J. Phys.*, **36**, 1265–1275.

Gordon, S., M. Sharp, B. Hubbard, C. Smart, B. Ketterling and I. Willis. 1998. Seasonal reorganization of subglacial drainage inferred for measurements in boreholes. *Hydrol. Process.*, **12**, 105–133.

Haefeli, R. 1951. Some observation on glacier flow. *J. Glaciol.*, 1(9), 496–500.

Hairer, E., and G. Wanner. 1991. *Solving Ordinary Differential Equations II.*, Berlin, Heidelberg, New York, Springer-Verlag.

Harbor, J., M. Sharp, L. Copland, B. Hubbard, P. Nienow and D. Mair. 1997. Influence of subglacial drainage conditions on the velocity distribution within a glacier cross section. *Geology*, **25**(8), 739–742.

Harrison, W. D., K. A. Echelmeyer and H. Engelhardt. 1993. Short-period observations of speed, strain and seismicity on Ice Stream B, Antarctica. *J. Glaciol.*, **39**(133), 463–470.

Harrison, W. D. and B. Kamb. 1970. Direct measurement of sliding velocity at the base of a glacier. *EOS*, **51**(4), 431. [Abstract].

Harrison, W. D. and B. Kamb. 1970. Glacier bore-hole photography. *J. Glaciol.*, **12**(64), 129–137.

Hill, 1956. *The Mathematical Theory of Plasticity,* 2nd edition. Clarendon, Oxford.

Hobbs, P. B. 1974. *Ice Physics.* Clarendon Press, Oxford.

Hooke, R. LeB., P. Calla, P. Holmlund, M. Nilsson and A. Stroeven. 1989. A 3 year record of seasonal variations in surface velocity, Storglaciären, Sweden. *J. Glaciol.*, **35**(12), 235–247.

Hooke, R. LeB., B. Hanson, N. R. Iverson, P. Jansson and U. H. Fischer. 1997. Rheology of till beneath Storglaciären, Sweden. *J. Glaciol.*, **43**(143), 172–179.

Hopkins, 1862. On the theory of the motion of glaciers. *Philosophical Transactions of the Royal Society,* **152**, 677–745.

Humphrey, N. 1993. Characteristics of the bed of the Lower Columbia Glacier, Alaska. *J. Geophys. Res.*, **98**(B1), 837–846.

Hutter, K. 1983. *Theoretical Glaciology.* Dordrecht, etc., D. Reidel Publishing Co.

Iken, A. and R. A. Bindschadler. 1986. Combined measurements of subglacial water presure and surface velocity of Findelegletscher, Switzerland: conclusions about drainage system and sliding mechanism. *J. Glaciol.*, **32**(110), 101–119.

Iken, A., H. Röthlisberger, A. Flotron and W. Haeberli. 1983. The uplift of Unteraargletscher at the beginning of the melt season – a consequence of water storage at the bed? *J. Glaciol.*, **29**(101), 28–47.

Iverson, R.M. 1985. A constitutive equation for mass movement behavior. *J. Geology* **93**, 143–160.

Iverson, N. R., R. W. Baker, R. LeB. Hooke and P. Jansson. 1999. Coupling between a glacier and a soft bed: I. A relation between water pressure and local shear stress determined from till elasticity. *J. Glaciol.* **45**(149), 31–40.

Iverson, N. R. 1999. Coupling between a glacier and a soft bed: II. Model results. *J. Glaciol.* **45**(149), 41–53.

Iverson, N. R., P. Jansson, and R. LeB. Hooke. 1994. In situ measurement of the strength of deforming subglacial sediment. *J. Glaciol.*, **40**(136), 497–503.

Iverson, N. R., B. Hanson, R. LeB. Hooke and P. Jansson. 1995. Flow mechanism of glaciers on soft beds. *Science*, **267**, 80–81.

Iverson, N. R., R. W. Baker and T. S. Hooyer. 1997. A ring-shear device for the study of till deformation: tests on tills with contrasting clay contents. *Quat. Sci. Rev.*, **16**(9), 1057-1066.

Iverson, N. R., T. S. Hooyer and R. W. Baker. 1998. Ring-shear studies of till deformation: Coulomb-plastic behavior and distributed strain in glacier beds. *J. Geology*, **44**(148), 634–642.

Jackson, M. and B. Kamb. 1998. The marginal shear stress of Ice Stream B, West Antarctica. *J. Geology*, **43**(145), 415–426.

Jansson, P. 1995. Water pressure and basal sliding on Storglaciären, northern Sweden. *J. Glaciol.*, **41**(138), 232–240.

Jarvis, G. T. and G. K. C. Clarke. 1975. The thermal regime of Trapridge Glacier and its relevance to glacier surging. *J. Glaciol.*, **14**(71), 235–250.

Jona, F. and P. Scherrer. 1952. Die elastischen Konstanten von Eis-Einkristallen. *Helv. phys. Acta*, **25**, 35–54.

Kahaner, D., C. Moler, and S. Nash. 1989. *Numerical Methods and Software.*, Englewood Cliffs, Prentice-Hall.

Kamb, B. 1970. Sliding motion of glaciers: theory and observation. *Rev. Geophys. Space Phys.*, **8**(4), 673–728.

Kamb, B. 1987. Glacier surge mechanism based on linked cavity configuration of the basal water conduit system. *J. Geophys. Res.* **92**(B9), 9083–9100.

Kamb, B. 1991. Rheological nonlinearity and flow instability in the deforming bed mechanism of ice stream motion. *J. Geophys. Res.*, **96**(B10), 16585–16595.

Kamb, B. and E. LaChapelle. 1964. Direct observations of the mechanism of glacier sliding over bedrock. *J. Glaciol.*, **5**(38), 159–172.

Kamb, B., C. F. Raymond, W. D. Harrison, H. Engelhardt, K. A. Echelmeyer, N. Humphrey, M. M. Brugman, T. Pfeffer. 1985. Glacier surge mechanism: 1982–1983 surge of Variegated Glacier, Alaska. *Science*, **227**(4686), 469–479.

Kavanaugh, J. L. and G. K. C. Clarke. 2000. Evidence for extreme pressure pulses in the subglacial water system. *J. Glaciol.* **46**(153), 206–212.

Knapp, R. T., Daily, J. W. and F. G. Hammitt. 1970. *Cavitation*. McGraw-Hill, New York.

Kuper, C. G. and D. H. Trevene. 1952. The effect of dissolved gases on the tensile strength of liquids. *Proc. Phys. Soc. London, A*, **65**, 46–54.

Lambe, T. W. and R. V. Whitman. 1979. *Soil mechanics.* John Wiley and Sons, New York.

Lliboutry, L. 1968. General theory of subglacial cavitation and sliding of temperate glaciers. *J. Glaciol.* **7**(49), 21–58.

Lliboutry, L. 1987. Realistic, yet simple bottom boundary condition for glaciers and ice sheets. *J. Geophys. Res.* **92**(B9), 9101–9019.

McCall, J. G. 1952. The internal structure of a cirque glacier; report on studies of the englacial movements and temperatures. *J. Glaciol.*, **2**(12), 122–131.

McKinlay, D. G., A. McGown, A. M. Radwan and D. Hossain. 1978. Representative sampling and testing in fissured lodgement tills. *The Engineering Behaviour of Glacial Materials*, pp. 129–140. Geo Abstracts, Northwich, England.

Malvern, L. E. 1969. *Introduction to the Mechanics of a Continuous Media.* Englewood Cliffs, Prentice-Hall.

Meier, M. and A. Post. 1969. What are glacier surges? *Can. J. Earth Sci.*, **6**, 807–817.

Meier, M. and A. Post. 1987. Fast tidewater glaciers. *J. Geophys. Res.*, **92**(B9), 9051–9058.

Mercer, J. H. 1978. West Antarctic ice sheet and CO_2 greenhouse effect: a threat of disaster. *Nature*, **271**, 321–325.

Meyer, J. 1911. Zur Kenntnis des negativen Drukes in Flüssigkeiten. *Abhandl. Deut. Bunsen Ges.*, Nr. 1; der ganzen Reihe Nr. 6.

Mitchell, J. K. 1993. *Fundamentals of Soil Behavior,* 2nd edition. John Wiley & Sons, Inc., New York, 437 p.

Morner, N.-A. and A. Dreimanis. 1973. The Erie Interstade, in *The Wisconsinan Stage,* edited by R. P. Goldthwait and H. B. Willman. *Mem. Geol. Soc. Am.,* **136**, 107–134.

Murray, T. and G. K. C. Clarke. 1995. Black-box modeling of the subglacial water system. *J. Geophys. Res.,* **100**(B7), 10231–10245.

Narod, B. B. and G. K. C. Clarke. 1980. Airborne UHF radio echo-sounding of three Yukon glaciers. *J. Glaciol.,* **25**(91), 23–31.

Northwood, T. D. 1947. Sonic determination of the elastic properties of ice. *Can. J. Res.,* **A25**, 88–95.

Nye, J. F. 1969. A calculation on the sliding of ice over a wavy surface using a Newtonian viscous approximation. *Proc. Royal Soc.,* **331**(1506), 445–467.

Oldenborger, G. A., G. K. C. Clarke and D. H. D. Hildes. In review. Hydrochemical coupling of a glacial borehole–aquifer system. *J. Glaciol.*

Paterson, W. S. B. 1994. *The Physics of Glaciers,* 3rd edition. Pergamon Press, Oxford, England.

Porter, P. R., T. Murray and J. A. Dowdeswell. 1997. Sediment deformation and basal dynamics beneath a glacier surge front: Bakaninbreen, Svalbard. *Ann. Glaciol.,* **24**, 21–26.

Raymond, C. 1971. Flow in a trnasverse section of Athabasca Glacier, Alberta, Canada. *J. Glaciol.,* **10**(58), 55–84.

Raymond, C. 1987. How do glaciers surge? A review. *J. Geophys. Res.* **92**(B9), 9121–9134.

Raymond, C. 1996. Shear margins in glaciers and ice sheets. *J. Glaciol.*, **42**(140), 90–102.

Reynolds, O. 1885. On the dilatancy of media composed of rigid particles in contact, with experimental illustrations. *Philos. Mag.*, **20**, 469–481.

Röthlisberger, H. and H. Lang. 1987. Glacial Hydrology. *In* Gurnell, A. M. and M. J. Clark, *eds. Glacio-fluvial sediment transfer; an alpine perspective.* Chichester, etc., John Wiley and Sons, 207–284.

Saussure, H.-B. de. 1779–96. *Voyages dans les Alpes, précédés d'un essai sur l'histoire naturelle des environs de Geneve.* 4 vols. Neuchâtel, S. Fauche.

St. Lawrence, W. and A. Qamar. 1979. Hydraulic transients: a seismic source in volcanoes and glaciers. *Science*, **203**(4381), 654–656.

Stone, D. B. 1993. Characterization of the basal hydraulic system of a surge-type glacier: Trapridge Glacier, 1989-92. (Ph.D. thesis, University of British Columbia.)

Stone, D. B. and G. K. C. Clarke. 1993. Estimation of subglacial hydraulic properties from induced changes in basal water pressure: a theoretical framework for borehole-response tests. *J. Glaciol.*, **39**(132), 327–340.

Stone, D. B. and G. K. C. Clarke. 1996. *In situ* measurements of basal water quality and pressure as an indication of the character of subglacial drainage systems. *Hydrol. Proc.*, **10**(4), 615–628.

Stone, D. B., G. K. C. Clarke and E. W. Blake. 1993. Subglacial measurement of turbidity and electrical conductivity. *J. Glaciol.*, **39**(132), 415–420.

Temperley, H. N. V. and LL. G. Chambers. 1946. The behavior of water under hydrostatic tension: I. *Proc. Phys. Soc. London*, **58**, 420–436.

Tillett, J. P. K. 1970. Axial and trasverse Stokes flow past slender axisymmetric bodies. *J. Fluid Mech.*, **44**(3), 401–417.

Truffer, M. 1999. Till deformation beneath Black Rapids Glacier, Alaska, and its implications on glacier motion. (Ph. D. thesis, University of Alaska Fairbanks).

Truffer, M., K. A. Echelmeyer, and W. D. Harrison. In press. Implications of till deformation on glacier dynamics. *J. Glac.*.

Tulaczyk, S., B. Kamb and H. Engelhardt. 2000a. Basal mechanics of Ice Stream B, West Antarctica. I. Till mechanics. *J. Geophys. Res.*, **105**(B1), 463–481.

Tulaczyk, S., B. Kamb and H. Engelhardt. 2000b. Basal mechanics of Ice Stream B, West Antarctica. II. Undrained plastic bed model. *J. Geophys. Res.*, **105**(B1), 483–494.

Tulaczyk, S., B. Kamb and H. Engelhardt. 2000c. Estimates of effective stress beneath Ice Stream B, West Antarctica, from till preconsolidation and void ratio. *Boreas*

van der Veen, C. J. and I. M. Whillans. 1996. Model experiments on the evolution and stability of ice streams. *Ann. Glaciol.*, **23**, 129–137.

Vivian, R. and G. Bocquet. 1973. Subglacial cavitation phenomena under the Glacier d'Argentière, Mont Blanc, France. *J. Glaciol.*, **12**(66), 439–451.

Walder, J. S. and A. C. Fowler. 1994. Channelized subglacial drainage over a deformable bed. *J. Glaciol.*, **40**(134), 3–15.

Weertman, J. 1957. On the sliding of glaciers. *J. Glaciol.*, **3**, 33–58.

Weertman, J. 1964. The theory of glacier sliding. *J. Glaciol.*, **5**(39), 287–303.

Weertman, J. and G. E. Birchfield. 1982. Subglacial water flow under ice streams and West Antarctic ice-sheet stability. *Ann. Glaciol.*, **3**, 316–320.

Whillans, I. M. and C. J. van der Veen. 1997. The role of lateral drag in the dynamics of Ice Stream B. *J. Glaciol.*, **43**(144), 231–237.